Charge carrier transport in two-dimensional tin halide perovskite field-effect transistors

zur Erlangung des Grades

„Doktor rerum naturalium“

am Fachbereich Chemie, Pharmazie und Geowissenschaften

der Johannes Gutenberg-Universität und in Kooperation

mit dem Max-Planck-Institut für Polymerforschung

in Mainz

Shuanglong Wang

Geboren in Henan, P.R. China

Mainz im Juni 2023

Die vorliegende Dissertation wurde in der Zeit von Oktober 2019 bis Juni 2023 am Max-Planck-Institut für Polymerforschung in Mainz unter Betreuung von Prof. Dr. Paul Blom angefertigt.

Dekan: Prof. Dr. Eva Rentschler, Johannes Gutenberg-Universität Mainz

1. Gutachter: Prof. Dr. Paul Blom, Max Planck Institut für Polymerforschung, Mainz

2. Gutachter: Prof. Dr. Carsten Streb, Johannes Gutenberg-Universität Mainz

Tag der mündlichen Prüfung: 17. Juli

Affidavit

I hereby declare that I completed the dissertation independently and without any external support. Except for the places mentioned and referenced in the thesis, no external sources were used.

Furthermore, I confirm that this thesis has not yet been submitted as part of another examination process neither in identical nor in similar form.

Ort, Datum: Unterschrift:

Abstract

Metal halide perovskites as new-generation semiconducting materials have gained huge attention in the field of high-performance solar cells, light-emitting diodes, and detectors, because of their excellent properties such as large light absorption coefficient, high charge mobility, tunable bandgap, and cost-effective solution processability. Field-effect transistors (FETs) provide an ideal platform to investigate the reliable long-range charge carrier transport properties of perovskite semiconductors including the influence of interfaces and morphology. Nevertheless, the mixed ionic-electronic nature of metal halide perovskites makes their performance in transistors complex in nature, with many challenges being still open. One aspect of the problem is the severe ion migration due to the presence of loosely bound constituent ions in these ionic materials, which are known to screen the electric field in perovskite FET devices, leading to low device mobility and large dual-sweep hysteresis.

The focus of this dissertation is on the systematic investigation of the charge carrier transport properties of two-dimensional (2D) layered tin halide perovskite in FETs. 2D layered tin halide perovskites are promising active channel materials for FET applications since bulky organic cations can effectively inhibit the ion migration. To understanding the correlation between chemical structure of organic spacer cations, grain size, thin film morphology, molecular organization, ion migration and charge carrier transport in 2D tin halide perovskite, different approaches, including grain engineering, additive modification, and spacer cation tuning have been employed in FETs. Combined with experimental characterization and simulation, it is revealed that reducing the number of grain boundaries and suppressing tin oxidation are effective methods to boost the charge carrier transport and minimize the ionic defects, leading to the overall improved electrical parameters of FET devices. A subtle change in molecular structure of organic cations has a significant impact on the molecular organization, phases and film morphology, which in turn, govern charge transport properties in 2D tin halide perovskite FETs.

Zusammenfassung

Metall-Halogenid Perowskite als Halbleitermaterial der neuen Generation haben aufgrund ihrer ausgezeichneten Eigenschaften wie einem großen Absorptionskoeffizienten für Licht, hoher Ladungsbeweglichkeit, einstellbarer Bandlücke und kostengünstiger Lösungsverarbeitbarkeit enormes Interesse im Bereich von leistungsstarken Solarzellen, Leuchtdioden und Detektoren gewonnen. Feldeffekttransistoren (FETs) bieten eine ideale Plattform, um die Zuverlässigkeit und Eigenschaften des Ladungsträgertransports über große Distanzen in Perowskit-Halbleitern zu untersuchen, einschließlich des Einflusses von Grenzflächen und Morphologie. Die gemischte ionisch-elektronische Natur von Metall-Halogenid Perowskiten macht ihre Wirkungsweise in Transistoren jedoch komplex, und viele Herausforderungen sind noch offen. Ein Aspekt des Problems ist die Ionendiffusion aufgrund der Anwesenheit locker gebundener ionische Bestandteile in diesen ionischen Materialien, die bekanntermaßen das elektrische Feld in Perowskit-FETs abschirmen und zu geringer Ladungsträgerbeweglichkeit und großem Hysterese führen.

Der Schwerpunkt dieser Dissertation liegt auf der systematischen Untersuchung der Ladungsträgertransporteigenschaften von zweidimensionalen (2D) geschichteten Zinnhalogenid-Perowskiten in FETs. 2D geschichtete Zinnhalogenid-Perowskite sind vielversprechende Materialien für den aktiven Kanal in FET-Anwendungen, da sperrige organische Kationen die Ionendiffusion effektiv hemmen können. Um den Zusammenhang zwischen der chemischen Struktur der organischen Kationen, der Korngröße, der Dünnschichtmorphologie, der molekularen Organisation, der Ionendiffusion und dem Ladungsträgertransport in 2D Zinnhalogenid-Perowskiten zu verstehen, wurden verschiedene Ansätze, einschließlich Korngrößen-Modifikation, Zusatzstoffmodifikation und Kationenanpassung, in FETs eingesetzt. In Kombination mit experimenteller Charakterisierung und Simulation wurde gezeigt, dass die Reduzierung der Anzahl von Korngrenzen und die Unterdrückung der Zinnoxidation effektive Methoden sind, um den Ladungsträgertransport zu

steigern und die ionischen Defekte zu minimieren, was zu verbesserten elektrischen Parametern der FETs führt. Gleichzeitig hat eine subtile Veränderung der molekularen Struktur des organischen Kations einen signifikanten Einfluss auf die molekulare Organisation, Phasen und sowie die Oberflächenmorphologie, die wiederum die Ladungsträgereigenschaften in 2D Zinnhalogenid-Perowskit-FETs bestimmen.

Contents

1 Chapter 1 Introduction

In this Chapter, two-dimensional (2D) tin halide perovskites and their physical properties in field-effect transistors (FETs) are introduced. First part is focused on the basic knowledge about 2D tin halide perovskites including crystal structure, organic cations, and thin film preparation. In addition, the electrical parameters of transistors and device physics of 2D tin halide perovskite FETs are systematically presented, especially regarding the ion migration and charge carrier transport. Finally, strategies to improve the device performance of the corresponding FETs are discussed in detail.

1.1 General background of 2D perovskite

1.1.1 Chemical structures

Metal halide perovskites are new-generation semiconductors due to their extraordinary optoelectronic properties such as high charge mobility, long carrier diffusion length, high photoluminescence quantum yield, solution processing and low-cost.[1-4] The bulk three-dimensional (3D) halide perovskites are most extensively studied with the general formula ABX_3, where the A site consists of organic or inorganic monovalent cations (typically methylammonium (MA) $CH_3NH_3^+$, formamidinium (FA) $HC\text{-}(NH_2)_2^+$, guanidinium (GA) $C\text{-}(NH_2)_3^+$, or inorganic cesium Cs^+), the B site is divalent metal ions (Pb^{2+}, or Sn^{2+}), and X represents halide anions (Cl^-, Br^-, or I^-), respectively, as shown in Figure 1.1a and b.[5-7] In perovskite structures, by treating all ions as hard and rigid spheres with a closed packing configuration, the relationship between the ionic radii can be obtained with the Goldschmidt's tolerance factor (t) and octahedral coefficient (μ) concept by the following equations[8,9]:

$$t = \frac{R_A + R_X}{\sqrt{2}(R_B + R_X)} \qquad \text{(Equation 1.1)}$$

$$\mu = \frac{R_B}{R_X} \qquad \text{(Equation 1.2)}$$

where R_A, R_B, and R_X are the ionic radii of the corresponding ions, respectively. The tolerance factor t for ionic radii is helpful for predicting new perovskite materials. 3D perovskites have typical tolerance factors between $0.8 \leq t \leq 1.0$ and $0.44 \leq \mu \leq 0.90$ (Figure 1.1c). With $t < 0.8$, the perovskite structures will be more distorted since the A site cation is not completely bonded and hard to fit into the BX_6 octahedron (Figure 1.1d). Additionally, stable structures are also formed for 3D perovskites when the t value is slightly above 1.[10,11] For example, the 3D perovskite with mixed cations $FA_{0.75}MA_{0.25}SnI_3$ possesses good structural stability with $t \sim 1.02$. However, further increasing t usually yields low-dimensional structures.[12] Therefore, the parameter t can be fine-tuned by changing the size of A-site cations to form an ideal perovskite structure.

The traditional 3D network with small size A-site cations consists of a corner-sharing coordinated inorganic octahedral structure, creating a favorable electronic band structure that facilitates the charge carrier transport.[13] On the contrary, bulky organic monovalent cations cannot be easily incorporated into the 3D network due to their large size, leading to an unstable crystal structure. Consequently, lower-dimensional perovskites emerged which can be imagined as “cleaving” the 3D structure into substructures with reduced dimensionality, transforming the inorganic divalent metals from crystal planes to sheets (Figure 1.1e).[14-16] Over the last ten years, the scientific community have devoted tremendous efforts to investigate the chemical and physical properties of traditional 3D and lower-dimensional perovskite materials and developed a wide variety of optoelectronic device applications, including solar cells, light emitting diodes, photodetectors, lasers, and others (Figure 1.1f).[17-21]

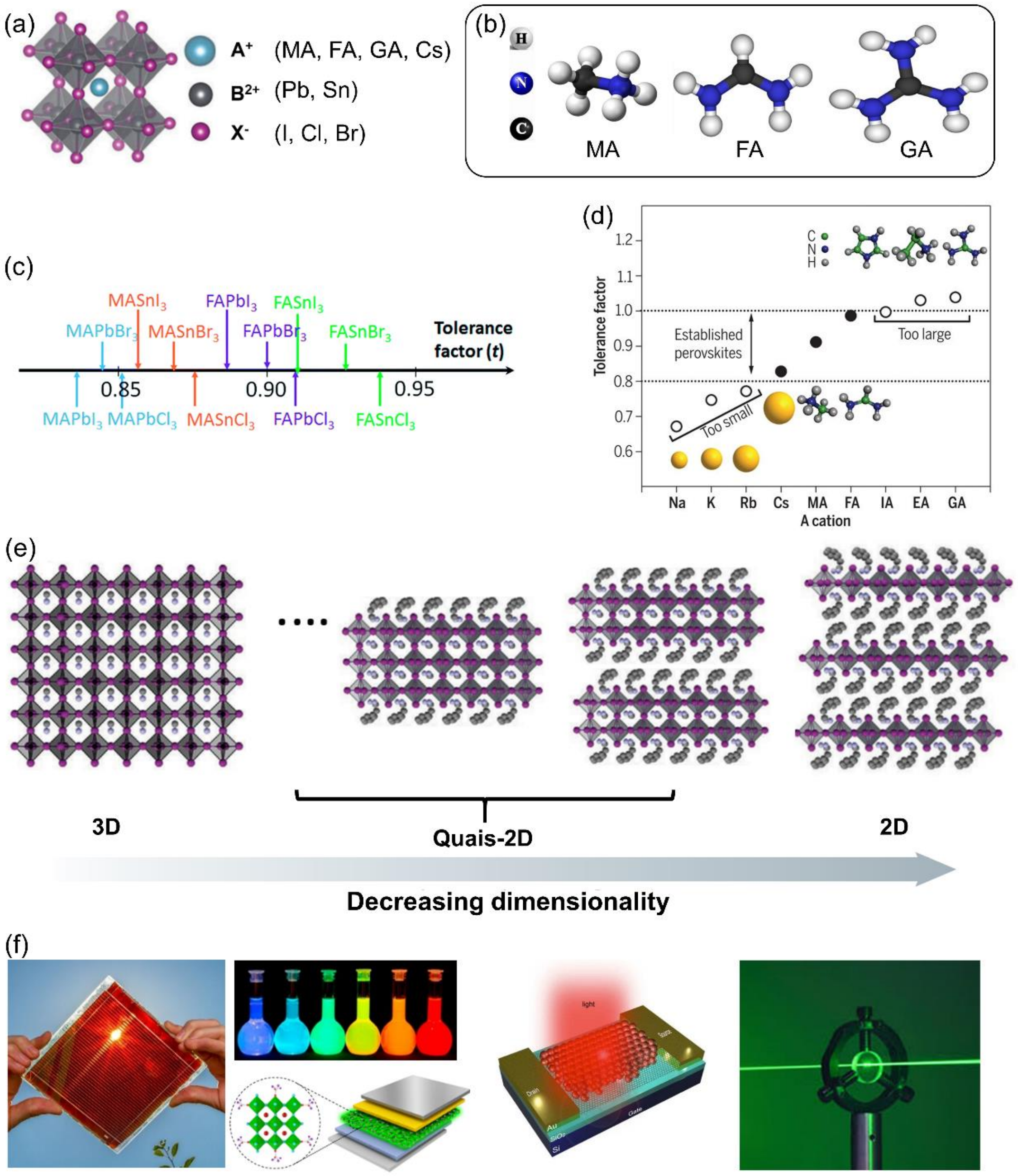

Figure 1.1. (a) Schematic structure of the perovskite semiconductor family (chemical formula, ABX_3);[1] (b) The structural representation of small molecular MA, FA, and GA cation;[5] (c) Tolerance factors of typical 3D perovskites with traditional size A-site cations;[10] (d) Tolerance factor of lead-iodine based $APbI_3$ perovskites with different ionic radius of A-site cations;[12] (e) Diagram of dimensional reduction of perovskites at the molecular level; (f) Illustration of the application of perovskite materials in various optoelectronic devices, such as solar cells, light-emitting diodes, photodetectors, and lasers.[17-21]

Two-dimensional (2D) metal halide perovskites resemble a (naturally formed) quantum well structure and exhibit excellent structural diversity such as layered or quasi-2D perovskites.[22] More importantly, their physical properties can be tuned by the layer thickness *n*. Here, the *n* value is defined as the number of inorganic layers in the 2D perovskite structure and it can be precisely tailored by controlling the stoichiometry of the precursor materials.[23] A common and representative structure of 2D halide perovskites is that alternated bulky monovalent organic cations and inorganic sheet structure are connected by hydrogen-bonding interactions.[24] In general, there are two main types for 2D perovskites: the Ruddlesden-Popper (RP) and Dion-Jacobson (DJ) phases (Figure 1.2). More specifically, the structure of the most extensively studied 2D RP perovskites is described by the general formula $(RNH_3)_2BX_4$, where RNH_3 is the bulky spacer cation, B is the divalent metal cations, and X represents the halide anions.[25] Large organic spacer cations are interdigitated between adjacent corner-sharing inorganic frameworks in 2D RP perovskites, leading to the formation of van der Waals gaps in the bulky spacers' bilayer structure.[26] The two layers of bulky spacer cations with opposite orientations result in a large interlayer distance between inorganic slabs. It is generally believed that it is difficult for charge carriers to tunnel through this organic part.[27]

In contrast, unlike 2D RP perovskites, DJ-type 2D perovskites do not contain a van der Waals gap between the 2D layers since the divalent organic spacer layer bridges the neighboring inorganic sheets by hydrogen-bonding interactions.[28] As such, the more robust and rigid structure combined with smaller inorganic layer spacing is expected to reduce the tunnel barrier of the organic layer and facilitate the charge carrier transport in both in-plane and out-of-plane directions.[29] Although the 2D DJ perovskites show great advantages, its application in electronic devices is far behind those of their 2D RP counterparts. This is likely due to the lack of available DJ-type organic ligands, leading to a low phase purity in perovskite thin films.[30] Thus, to date, 2D RP perovskites are mostly employed in transistors and other electronic devices.

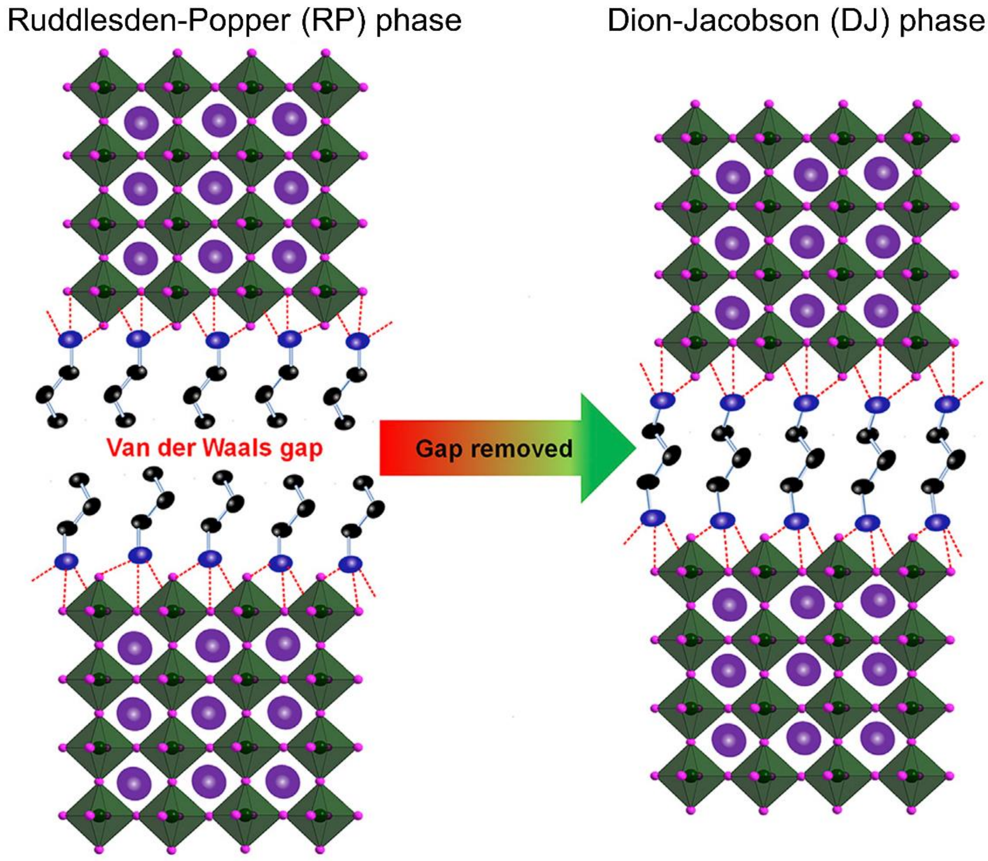

Figure 1.2. Schematic illustration of RP and DJ phase layered metal halide perovskite structures.[25]

1.1.2 Choice of organic cations

The chemical nature of bulky spacers strongly governs the crystal structural and optoelectronic properties of 2D perovskites. In particular, the physical properties of the 2D layered perovskites such as charge transport and phase purity can be easily tuned by the spacer cations: (i) the distortion of each connected octahedron and tilting of bonding angles (e.g., I-Sn-I), and (ii) the chemical and physical stability of the perovskite materials by controlling the hydrophobic cation.[31-33] So far, there have been several cases of organic spacer cations incorporated into low dimensional perovskite devices, with the chemical structures of some cations shown in Figure 1.3a and b. However, the structure-property relationships in layered perovskites are far from being understood. Most 2D perovskites based on novel organic cations are studied in trial-and-error tests by randomly picking the spacers.[34] To date, the structural design rules for the organic cations are still ill-defined. Therefore, a common understanding and in-depth insight into the correlation between the chosen spacer and the resulting structure, as well as its device performance are essential to drive the material design forward.[35] This holds the key to the development of novel 2D perovskites for high-performance optoelectronic devices.

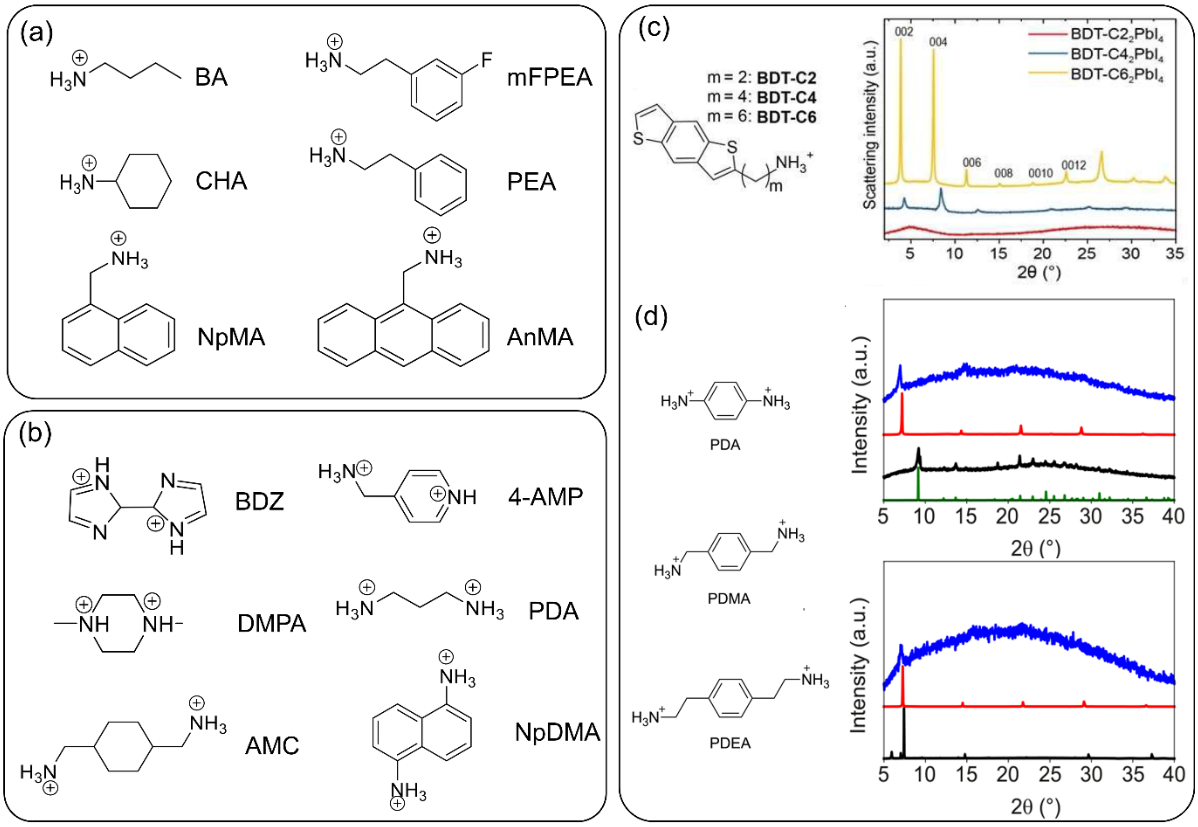

Figure 1.3. Chemical structures of typical spacer cations in (a) RP and (b) DJ perovskites; RP spacer cations: Butylammonium (BA); 3-fluorophenylethylammonium (mFPEA); Cyclohexylammonium (CHA); Phenethylammonium (PEA); 1-naphthalenemethylammonium (NpMA); 9-anthracenemethylammonium (AnMA). DJ spacer cations: 2,2'-Biimidazolium (BDZ); 4-(aminomethyl)piperidinium (4-AMP); 1,4-dimethylpiperazinium (DMPA); 1,3-propanediammonium (PDA); 1,4-bis(ammoniomethyl)cyclohexane (AMC); Naphthalene-1,5-diammonium (NpDMA); (c) Chemical structures of benzodithiophene-based ligands where m represents the number of carbon atoms in the alkyl chain, and corresponding XRD patterns of (BDT-Cm)$_2$PbI$_4$ thin films;[37] (d) Molecular structures of DJ-type PDA, PDMA, and PDEA organic spacers, and XRD data of I$^-$ (up) and Br$^-$ (down) based layered perovskites: black, PDA; red, PDMA; blue, PDEA. The green line shows the simulated diffractogram of (PDA)PbI$_4$·2H$_2$O.[38]

Typically, several critical factors should be considered including the geometry and functional groups when designing organic cations for 2D perovskite applications. According to the previous studies of RP-type layered perovskites, the length of the anchoring group (e.g., alkylammonium chain) plays an important role in the formation of the crystal structure. It is revealed that the penetration depth of the anchoring group into the inorganic perovskite layers is related to the length of the alkylammonium side chain, which has a strong effect on the structural and optoelectronic properties of the 2D perovskite.[36] Primera Darwich et. al. integrated benzodithiophene (BDT) based cations into a RP layered perovskite structure, as shown in Figure 1.3c. X-ray diffraction (XRD) patterns showed significant different phase behavior with respect to the number of carbon atoms in the alkyl side chain. The spacer cation BDT-C6 based perovskite exhibited clear and intense diffraction peaks which were assigned to a RP phase. However, the shorter alkyl chains drastically decreased crystallinity without any evident signal for a layered structure of BDT-C2, demonstrating that changing the alkyl chain length is a critical factor for incorporating rigid conjugated moieties in 2D perovskites.[37]

In another example, Dučinskas et. al reported three DJ-type organic spacers with 1,4-phenylenediammonium (PDA), 1,4-phenylenedimethylammonium (PDMA), and 1,4-phenylenediethylammonium (PDEA) with various alkyl chain lengths and different halogens, respectively (Figure 1.3d).[38] The results revealed that when using a iodine-based halide, PDA did not form a well-defined layered 2D DJ perovskite structure. This was likely due to the rigid structure of the PDA spacer, as well as its lower level of penetration into the neighboring perovskite layers, inhibiting the formation of the layered DJ perovskite phase. When the alkyl chains were extended to PDMA by adding one methylene ($-CH_2-$) group, the PDMA-based films showed typical layered perovskite diffraction patterns with a sharp diffraction peak at 7.19°, which was assigned to the (001) reflection. However, further increase of the spacer to PDEA resulted in significantly reduced diffraction intensities. The above discussion demonstrates the key role of alkyl chain length and provides an important design rule for incorporating organic cations. It should also be pointed out that the counterions (e.g., I^-, Br^-) govern the crystallinity of the 2D layered perovskites. As shown in the XRD patterns, when the anion I^- was replaced by Br^- for the PDA cation with the shortest alkyl chain length, the film exhibited different diffraction signals with higher order reflections, indicating the presence of a layered perovskite phase in the film. Therefore, the effect of the halide on structural properties should also be accounted for the selection of a suitable cation as organic spacer for 2D perovskites.

1.1.3 Thin film preparation

The quality of 2D perovskite thin films is paramount in determining the FETs performance. Homogeneous films with high-crystallinity, large grains, as well as good surface coverage and/or no pinholes are highly desirable for device optimization.[39] To date, several approaches including vacuum thermal evaporation and solution-processing have been developed to prepare the perovskite thin films. Thermal evaporation is one of the commonly employed technologies for semiconductor industry, which can be viewed as a physical-chemical process where the organic and inorganic precursor materials are mixed or separately loaded into different crucibles. The source materials are heated under a high vacuum along with vaporization to be deposited onto the substrates to form the perovskite layer, as shown in Figure 1.4a.[40] Despite the advantages of solvent- and annealing-free processing, the distinct drawbacks of this method hinder its wide application for perovskite deposition. Firstly, evaporation species and rate need to be precisely controlled to obtain dense and uniform films with controllable thickness, which complicate the fabrication processing. Secondly, a high vacuum environment is costly due to special customized equipment, which is unfavorable for large-scale applications.

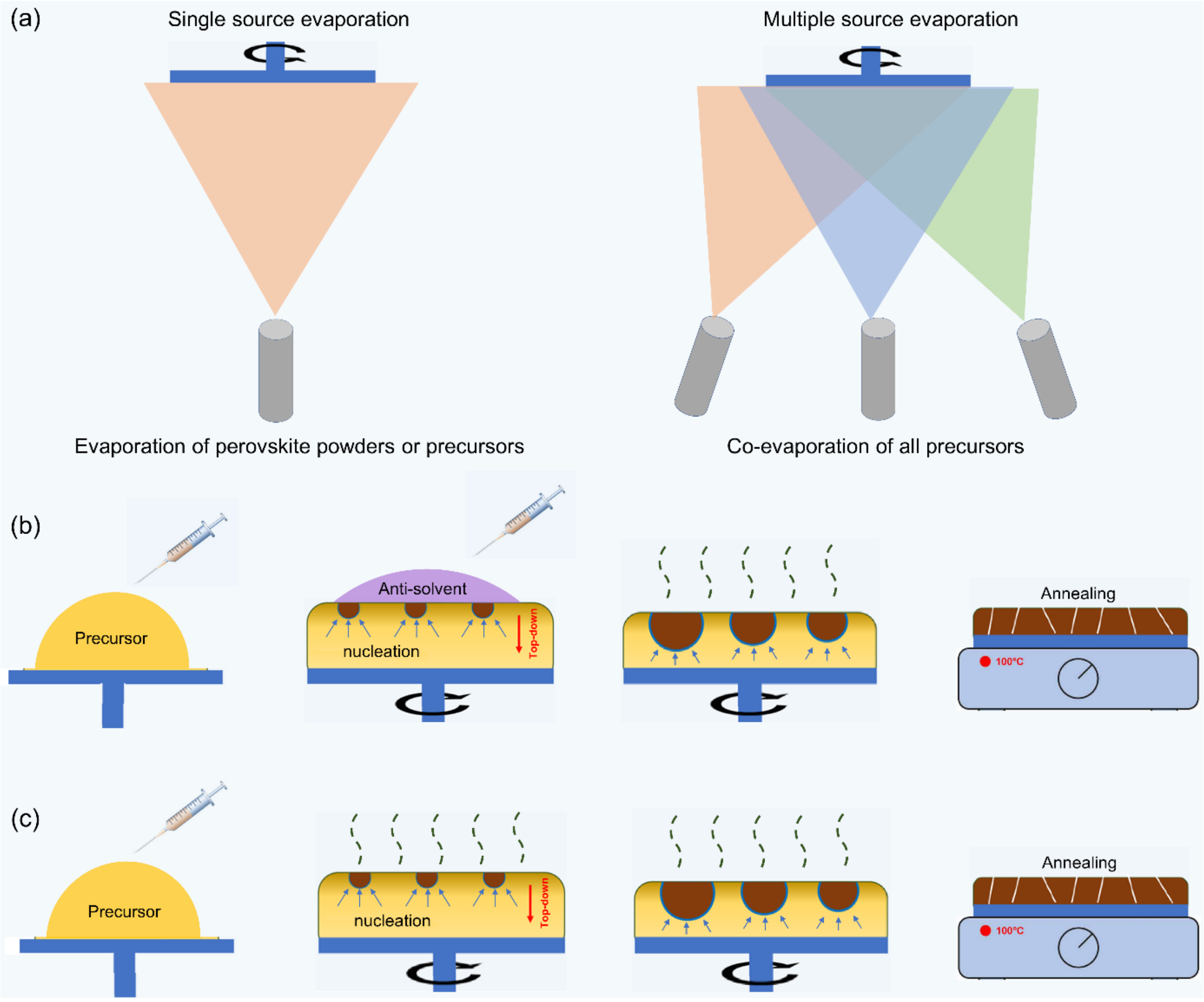

Figure 1.4. Illustrations of thin film processing of perovskites by (a) vacuum thermal evaporation; (b) two-step anti-solvent method; (c) direct one-step spin-coating.

Solution processing is a promising alternative way and mature technique, which is particularly attractive in industrial production due to low cost and easy control of film composition and thickness. In this method, the perovskite solution is prepared by dissolving the source precursor materials in polar solvents like N,N′-dimethylformamide (DMF), dimethyl sulfoxide (DMSO), and/or their mixtures for fast film drying. Among spin-coating techniques, the two-step anti-solvent method shows universality with various perovskites and is one of the most commonly used solution deposition approach for fabrication of high-performance perovskite thin films. For the procedure of anti-solvent processing, as shown in Figure 1.4b, firstly, a mixture of organic and inorganic source materials in the appropriate molar ratio is dissolved in processing solvents like DMF and DMSO. Secondly, the precursor solution is drop-cast onto the substrate and spread over the entire surface. Then the spin-coater is accelerated to a desired speed and maintains this for several tens of seconds to evaporate the solvent and start the nucleation. Finally, an anti-solvent (e.g., chlorobenzene) which does not dissolve the perovskite and is miscible with the host solvent DMF or DMSO is dropped onto the substrate during spin coating followed by film annealing at a certain temperature.

In 2014, Seok et al. firstly reported the use of toluene as an anti-solvent to prepare perovskite films.[41] Specifically, the anti-solvent toluene was dropped at a proper time window during the solution processing to extract residual solvents nearly instantly, enabling a remarkably improved power conversion efficiency and negligible hysteresis of solar cells. Since then, the use of various anti-solvent treatments has been proposed to boost the perovskite thin film quality. The working mechanism of anti-solvent processing is based on a heterogeneous nucleation via creating an instantaneous local super saturation in the wet film during spin-coating.[42] Therefore, insolubility and miscibility with the perovskite precursor solution are the basic requirements for choosing the anti-solvent. More importantly, the fundamental mechanism of the complicated interactions of both solvents under the influence of physicochemical properties during the anti-solvent treatment is far being understood. In addition, this approach involves several key parameters, which significantly influence the quality of perovskite film, such as the physical and chemical nature of the anti-solvent, the volume ratio between precursor solvent and anti-solvent, the exact dropping time, and others.[43]

In comparison with thermal evaporation and anti-solvent solution processing, the one-step solution method is much simpler and more universal for the preparation of perovskite thin films (Figure 1.4c). Despite that single-step deposition methods have enabled multiple cases of record efficiencies for perovskite devices, there is still a lack of comprehensive knowledge of how 2D perovskite grains crystallize from solution to solid during spin-coating and thermal annealing. A deep understanding of the crystallization process during one-step deposition will be beneficial for manipulating film morphology, and the orientation of the layers with respect to the substrate, which are critical factors for the fabrication of 2D perovskite thin films for optoelectronic devices.[44]

1.1.4 Ion migration

Ion migration has been regarded as one of the most interesting processes in halide perovskite-based electronic devices. Perovskite materials are generally considered as mixed conductors with ionic-electronic characteristics. The ionic migration cannot be neglected in perovskite devices due to a large fraction of mobile ions in these soft ionic materials. Previous studies have indicated that “mobile ion” are the cause of many important properties associated with perovskites in the devices (Figure 1.5).[45] Ion migration and accumulation contribute to anomalous phenomena such as hysteresis, and giant capacitance in solar cells, and are also being held responsible for the poor stability of the device. However, ion migration is believed to act as a double-edged sword, which also shows some advantages for device applications. For example, it was reported that the ion migration process was beneficial for promoting the device performance under continuous light illumination, since the accumulation of mobile ions can passivate traps at the interface in solar cells, leading to improved carrier transport and collection efficiency.[46] More importantly, perovskites are considered suited for resistance-switching memory device applications due to the ion migration behavior.[47] Additionally, fast response photodetectors are also potential applications for perovskites due to manipulation of the ion migration progress under varying electric field.[48] Therefore, understanding the ion migration process in perovskite materials is an important prerequisite for the development of perovskite based electronic devices.

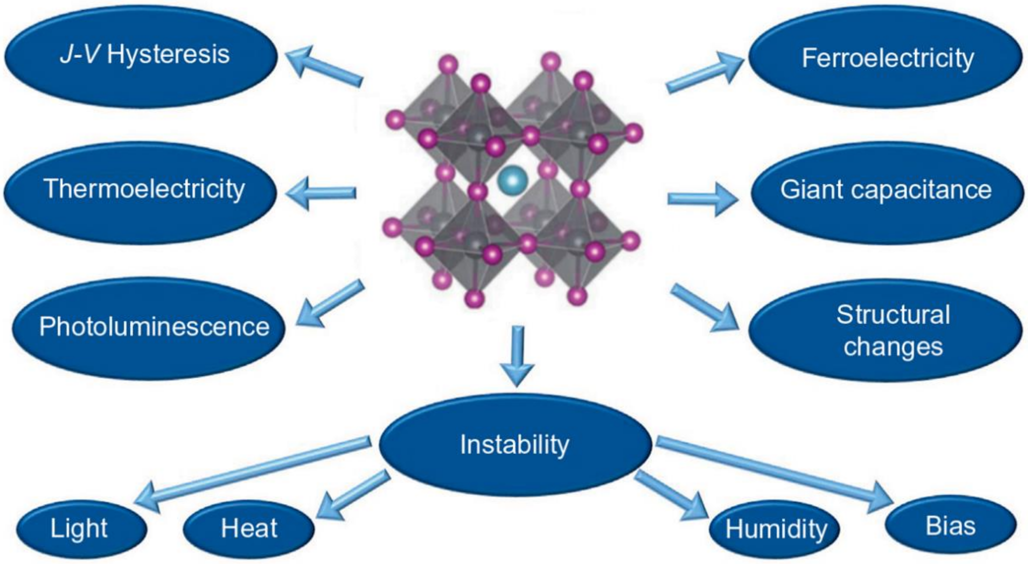

Figure 1.5. Observed phenomena in perovskites with possible relationship to ion migration.[45]

Theoretically, any of the constituting cations and anions in perovskite materials can migrate under certain conditions. For example, I^-, Sn^{2+} and MA^+ may migrate in 3D perovskite $MASnI_3$ films under the application of an electric field. However, in 2D tin halide perovskites, such as $(PEA)_2SnI_4$ or $(BA)_2SnI_4$, I^- and Sn^{2+} are the dominating mobile ions because the organic cation PEA^+ or BA^+ is considered to be more stable due to their large size.[49] Additional extrinsic ions resulting from decomposition or contamination of perovskites, such as H^+, may also be involved.[50] It is generally believed that ion migration is mediated by traps and defects in perovskite films. Therefore, reducing the number of defects in perovskite thin films is critical to suppress ion movement. Earlier studies revealed that the trap density N_t in single crystalline 3D organic-inorganic hybrid perovskites is around 10^9-10^{10} cm^{-3}. However, N_t significantly rises to 10^{16} cm^{-3} in polycrystalline perovskite thin films.[51] A large density of point defects can be generated in polycrystalline perovskite films by several origins, such as the fast crystallization of perovskite films prepared by solution or thermal-evaporation processes; and the non-stoichiometry ratio between the precursor materials in solution.[52]

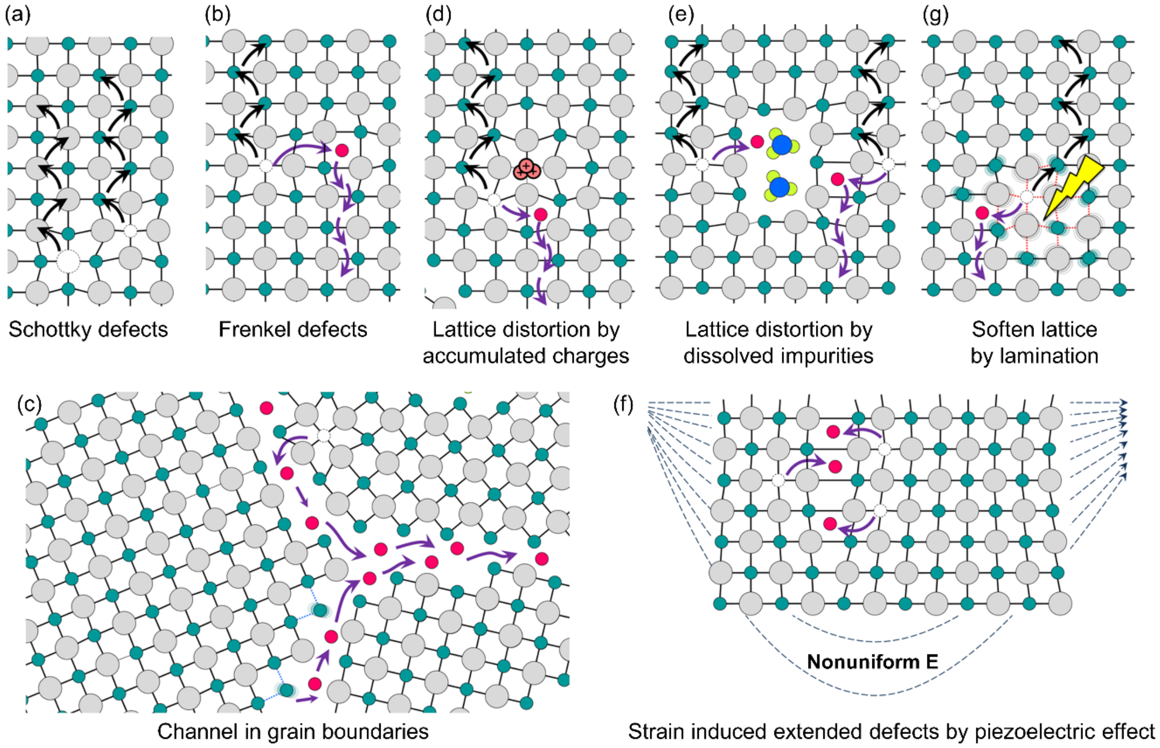

Figure 1.6. Illustration of ion migration pathways enabled by different possibilities of (a) Schottky defects; (b) Frenkel defects; (c) Open space and wrong bonds at grain boundaries; (d) Lattice distortions due to accumulated charges; (e) Dissolved impurities; (f) Soften lattice caused by the light illumination and (g) Induced bond weakening and non-uniform strain caused by the piezoelectric effect.[53]

Therefore, the generation of defects and resulting ion migration are inevitable during the fabrication of perovskite thin films. The point defects in perovskite include Schottky (Figure 1.6a) and Frenkel defects (Figure 1.6b). These point defects can move from site to site driven by an applied electric field.[53] The first experimentally confirmed migrating species related to point defects was MA^+ in $MAPbI_3$ perovskite solar cells by Yuan et al. in 2015. The migration of MA^+ was directly observed under applied voltage through a photo-thermal induced resonance technique.[54] In addition to bulk point defects, the surface and grain boundaries of the crystal grains also serve as important ion migration channels. Some reports revealed that the ion migration might be dominated by the grain boundaries in polycrystalline perovskite films (Figure 1.6c). The relatively open structure at grain boundaries and surfaces allows ion migration occurring with a low activation energy in comparison to that in the bulk.[55] In addition, other possible channels, such as a local lattice distortions caused by accumulated charges, dissolved impurities, soften lattice by lamination or non-uniform strain due to the piezoelectric effect (Figure 1.6d-g), light illumination induced lattice softness, are also possible causes for the formation of mobile ions.[56]

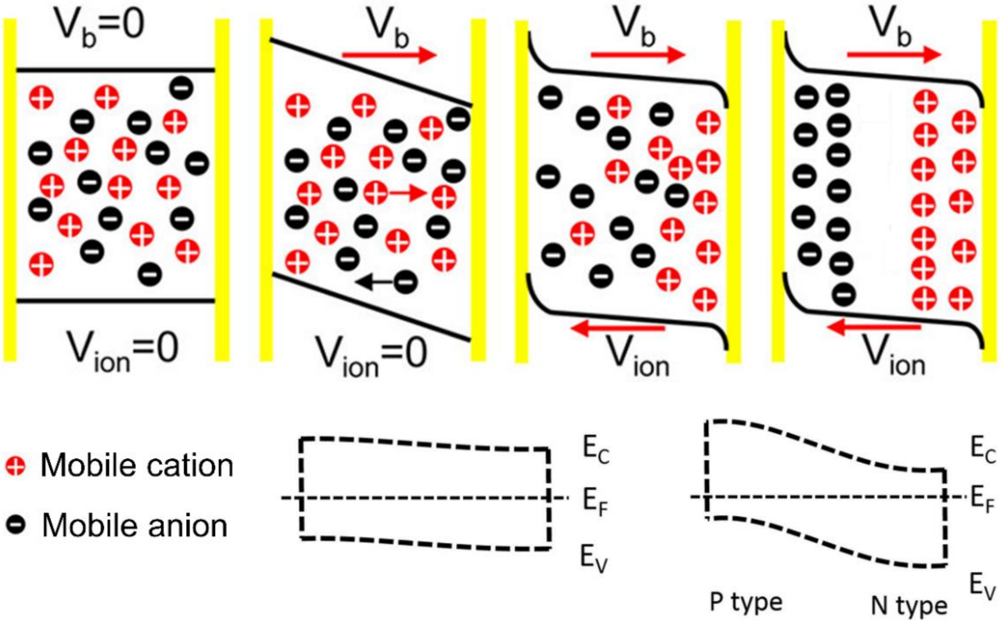

Figure 1.7. Schematic diagrams indicating the dynamics of ionic migration following application of an external voltage. The two yellow bars represent two lateral electrodes (up). Below are the corresponding energy diagrams in the perovskite layer before and after ion drift.[57]

Understanding the dynamics of the ion migration in perovskite devices is critical to maximize charge carrier transport. For example, in a sandwich-structure device, ions are randomly distributed throughout the device channel without external voltage. Then, the ions start to move when applied a positive bias V_b (pointing from left to right in Figure 1.7) leading to an ionic current in the channel. Afterwards, the oppositely charged ions accumulate near the perovskite-electrode interfaces, resulting in the formation of ionic layers and an ion-induced built-in electric field with the direction opposite to the external electric field, which significantly screens the external bias. The screening effect induced by ion migration is a typical problem for perovskite transistors, which would undoubtedly inhibit the charge carrier transport in the channel.[57] As more ions migrate towards the electrodes and accumulate at the perovskite-electrode interfaces at continuous V_b, the ion-induced electric field constantly increases and finally reaches equilibrium condition. Additionally, the positive ions/vacancies that move towards and accumulated at the cathode will act as space charges, causing *n*-type doping in the perovskite on the cathode side. Similarly, the remaining negative space charge layer close to the anode side can lead to *p*-type doping in the perovskite layer.[58] In this case, the corresponding negative and positive charges near the electrodes result in strong band bending. Overall, ion migration is one of the most important factors that seriously affect the performance of perovskite electronic devices.

As discussed above, the charge carrier transport properties in perovskite films are significantly limited by the migration and accumulation of mobile ions resulting in reduced device performance. Therefore, suppressing ion migration is of great importance in polycrystalline perovskite thin films. To date, there have been tremendous efforts devoted to inhibit ion movement and thus enhance the performance of perovskite devices, including additive,[59] mixed solvent,[60] and composition engineering.[61] Generally, these optimization methods can be categorized into three strategies to suppress ion movement: (i) enhancing formation energies of both cation and anion vacancies; (ii) defect passivation of grain boundaries and at surfaces to increase the activation energy of ionic defects; and (iii) minimizing the density of grain boundaries by controlling the crystallization via the processing parameters.[62] Despite the progress made to suppress ion migration in perovskites, it is still challenging to effectively control ion migration in FET devices. Further understanding of ion migration especially in 2D perovskite tin halide FETs is highly desirable to guide the material structure and device fabrication design.

1.1.5 Charge carrier transport

The non-conducting properties of organic cation ligands connected with the inorganic frameworks by hydrogen bonding in 2D perovskites significantly decrease the charge carrier mobility compared to the 3D perovskites. The large size spacer cations lead to a large distance between inorganic frameworks, as shown in Figure 1.8a. For example, the benchmark cations PEA and BA based 2D perovskites $(PEA)_2SnI_4$ and $(BA)_2SnI_4$ have interlayer distances of 16 and 13 Å (with the chemical structures of Figure 1.3), which makes it difficult for charge carriers to tunnel through the energy barrier along the out-of-plane direction, resulting in several orders of magnitude difference in conductivity measured in the in-plane and out-of-plane direction.[63] High-quality perovskite thin films are crucial for obtaining high-performance perovskite electronic devices. In 2D tin halide perovskites, there are several essential factors, such as molecular orientation and film morphology for improving the charge carrier transport properties.

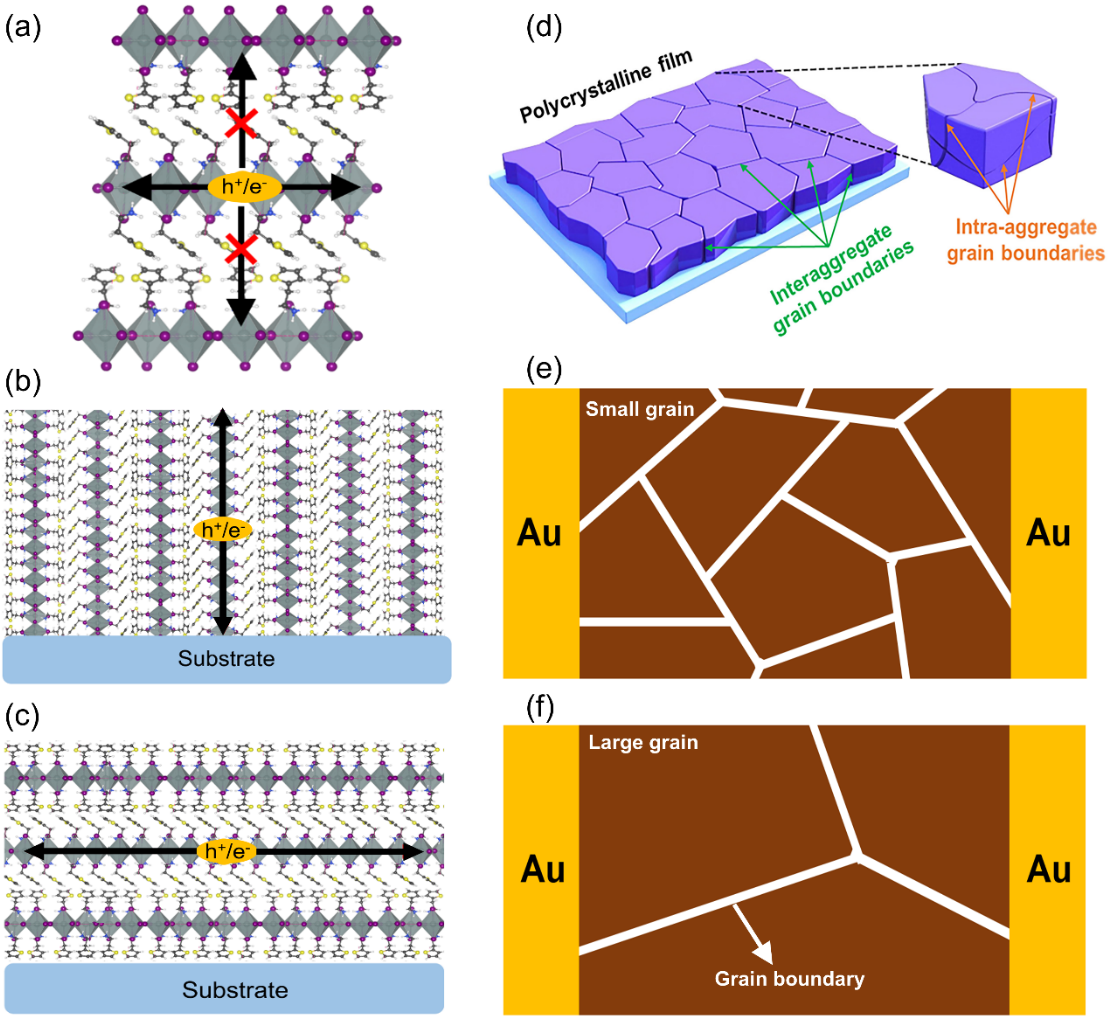

Figure 1.8. (a) Illustration of charge carrier transport in 2D perovskite layers; Schematic of the charge transport in oriented 2D perovskite layers perpendicular (b) and parallel (c) to the substrate. (d) Schematic diagram of a solid polycrystalline thin film with grain boundaries (GBs), illustrating interaggregate GBs and intra-aggregate GBs.[64] Illustration of (e) small and (f) large grain stacking in the FET channel.

Molecular orientation is one of the key factors that significantly affects charge carrier transport. Unlike the isotropic structure of 3D perovskites, the highly anisotropic structure of the 2D perovskites enables preferential growth perpendicular or parallel to the substrate, leading to a large difference between the out-of-plane and in-plane conductivity, which influences the charge carrier mobility in 2D perovskite transistors (Figure 1.8b and c).[64] Therefore, for transistor applications the parallel orientation of crystal structure in the thin film with respect to the substrate can ensure a direct charge transport pathway between the source and drain electrodes, which is crucial for the device performance.

An additional factor governing charge transport properties is the thin film morphology. The polycrystalline nature of the tin halide perovskites arising from rapid nucleation and crystallization when processed from solution and the unbalanced nucleation and crystal growth rate usually causes an inferior film morphology, including low surface coverage, large-size pinholes, and small grains with considerable density of grain boundaries (GBs). GBs can be viewed as the interface between two individual homo-phase grains. These adjacent grains are generally oriented in different crystallographic directions. More specifically, GBs can be categorized as intra-aggregate GBs and interaggregate GBs, respectively, as schematically shown in Figure 1.8d.[65] GBs usually create potential barriers since they serve as trap sites and scattering centers for charge carriers, contributing to a reduced charge carrier mobility and increased ion migration. Furthermore, it is generally believed that ions move much faster at the GBs than within the grains.[66] In addition, some imperfect structures occurring at GBs may affect the device operating stability associated with the presence of mobile ions, oxygen, water, heat, or/and light. Especially in perovskite-based transistors, small crystal grains will produce a large number of GBs, which significantly retard lateral charge carrier transport, leading to unsatisfied device performance.[67]

Therefore, superior morphology by controlling the grain growth and minimizing the number of GBs in 2D tin halide perovskites is crucial in maximizing the charge transport in perovskite devices. In this regard, enlarging the perovskite grain size is a useful approach to reduce both the number of GBs and the defect density (Figure 1.8e and f). To date, many approaches, such as additive engineering and post-treatment processes have been widely investigated to increase the grain size in solar cell devices.[68,69] However, it should be pointed out that due to the different operating mechanisms between transistors and solar cells, the above methods cannot be directly applied to transistor devices. For example, thick perovskite films with balanced hole/electron charge transport out-of-plane are required for photovoltaics. On the contrary, a thin channel layer facilitating either electron- or hole-dominated charge transport in the in-plane direction is desirable for unipolar transistor applications. Therefore, these differences require rationalized optimization approaches for transistor devices.

1.2 Characterization of FETs

FET is a three-terminal device that can be viewed as a voltage controlled electrical switch. To date, next to conventional Si based integrated circuits FETs based on alternative semiconductors are being considered for potential applications as display drivers, identification tags and smart cards.[70] FETs consist of a layered structure with a thin semiconductor film, a dielectric layer, and three electrodes named source (S), drain (D), and gate (G), respectively, as shown in Figure 1.9a. Generally, there are four principal architectures for FET devices, depending on the deposition order of the different functional layers. So far, all of these device geometries have been demonstrated for perovskite transistors. The S (usually grounded) and D electrodes have a direct contact with the semiconductor film and the G electrode is separated by a dielectric layer from the semiconductor and the other electrodes.

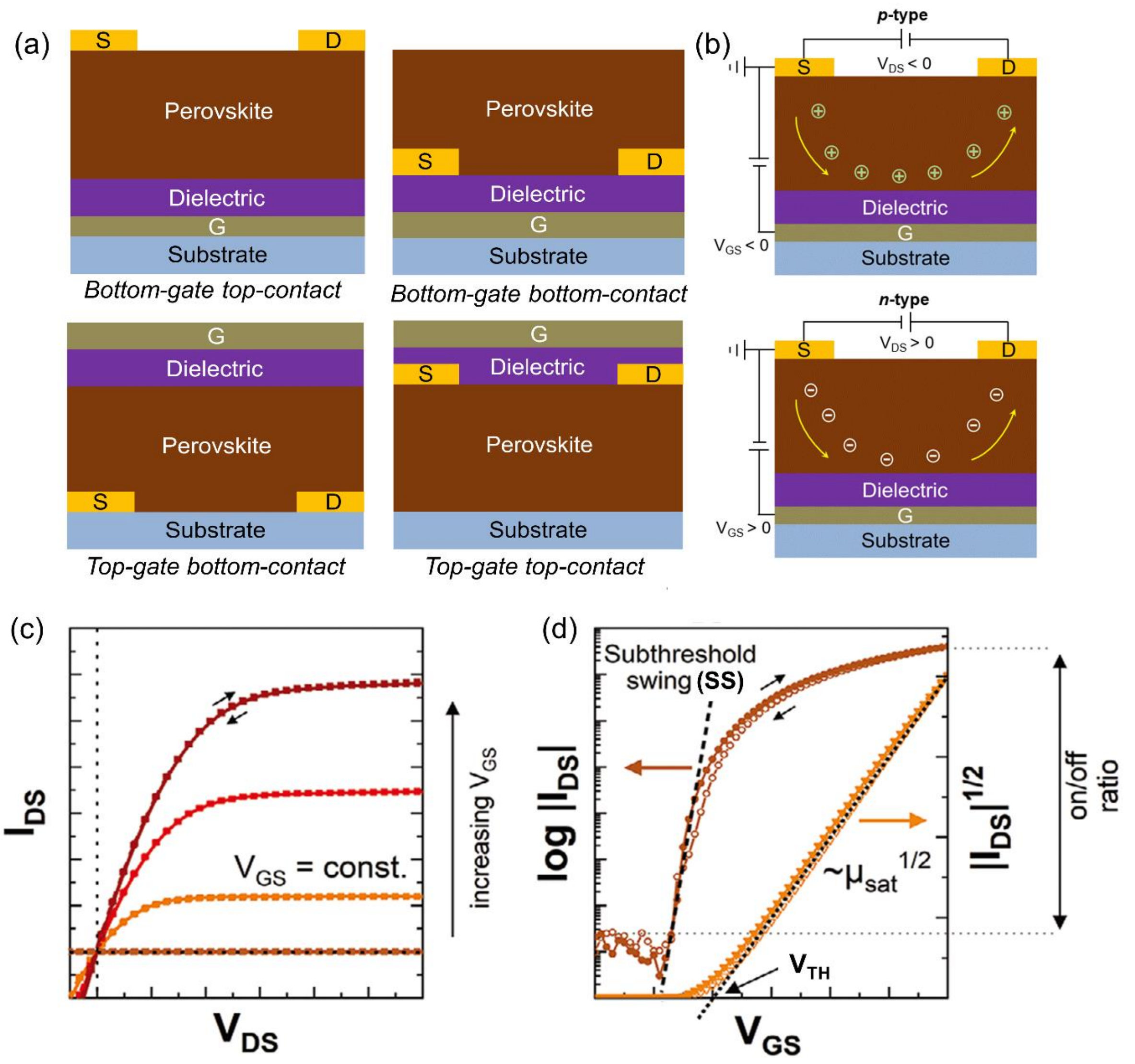

Figure 1.9. (a) Commonly employed FET architectures with perovskite as semiconducting material. (b) Classification of FETs based on *p*- or *n*-type charge carrier. (c) Corresponding output characteristics (sweeping V_{DS} while V_{GS} = constant value) and (d) transfer characteristics (sweeping V_{GS} while V_{DS} = constant value) for an ideal FET. [31]

During the operation of a FET device, the applied gate and source voltage (V_{GS}) induces accumulation of charges carrier at the interface between the insulating layer and the semiconductor. Then a current flows in the channel from the S to the D electrode upon application of a S-D voltage (V_{DS}).[71] Unipolar devices utilize either holes (*p*-channel) or electrons (*n*-channel) as major carrier type (Figure 1.9b). To simplify their fabrication, the most commonly used device architecture for perovskite FETs is bottom-gate top-contact (BG-TC) geometry based on silicon/silicon oxide (Si/SiO_2) as bottom-gate electrode and dielectric layer, offering the benefit of a well-defined dielectric layer. In FET devices, the distance between the S and D electrodes (channel length, abbreviated L) typically lies in the range of a few to several hundreds of micrometers and the corresponding channel width (W) of the electrodes ranges typically from several hundred micrometers to a few millimeters.

There are several key parameters that determine the operational properties of a transistor such as: field-effect mobility (μ), threshold voltage (V_{TH}), on/off current ratio ($I_{ON/OFF}$), and sub-threshold swing (SS). The above electrical parameters in FET devices can be significantly influenced by several factors, such as device geometry, materials property, and film morphology of the semiconductor. In general, high μ, low V_{TH}, large $I_{ON/IOFF}$, and small SS values are prerequisites for a well working transistor.[72] The mobility of a transistor is the first important parameter in determining how efficiently charge carriers can be transported along the conducting channel. It is described as the average charge carrier drift velocity per unit electric field, in units of $cm^{-2}V^{-1}s^{-1}$. The performance of FETs is usually characterized by measuring the output (I_{DS} vs. V_{DS}) (Figure 1.9c) and transfer (I_{DS} vs. V_{GS}) (Figure 1.9d) characteristics. In unipolar FET devices with hole- or electron-dominated transport, once the applied V_{GS} surpasses the threshold voltage V_{TH}, the accumulation of charge carriers occurs at the semiconductor/dielectric interface and the overall charge carrier density is proportional to (V_{GS}-V_{TH}). The applied V_{GS} and the nature of the injecting contact between semiconducting layer and S-D electrodes determine the amount of majority carriers in the channel. Consequently, a common model of FETs provides the total channel current I_{DS} in the linear regime at low V_{DS} << V_{GS}-V_{TH} can be expressed via the following equation[73]:

$$I_{DS,linear} = \frac{W}{L} C_a \mu [(V_{GS} - V_{TH}) V_{DS}] \qquad \text{(Equation 1.3)}$$

where C_a is the capacitance per unit area of the dielectric layer. The charge carrier mobility μ in the linear regime can be calculated by:

$$\mu_{linear} = \frac{\partial I_{DS}}{\partial V_{DS}} \cdot \frac{L}{W C_a V_{DS}} \qquad \text{(Equation 1.4)}$$

When $V_{DS} > V_{GS}$-V_{TH}, the charge density at the drain electrode becomes zero. Further increase in V_{DS} results in a "pinch-off" of the channel and a constant channel current, typically referred to as the "saturation regime", which will be discussed later. In the saturation regime at high V_{DS}, the I_{DS} can be expressed via the Equation:

$$I_{DS,saturation} = \frac{W}{2L} C_a \mu (V_{GS} - V_{TH})^2 \qquad \text{(Equation 1.5)}$$

The charge carrier mobility μ in the saturation regime can therefore be extracted from the following Equation:

$$\mu_{saturation} = \frac{2L}{WC_a} \left(\frac{\partial\sqrt{I_{DS}}}{\partial V_G}\right)^2 \qquad \text{(Equation 1.6)}$$

The charge carrier mobility μ is calculated in either the saturation or the linear regime from the above two equations. It should be pointed out that in an ideal FET device, the mobility calculated in the linear and saturation regimes are identical. The threshold voltage V_{TH} is another important parameter to evaluate the performance of FET devices. V_{TH} can be considered as the minimum gate voltage V_{GS} required for accumulating the charges at the semiconductor/insulator interface, creating a conducting pathway between the S-D electrodes. V_{TH} can be extracted from the transfer curves by determining the x axis intercept of $\sqrt{(I_{DS})}$ versus V_{GS} in the saturation regime. In general, V_{TH} needs to be controlled to ensure proper operation of the device. Low V_{TH} indicates reduced power consumption of the device, and is, thereby, beneficial for portable devices and integrated circuits. Another figure of merit in a FET device is the on/off current ratio $I_{ON/OFF}$, defined as the ratio between the on and off I_{DS}. The $I_{ON/OFF}$ indicates the switching performance of the FET, whereby a high value is desired for practical applications. The sub-threshold swing SS is also one of the key parameters that determines an efficient usage of the transistor as an electrical switch and reflects the quality of the semiconducting film. In fact, SS is more complicated in perovskite FETs due to the mixed ionic and charge conduction. Therefore, the non-ideal behavior and deviation from the above discussion could potentially lead to overestimation or underestimation of the charge carrier mobility and other parameters, which should be carefully analyzed.

1.3 2D tin halide perovskites for FET applications

Despite the huge progress made for perovskite semiconductors in solar cells and light-emitting diodes, the development of perovskite FETs is far behind in both performance and reliability. To date, a significantly smaller community reports the application of perovskite materials for FETs, in spite of the fact that the first manuscript on perovskite FETs preceded all reports on other device applications.[74] One of the possible reasons is ion migration in perovskites, which screens the applied gate electric field, and yields a low field-effect mobility and large current-voltage hysteresis, posing a major difficulty for the fabrication of reliable FETs.[75] Additionally, the poor stability of perovskites further hinders the development of perovskite FETs. Together with these limitations, it remains a huge challenge to understand and investigate the charge transport properties in perovskites by FETs. Nevertheless, the expected high charge mobility, long carrier diffusion length, and the ease of preparation as demonstrated for solar cells and other electronic devices, motivate and sustain the research on perovskite FETs.

Replacing the toxic Pb on the B-site with various alternative divalent metallic cations in 2D perovskites for optoelectronic devices applications has motivated a lot of research. Various candidates such as, tin (Sn), germanium (Ge), bismuth (Bi), stibium (Sb), and copper (Cu) have been proposed to prepare Pb-free perovskites for electronic devices.[76] Among these alternatives, Sn-based perovskites demonstrate similar properties like Pb-based analogues and offer great potential for eco-friendly industrial applications. Specifically, Sn and its neighbor Pb both belong to the same group 14 of the periodic table of elements, adopting a similar outer electron configuration ns^2np^2 (n = 5 for Sn and n = 6 for Pb). The divalent state of the Sn^{2+} cation has a roughly comparable radius (~1.35 Å) compared with Pb^{2+} (~1.49 Å), which allows for the replacement of Pb by Sn while retaining a stable structure with negligible perovskite lattice perturbation.[77] Moreover, Sn-based perovskites exhibit similar optical and electronic properties compared to the Pb-based counterparts. Some of them are even superior with regard to the device performance of solar cells, such as higher charge carrier mobility and smaller exciton binding energy. These unique properties make Sn-based perovskites promising semiconductors for potential FET applications. Previous studies reveal that pure Pb-based 2D perovskites do not show field-effect behavior at room temperature.[78] Compared to the Pb-based 2D perovskite, the Sn counterpart has a high field-effect mobility with smaller in-plain effective mass value and longer carrier lifetime. Based on the Drude-Smith equation, at fixed temperature the charge carrier mobility in the semiconductor is expressed by the following equation[79]:

$$\mu = \frac{q\tau}{m^*} \qquad \text{(Equation 1.7)}$$

where q is the elementary charge; τ stands for the carrier lifetime; and m* is the carrier effective mass. Larger τ and smaller m* values thus increase the charge carrier mobility in the perovskite. This further demonstrates the benefit of Sn in the perovskite structure.

Kagan et al. firstly reported the 2D hybrid perovskite FETs in 1999 based on a spin-coated $(PEA)_2SnI_4$ film.[74] A maximum hole mobility of 0.62 $cm^2V^{-1}s^{-1}$ at room temperature was observed (Figure 1.10a). Later, the same group further improved the device mobility of 2D hybrid perovskite FETs by using new spacer cations and process optimization.[80] Surprisingly, there is a relatively large time gap of more than ten years of reports on 2D Sn-based perovskite FETs. Probably sparked by the impressive progress achieved in other perovskite electronic devices as solar cells, recently, 2D Sn-based perovskite FETs have ushered a new era of renewed efforts with increased mobility and stability. In 2016, Adachi's group reported a high-performance 2D $(PEA)_2SnI_4$ perovskite FET with maximum field-effect hole mobility of 15 $cm^2V^{-1}s^{-1}$ and negligible hysteresis by device and process optimization, including the use of a self-assembled monolayer, modification of the device geometry, and introduction of a charge injection layer (Figure 1.10b).[81] Later, the hole mobility was further substantially improved to 40 cm^{2}V^{-1}s^{-1} by employing large single crystals of (PEA)$_2$SnI$_4$.[82] Interestingly, 2D (PEA)$_2$SnI$_4$ perovskite FETs also show *n*-channel characteristics (Figure 1.10c). By inserting a C$_{60}$ interlayer between the S-D electrodes and semiconducting film, the device showed pronounced *n*-type behavior and exhibited an electron mobility of 0.9 cm^{2}V^{-1}s^{-1} at room temperature.[83]

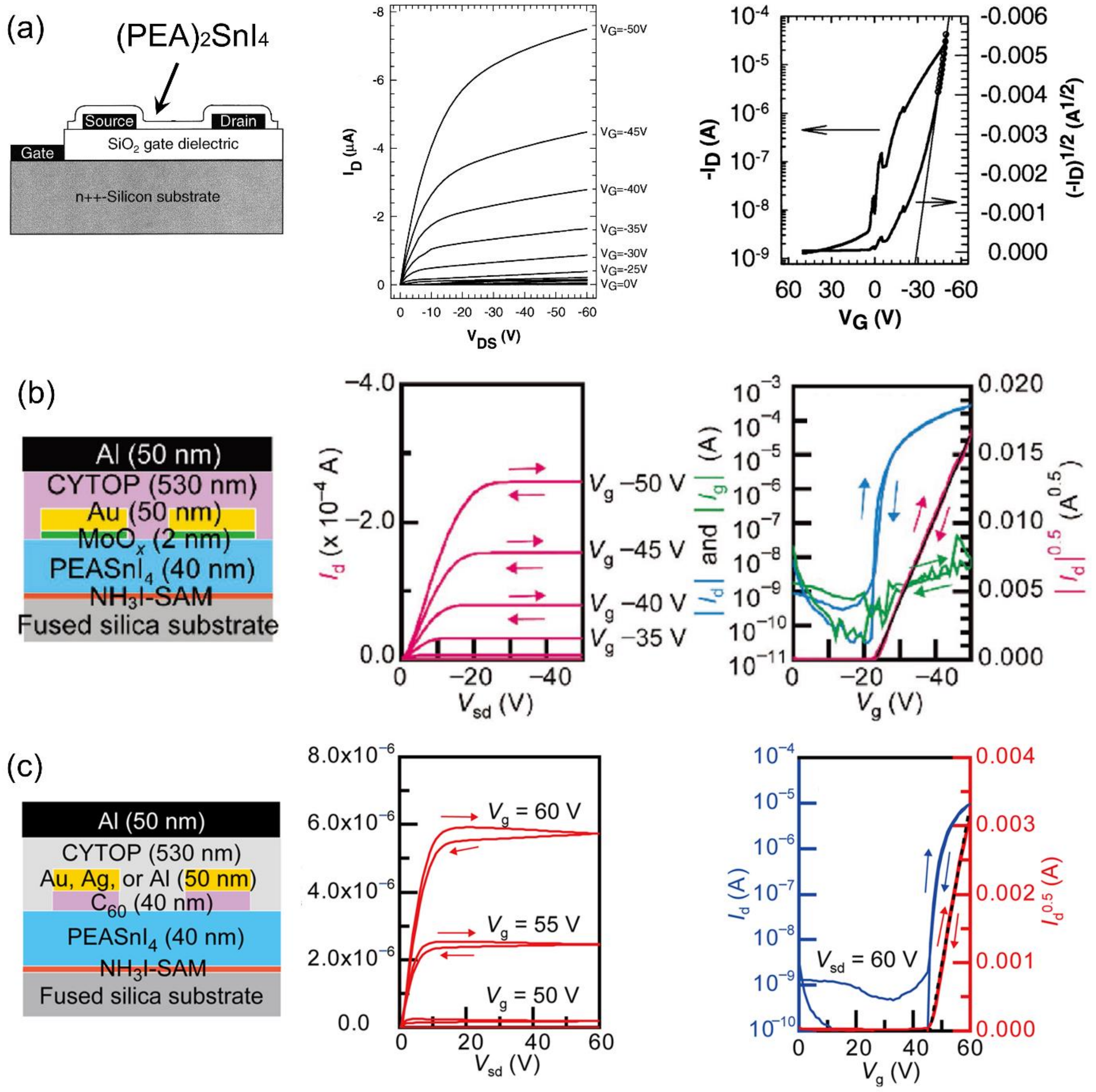

Figure 1.10. Three representative cases for the development of 2D Sn-based perovskite FETs. (a) The first report about the 2D perovskite FET with (PEA)$_2$SnI$_4$ semiconducting layer.[74] (b)

Top-gate top-contact 2D $(PEA)_2SnI_4$ perovskite FET with high hole mobility and negligible hysteresis.[81] (c) *n*-type 2D perovskite FET with C_{60}/Au contacts exhibited electron transport.[83]

After more than a decade gap on the research of perovskite FET devices, remarkable progress has been made in the development of 2D Sn-based perovskite FETs. The continuous efforts on the improvement of the device performance are beneficial for a better understanding of 2D Sn-based perovskite materials and devices that can become excellent candidates for high-quality transistors.

1.4 Device physics of 2D tin halide perovskite FETs

Although some progresses have been made for 2D tin halide perovskite FETs, many of their intrinsic properties, such as ion migration and low-temperature device performance still remain unclear. Analyzing and understanding these phenomena in 2D tin halide perovskite FETs are of great importance to turn perovskite FETs into serious contenders for electronic circuits and other types of electronic device applications. Originating from the ion movement and defects, charge carrier dynamics in perovskites show complicated processes. Particular attention should be paid to the characterization conditions of perovskite FETs, such as measurement mode and temperature (Figure 1.11). Suffering from severe ion migration, the charge carrier mobility in perovskite FETs is limited. The stability issue by extrinsic factors such as light, water, and oxygen, is still not extensively investigated. These major obstacles significantly delayed their commercial deployment.

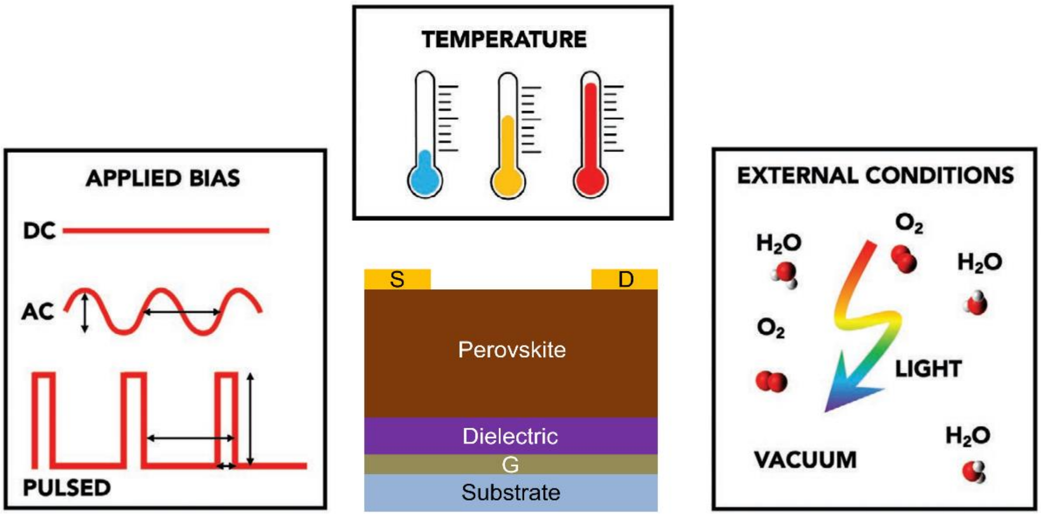

Figure 1.11. Summary of different measurement conditions for perovskite FET devices.[84]

Traditional organic FETs are typically characterized in a continuous direct current (DC) mode. It takes tens of seconds or few minutes for the entire measurement with dual-sweeping. In perovskite transistors, however, the migration of ionic species can be easily observed at room temperature owing to their low activation energies. The application of biases with a long period of time inevitably lead to ion migration induced screening of the electric fields, and consequently reducing the gate modulation and charge carrier mobility. Considering the much larger motion speed of electrons/holes as compared to ions, in principle, a negligible ionic current can be obtained by a high scan rate during the electrical characterization.[85] Nevertheless, the research on perovskite solar cells have demonstrated that the device performance can be overestimated by applying fast sweep rates of several volts per second.[86] Similarly, in FETs the key parameters including charge carrier mobility and hysteresis might be artificially manipulated. In order to investigate the device parameters of polycrystalline perovskite thin film transistors at room temperature, the electrical measurement conditions should be carefully checked in the presence of complicated structural defects and mixed charge/ionic transport. Pulse mode is believed to be a powerful tool and an effective approach to investigate the electronic characteristics of perovskite FET devices by reducing the influence of ion movement. In pulse mode the pulse width, frequency, and integration times can be tailored (Figure 1.12). By applying voltage pulses instead of using a continuous sweep, it is possible to gain important information about the carrier dynamics and charge transport. At each step of the pulse mode, the pulse width and delay time are important to characterize the electronic and ionic transport, as well as charge carrier trapping and detrapping events. For example, when a short pulse is applied to the gate bias, the time scale of the accumulation of charges at the dielectric interface is much faster than the accumulation of ions. Due to this distinct difference in dynamics of ions and charges, hence, detailed pulse measurements are essential to elucidate the mechanism of charge and ion transport in 2D tin halide perovskite FETs.

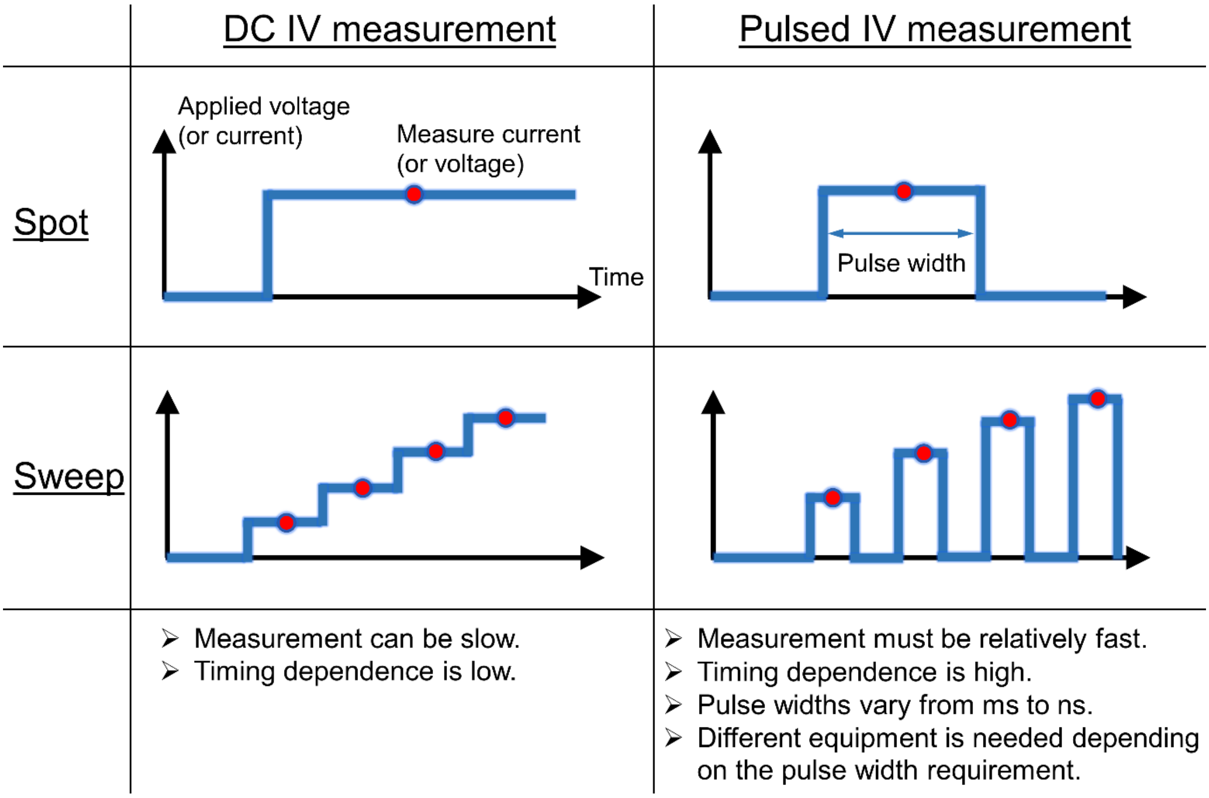

- Measurement can be slow.
- Timing dependence is low.

- Measurement must be relatively fast.
- Timing dependence is high.
- Pulse widths vary from ms to ns.
- Different equipment is needed depending on the pulse width requirement.

Figure 1.12. Illustration of continuous and pulse mode with spot or sweep scanning for transistor measurement.

Temperature is another important parameter for the FET characterization. Temperature dependent measurements can provide important information about the charge transport mechanism in perovskite materials. Earlier studies on 3D perovskite FETs showed that the migration of mobile ionic defects, which screen the gate field and reduce electronic transport in the channel, is thermally activated and thus can be suppressed upon decreasing the temperature during device measurement.[87] Liu et al. investigated quasi-2D perovskite $(BA)_2(MA)_{n-1}Pb_nI_{3n+1}$ single crystal FET devices with varying n = 1, 2, and 3.[88] Due to severe ion migration in this lead halide perovskite, it was not possible to observe any field-effect response at room temperature. The authors carried out temperature-dependent electrical measurements from 80 K to 160 K, as presented in Figure 1.13a. The dual-sweep hysteresis declined significantly as the temperature decreased, suggesting that the low temperature can effectively inhibit the ion migration. The extracted effective electron mobility exhibited a lower mobility at higher temperature which might be ascribed to phonon scattering. For 2D tin halide layered perovskite FETs, benefiting from recent advances in material and device engineering, the transistors show more reliable behavior with low hysteresis and high charge mobility at room temperature, thus, with only few reports focusing on low temperature device performance.

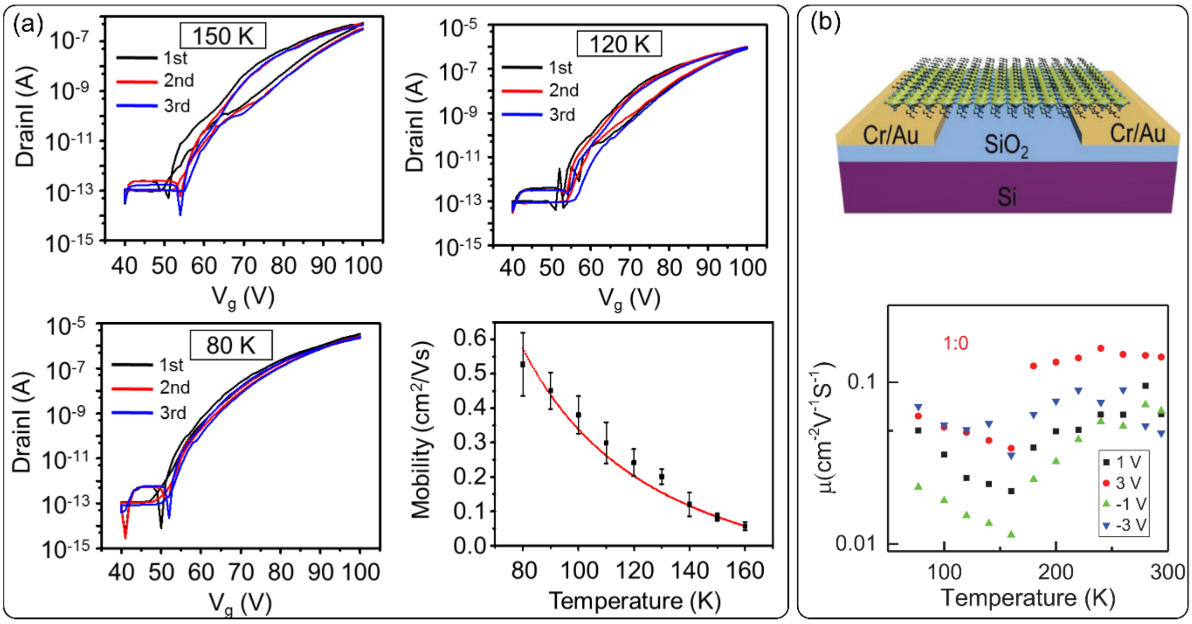

Figure 1.13. (a) 2D lead-halide single crystal perovskite FETs measured at 150 K, 120 K, 80 K with three scans to guarantee reliability, and corresponding field-effect electron mobility extracted from transfer curves at different temperatures;[88] (b) Schematic of the bottom-gate, bottom-contact 2D $(BA)_2SnI_4$ perovskite microplate FET and the temperature-dependent hole mobility under different source-drain bias.[89]

Wang et al. studied the charge transport mechanism in perovskite FETs based on 2D $(BA)_2SnI_4$ crystals (Figure 1.13b).[89] It was revealed that the field-effect hole mobility showed a continuous decrease when the temperature increases from 77 K to 160 K, resulting in a negative temperature coefficient. Meanwhile, the mobility constantly increases at higher temperature from 180 K to 295 K. At around 180 K the mobility showed an abrupt change, possibly due to an orthorhombic-to-orthorhombic phase transition. The mobility decrease below 160 K with elevating temperature was indicative of reduced carrier-phonon scattering. The enhanced mobility with temperature above 180 K was possibly due to different mechanisms, such as thermal activated charge transport or the formation of small polarons resulting from the strong electron-phonon interaction. Therefore, temperature dependent studies provide important details about the charge carrier transport properties in perovskites. Low temperature measurements are necessary in the future for a better understanding of charge carrier injection and transport in order to make this class of materials an excellent candidate for cost-effective and high-quality transistor applications.

Other parameters during the measurements, such as the effect of light can also not be neglected because perovskites are photoactive materials. The light induces the generation of free charge carriers due to the low exciton binding energy in these materials. Previous works have demonstrated that perovskite FETs are sensitive to light, which can increase the channel current by several orders of magnitude.[88] This unique property of perovskites has triggered huge interests in the study of phototransistor devices. Therefore, it should also be considered that dark conditions are necessary when regular FETs are characterized to avoid the contribution of the photo-generated charge carriers to the field effect mobility.

1.5 Challenges for 2D tin halide perovskite FETs

To date, the study of 2D tin halide layered perovskite FETs is still at a very preliminary stage, with many challenges being open. These issues include (i) intrinsic properties of perovskite materials, (ii) grain boundaries, (iii) interface between semiconducting layer and source-drain electrodes, and (iv) interface between semiconducting layer and dielectric layer (Figure 1.14a).[90] Therefore, insights into the fundamental material issues, such as crystallinity, orientation, ionic defects, and ion migration are highly desirable for obtaining high-performance perovskite FETs. The complexity of the carrier dynamics in 2D tin halide perovskites from quantum and dielectric confinement to ion migration requires a particular attention to optimize the FET performance. Note that, despite the progress in performance improvement of 2D tin halide perovskite FETs, the mobility and stability are still far behind that of traditional organic and inorganic FETs. The relatively poor device performance mainly stems from the poor quality of the solution processed films, which is attributed to oxidation and fast crystallization, generating a high density of charge carrier traps by ionic defects and inferior morphologies.

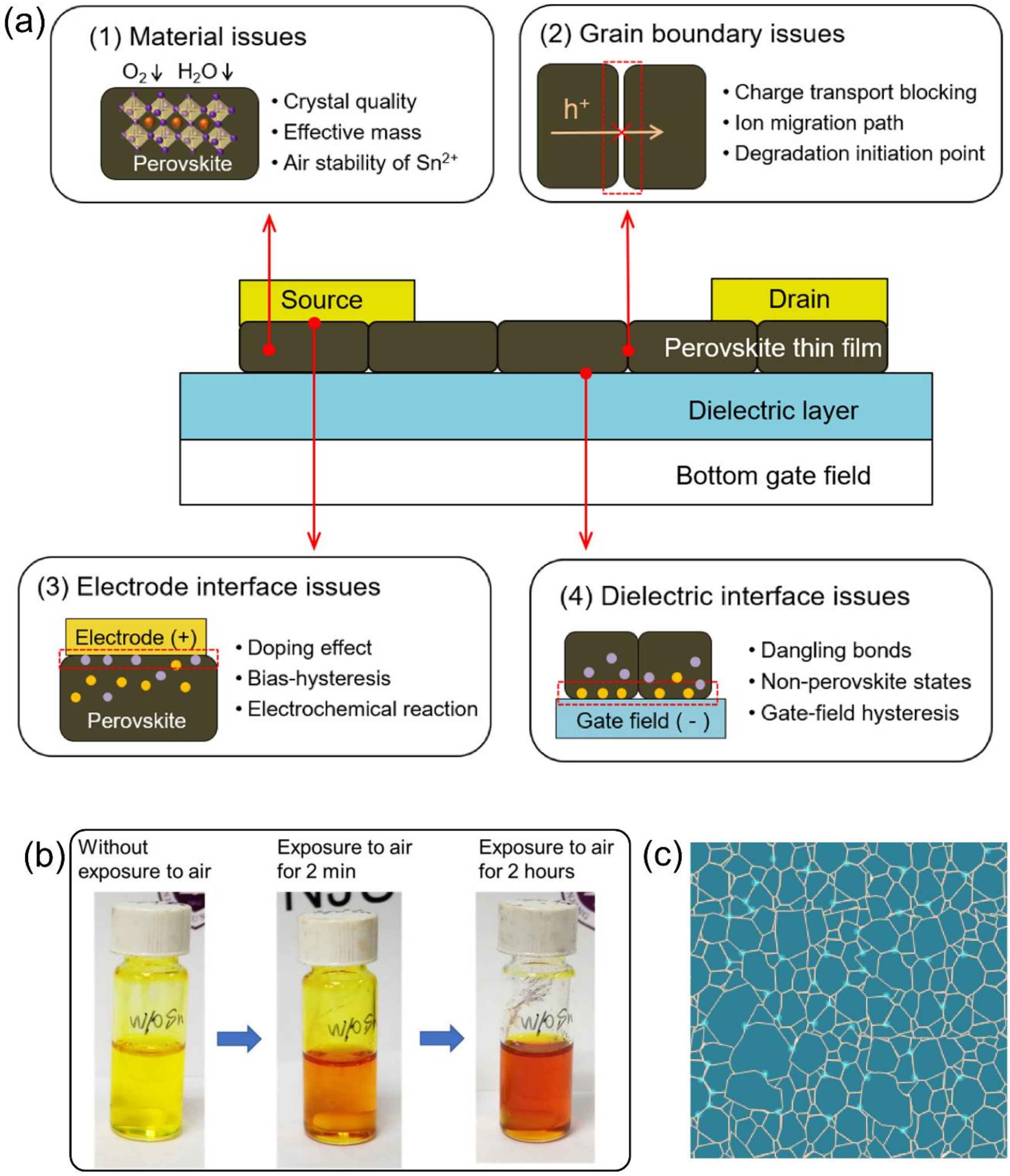

Figure 1.14. (a) Illustration of main issues for the optimization of metal halide perovskites in FETs application;[90] (b) Photographs showing the ease of oxidation of Sn^{2+} to Sn^{4+} in ambient air;[91] (c) Schematic demonstration of typical inferior film morphology with small grain size and pinholes of 2D tin halide perovskite thin films.

The easy oxidative conversion of Sn from its +2 to +4 state is the first problem of 2D tin halide perovskite FETs. Specifically, Sn contains the electron configuration of $5s^2 5p^2$, where the two electrons on the 5s orbital of Sn^{2+} exhibit the active pair effect tending to be lost easily and giving rise to the easy oxidation to Sn^{4+}.[91] As shown in Figure 1.14b, the fresh yellow perovskite precursor solution rapidly becomes orange-red under exposure to air for several minutes. Leijtens et al. investigated and summarized the oxidation reaction mechanism for pure Sn perovskites as $2SnI_2 + O_2 \rightarrow SnO_2 + SnI_4$.[92] Sn^{4+} is generally considered as an ionic defect in the film. The oxidation issue causes short charge carrier lifetimes and thus short carrier diffusion lengths, leading to poor charge transport properties in tin halide perovskite films. There are several sources for Sn^{4+} impurities like for example in the commercial materials, precursor solution, and during film deposition. It has been reported that even the highest-purity (99.999%) commercial SnI_2 exhibited a substantial amount of Sn^{4+}. Additionally, Saidaminov et al. reported that the conventional solvent DMSO (formula: $(CH_3)_2SO$) can oxidize Sn^{2+} at the temperatures above 100 °C by the following reaction in the precursor solution: $2SnI_2 + 2(CH_3)_2SO \rightarrow SnO_2 + SnI_4 + 2(CH_3)_2S$.[93] The oxidation inevitably takes place during the film processing in the glovebox even at the presence of only minor oxygen traces. Additionally, the energetically unfavorable *s-p* antibonding coupling between 5s of Sn and 6p of I leads to the low formation energies of Sn vacancies. These two factors contribute to the easy formation of Sn defects during the film crystallization process.

The second challenge for 2D tin halide perovskite films is the hardly controllable crystallization process, which originates from the unique property of Sn^{2+} of high Lewis acidity due to the high energy of its 5p orbital, resulting in the rapid reaction rate of SnI_2 with organic cation salts. The high Lewis acidity and the easy oxidation of Sn^{2+} significantly facilitate the nucleation and growth rate of perovskite crystals from precursor solution leading to inferior morphology of perovskite films with high density of defects, small grains, and large number of pinholes (Figure 1.14c).[94] The above discussion indicates that the issues including the fast crystallization, easy oxidation of Sn^{2+} and formation of Sn vacancies during film processing should be well-handled to improve the film quality of Sn-based perovskites. Unlike the field of perovskite solar cells and light-emitting devices, where many different strategies have been investigated, only relatively few have been implemented and explored in perovskite FETs, possibly due to different operating mechanisms as discussed before.

1.6 Optimization of 2D tin halide perovskite FETs

To overcome the above challenges of 2D tin halide perovskites, to date, researchers have developed several strategies to regulate the crystallization process, suppress ion migration and enhance the field-effect mobility. These approaches include solvent engineering, spacer cation tuning, and doping.

1.6.1 Solvent engineering

Solvent engineering has been demonstrated to be a powerful approach to regulate the crystallization in Sn-based perovskite solar cells by controlling the solvent parameters, such as solubility, polarity, boiling point, viscosity, and others.[95] The 2D tin halide perovskite precursor solution is usually prepared by dissolving the two source materials SnI_2 and organic cation salt into the solvent DMF. However, in the conventional method with pure DMF, the $(PEA)_2SnI_4$ perovskite crystals are formed immediately after spin coating leading to the poor morphology. Therefore, it is essential to keep the balance between nucleation rate and growth rate of perovskite crystals. This is possible by choosing solvents with different properties. Previous reports revealed that the tin halide perovskite precursor solution can be prepared with polar solvents to form the Lewis acid-base intermediate phase, where the bond strength of this intermediate can significantly influence the crystallization process of the perovskite crystals. Therefore, introduction of solvents with high basicity is an effective method to control the crystallization of 2D Sn-based perovskites by adjusting the bonding strength of Lewis acid-base coordination.

Zhu et al. reported controlled crystallization of 2D $(PEA)_2SnI_4$ perovskite and improved FET performances by employing the mixed solvent DMF:DMSO (Figure 1.15a).[95] When spin-coated from pure DMF the film color became dark brown during processing, while the film deposited from the mixed solvent was firstly light-yellow during spin-coating and changed to dark brown during thermal annealing indicating an intermediate phase prior to the formation of the perovskite phase. It was demonstrated that DMSO with an oxygen donor as Lewis base bears strong coordination ability by donating a lone pair of electrons, leading to the formation of a Lewis acid-base adduct. As a result, the uncoordinated tin ions and/or tin clusters could be effectively reduced, along with suppressed anti-site defects, enhanced crystallinity with larger crystallite size, and improved film morphology. Consequently, the approach of mixed solvents significantly improved the mobility of $(PEA)_2SnI_4$ FETs from 0.7 $cm^2V^{-1}s^{-1}$ to 3.5 $cm^2V^{-1}s^{-1}$.

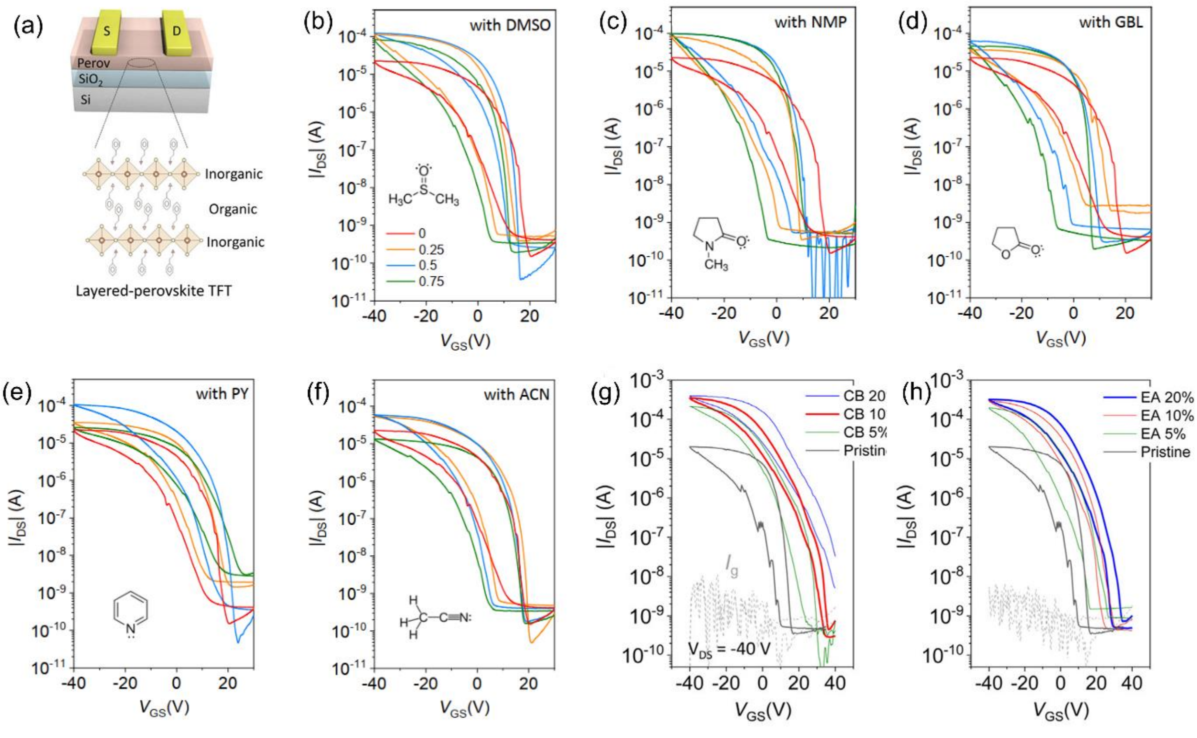

Figure 1.15. (a) Schematic of 2D perovskite FETs based on $(PEA)_2SnI_4$ semiconducting layer. Transfer characteristics of pristine and optimized device by the solvents of (b) DMSO; (c) NMP; (d) GBL; (e) PY; (f) ACN; (g) CB; and (h) EA with different volume ratios.[95,96]

Based on a similar strategy, two more oxygen-donor Lewis bases N-methyl-2-pyrrolidone (NMP), and gamma-butyrolactone (GBL), as well as nitrogen-donor Lewis bases pyridine (PY) and acetonitrile (ACN) were further systematically investigated by Zhu et al., as shown in Figure 1.15c-f.[95] The results revealed higher crystallinity and improved morphology for the $(PEA)_2SnI_4$ films obtained from the mixed solvents in comparison to pure DMF. The device with oxygen donor Lewis bases NMP and GBL exhibited improved FET mobilities of 2.9 and 1.8 $cm^2V^{-1}s^{-1}$ under optimized conditions. The nitrogen donor Lewis bases, PY and ACN, also increased the mobilities to 1.9 and 1.0 $cm^2V^{-1}s^{-1}$, respectively.

Additionally, Zhu et al. further reported an easy and highly repeatable binary solvent method to prepare high-performance $(PEA)_2SnI_4$ transistors by adding chlorobenzene (CB) and ethyl acetate (EA) into DMF.[96] As shown in Figure 1.15g and h, the transfer curve of the pristine perovskite FET from pure DMF showed several zigzag current steps in the reverse scanning, which were ascribed to the detrapping of captured charge carriers. In contrast, the binary solvents DMF:CB and DMF:EA based FETs showed a significantly improved maximum channel current I_{DS}, larger $I_{ON/OFF}$ and smaller dual-sweep hysteresis. Particularly, the sample from DMF:10% CB exhibited a mobility of 3.1 $cm^2V^{-1}s^{-1}$. The addition of the much less toxic solvent EA provided the same effect on the device performance and the FET with optimized DMF:20% EA yielded the highest mobility of 3.8 $cm^2V^{-1}s^{-1}$. The improvement of overall device parameters by using mixed solvents was due to the enhanced film quality with full coverage and low defect density. The nucleation was promoted with more oriented grains during spin-coating by adding CB/EA to the precursor solution.

1.6.2 Spacer cation engineering

The 2D tin halide layered perovskites show a low theoretical charge carrier mobility as compared to 3D perovskites due to the dielectric confinement effect by bulky organic spacer cations. But this can be turned into an advantage since such organic cations can be chemically tailored by different chemical structures, opening the door to a plethora of new layered structures with various functionalized features. Furthermore, chemical tuning of organic cations has been proven to be beneficial for improving the device performance of tin halide perovskite optoelectronic devices such as solar cells or light-emitting diodes. To date, the RP structure of

2D tin halide layered perovskites is the mostly reported one due to its structural freedom to accommodate a rich library of organic monocations. Despite some progress has been achieved, the cation engineering for perovskite devices is highly limited since there is no systematic understanding of the effects of the spacer cations on the crystal structure, charge transport properties, and device performance. Therefore, it is difficult to predict the resulting structure of these synthetic experiments, hindering the discovery of novel 2D perovskite materials to be incorporated into high-performance devices.

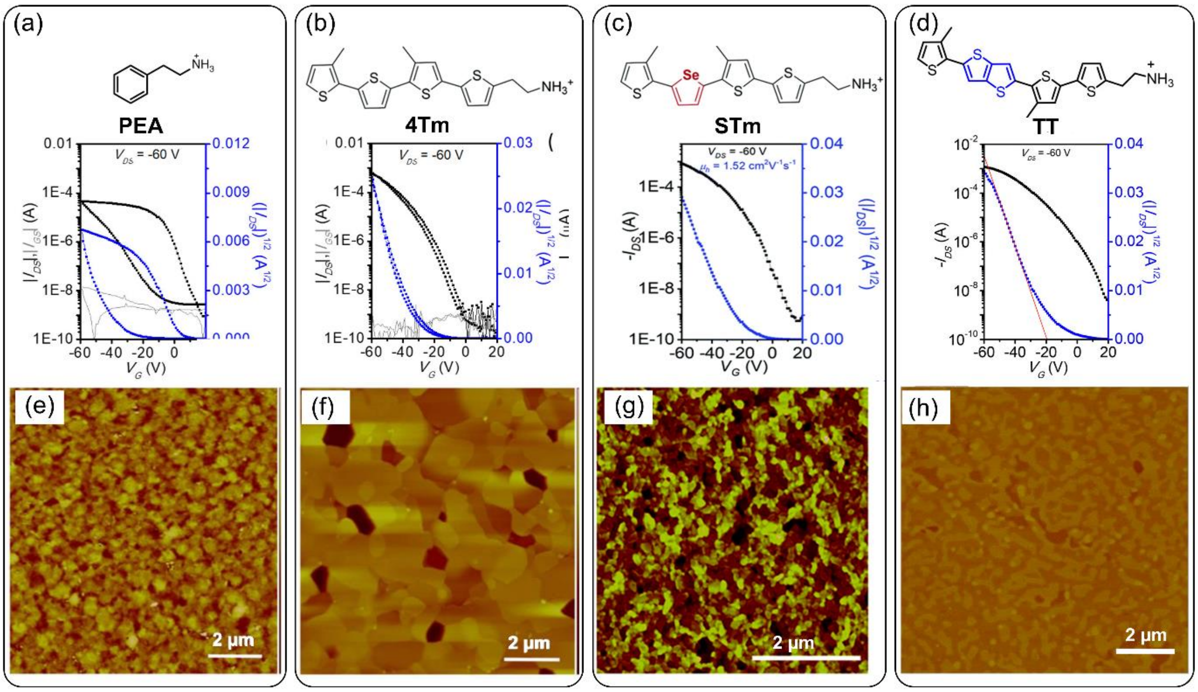

Figure 1.16. Chemical structures of organic cations (a) PEA,[97] (b) 4Tm,[97] (c) STm,[98], and (d) TT,[99] and their transfer characteristics in 2D Sn-based perovskite FETs. The corresponding AFM imgaes of (e) $(PEA)_2SnI_4$, (f) $(4Tm)_2SnI_4$, (g) $(STm)_2SnI_4$, and (h) $(TT)_2SnI_4$ thin films.

The spacer cation PEA has been extensively studied in 2D tin halide perovskite FETs and different optimization methods have been employed to improve the corresponding device performance of $(PEA)_2SnI_4$ FETs (Figure 1.16a). Gao et al. reported a 2D tin halide perovskite featuring a linear π-conjugated oligothiophene ligand in bottom-gate/top-contact FETs, namely, $(4Tm)_2SnI_4$, where 4Tm is a quaterthiophene-based cation, 2-(3‴,4′-dimethyl-[2,2′:5′,2′:5″,2‴-

quarterthiophen]-5-yl)ethan-1-ammonium (Figure 1.16b).[97] Concerning the device performance, $(PEA)_2SnI_4$ yielded a maximum hole mobility of 0.15 $cm^2V^{-1}s^{-1}$ at room temperature. In contrast, for $(4Tm)_2SnI_4$ FETs an overall improved field-effect behavior was observed. A high on/off current ratio of 10^6, a smaller subthreshold swing SS of 10 V dec^{-1}, and a lower leakage current of 10^{-10} A were achieved. By a systematic optimization of the annealing temperature and film thickness the hole mobility of $(4Tm)_2SnI_4$ FETs went up to 2.32 $cm^2V^{-1}s^{-1}$, which was one order of magnitude higher than for $(PEA)_2SnI_4$. Meanwhile, $(4Tm)_2SnI_4$ exhibited ideal transfer curves with a much smaller hysteresis indicating that the bulky 4Tm cation was beneficial to suppress ion migration and reduce trap states in the perovskite film. Additionally, the $(4Tm)_2SnI_4$ thin film exhibited improved morphology compared to the $(PEA)_2SnI_4$ (Figure 1.16e and f).

Wei et al. of the same group further designed and synthesized a selenophene-containing conjugated organic ligand, 2-(4′-methyl-5′-(5-(3-methylthiophen-2-yl)selenophen-2-yl)-[2,2′-bithiophen]-5-yl)ethan-1-aminium (STm), for 2D halide perovskites FET applications.[98] Specifically, the third thiophene ring of the 4Tm backbone was swapped to a selenophene ring. The highest occupied molecular orbital (HOMO) level of the STm ligand was investigated by cyclic voltammetry and optical absorption indicating the value of 5.05 eV, which was lower than the one of the 4Tm ligand with 5.12 eV. The introduction of selenophene was expected to facilitate hole injection from the Au electrode (5.0 eV) to the perovskite layer leading to the improved FET performance. As shown in Figure 1.16c, a *p*-type transport behavior was observed with a maximum hole mobility of 1.52 $cm^2V^{-1}s^{-1}$ and an average value of 1.35 $cm^2V^{-1}s^{-1}$ at room temperature, which was comparable to that of the reference $(4Tm)_2SnI_4$ FETs. However, compared with $(4Tm)_2SnI_4$ FET, no obvious enhancement of the device parameters was observed even after systematic optimization of the processing conditions. Based on the film morphology characterization, the reduced performance of $(4Tm)_2SnI_4$ FET was attributed to smaller crystal grains and increased amount of grain boundaries than for $(4Tm)_2SnI_4$-based films (Figure 1.16g). Nevertheless, the FET performance of $(STm)_2SnI_4$ was improved in comparison to $(PEA)_2SnI_4$, demonstrating that the STm cation was a good candidate for electronic and optoelectronic applications.

Later, Liang et al. of the same group further synthesized a lead-free 2D perovskite, namely $(TT)_2SnI_4$, by replacing one thiophene unit in 4Tm with fused thiophene rings (Figure 1.16d).[99] The fused thiophene structures being a highly planar system allows stronger $\pi-\pi$ interactions. The coplanar conformation can also induce the formation of ordered crystalline structures promoting self-assembly and lateral growth of the 2D crystalline film. The crystallization kinetics of $(TT)_2SnI_4$ was controlled by modulating the intermolecular interactions of the organic ligand, leading to a reduced nucleation density during the film crystallization process. Therefore, the $(TT)_2SnI_4$ film revealed large grain size (Figure 1.16h). As a result, highly performing FET devices were achieved with a maximum hole mobility of 9.35 $cm^2V^{-1}s^{-1}$ and a negligible hysteresis.

1.6.3 Doping

Electrical doping is a direct and efficient approach to improve the electrical properties of emerging semiconductors. The term ‘doping’ is broadly used in literature to describe the introduction of any kind of impurity into the semiconductor lattice to control crystal growth and stability or to tune optoelectronic properties. The doping effect is usually achieved through defect formation to provide extra electrons or holes to the lattice.[100] Doping with new components is already reported as an effective method to assist the formation of high quality perovskite films for solar cell applications.[76] The introduction of new components in perovskites has a substantial influence on the crystallization kinetics and the structural stability of perovskites, simultaneously offering enhanced carrier transport characteristics and improved device performance. However, so far its feasibility and mechanism still remain elusive for metal halide perovskites transistors.

Zhu et al. analyzed the structural and optoelectronic properties of traditional $(PEA)_2SnI_4$ perovskites doped with copper iodide (CuI) in FET devices by combining theoretical and experimental methods (Figure 1.17a).[101] The monovalent cation Cu^+ with an ionic radius of 77 pm was chosen in this study, which was slightly smaller than Sn^{2+} (118 pm). The density functional theory (DFT) calculations showed that the crystal structure of pristine $(PEA)_2SnI_4$ consists of a perfect organic-inorganic layered structure with a well-connected SnI_6 octahedral cage. After inserting Cu^+ to replace Sn^{2+} a certain degree of structural variations was observed. DFT calculations disclosed that the incorporation of Cu^+ into $(PEA)_2SnI_4$ results in a destabilized perovskite structure. Interestingly, the CuI-blended perovskite achieved much higher FET performance compared with the pristine one. The Cu^+-doped films revealed an improved electrical performance, with a twofold increase in hole mobility, increased $I_{ON/OFF}$, and reduced hysteresis and SS value, compared to the reference device. It was found that due to the formation of heterostructures in the CuI-$(PEA)_2SnI_4$ composite film, the distribution of CuI in the grain boundaries lowered the trap density and facilitated the charge transport.

Later, Go et al. of the same group used the same strategy by adding 1 vol % sodium iodide (NaI) into $(PEA)_2SnI_4$ perovskite to improve the transistor performance.[102] As presented in Figure 1.17b, the doped NaI-$(PEA)_2SnI_4$ perovskite exhibited reduced dual-sweep hysteresis, and higher hole mobility of 2 $cm^2V^{-1}s^{-1}$ than the pristine device. This device improvement was ascribed to the enhanced film quality, including increased grain size, crystallinity, and higher film coverage of the NaI-$(PEA)_2SnI_4$ film. In addition, NaI effectively passivated the iodine vacancies at the grain boundaries, thereby suppressing the defect and ion migration.

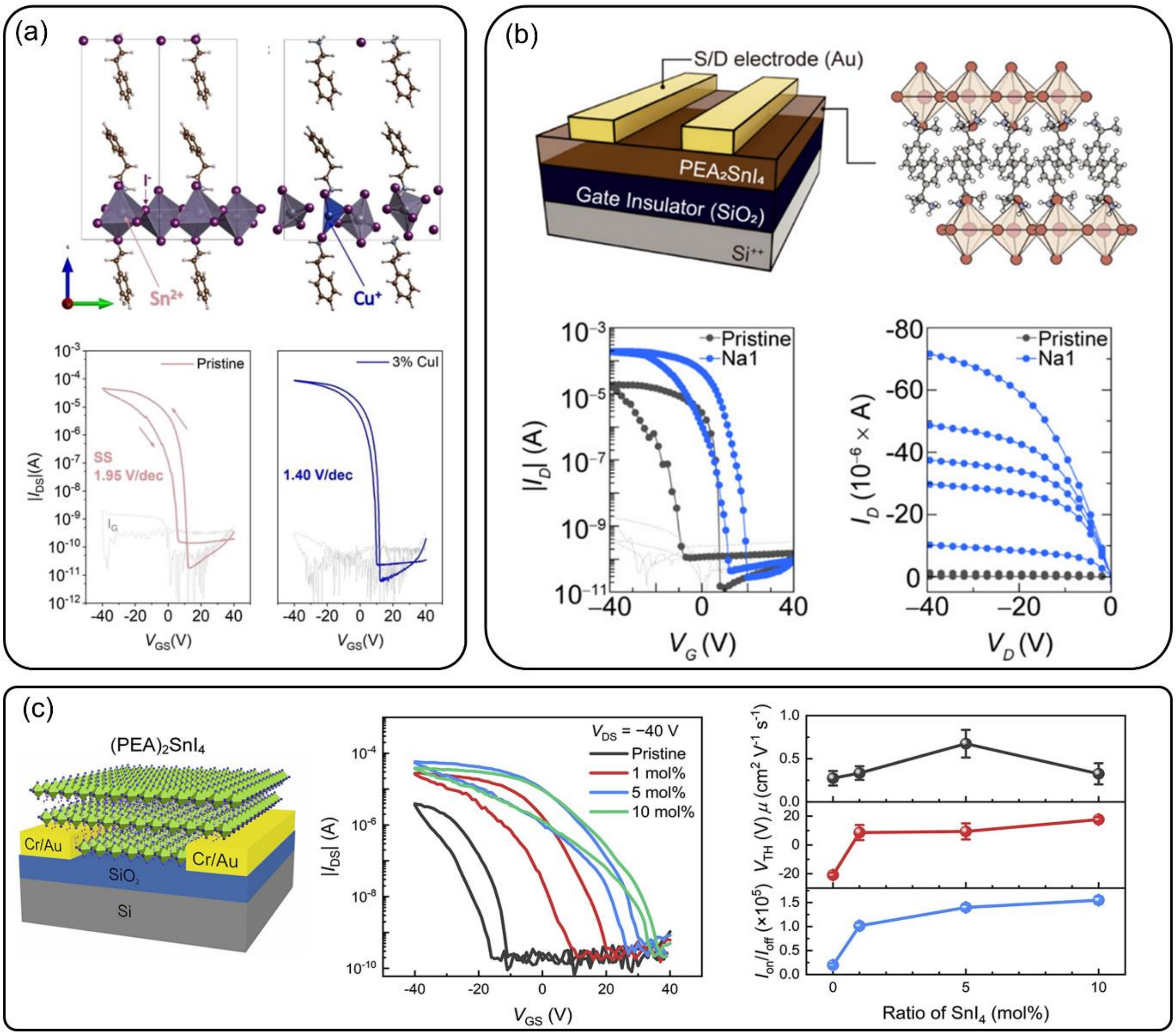

Figure 1.17. (a) Schematic diagram of DFT calculations of $(PEA)_2SnI_4$ with $Sn^{2+}$and Cu^+ and the corresponding transfer curves;[101] (b) Illustration of bottom-gate/top-contact $(PEA)_2SnI_4$ FET and transfer and output characteristics of pristine $(PEA)_2SnI_4$ (black) and NaI doped (blue) devices ($V_{DS} = -40$ V);[102] (c) Device configuration of $(PEA)_2SnI_4$ FET doped with SnI_4 and the corresponding FET performance with different doping ratios.[103]

Liu et al. introduced the SnI_4 dopant to increase the device performance of $(PEA)_2SnI_4$ based FETs, as shown in Figure 1.17c.[103] It was observed that Sn^{4+} *p*-dopes the perovskite and increases the electrical conductivity by 10^5 times as compared to the pristine $(PEA)_2SnI_4$ film. The dopant SnI_4 was also found to improve the film morphology of $(PEA)_2SnI_4$ leading to reduced trap states. By doping the films with SnI_4 in the doping range of 1-5 mol %, a significant enhancement of the device current was achieved, indicating the improvement of device performance. The currents of output curves also increased with higher doping ratios.

However, the doped device showed an increased hysteresis, which was probably attributed to the extra I ions brought by SnI_4 in the films, causing stronger ion migration.

1.6.4 Others

Interface engineering can also serve as an effective approach to reduce defects and ion migration by modifying the interface characteristics or introducing additional interlayers. Matsushima et al. demonstrated that perovskite transistors with untreated SiO_2 exhibited dual-sweep hysteresis during consecutive forward and reverse scans (Figure 1.18a).[81] The large hysteresis was attributed to the movement of mobile ions through the perovskite film. At negative V_{GS}, positive ions gradually moved through grain or crystallite boundaries and accumulated at the gate insulator surface. The gradually accumulated cations act as hole scattering centers and significantly reduce the number of holes in the channel by screening the gate electric field, thereby resulting in large hysteresis of the FET devices. On the contrary, NH_3I self-assembly monolayer (SAM) treatment greatly inhibited the hysteresis, which may be due to the reduced number of mobile ions. Therefore, the device showed overall improved parameters including the mobility, V_{TH}, $I_{ON/OFF}$, and SS values.

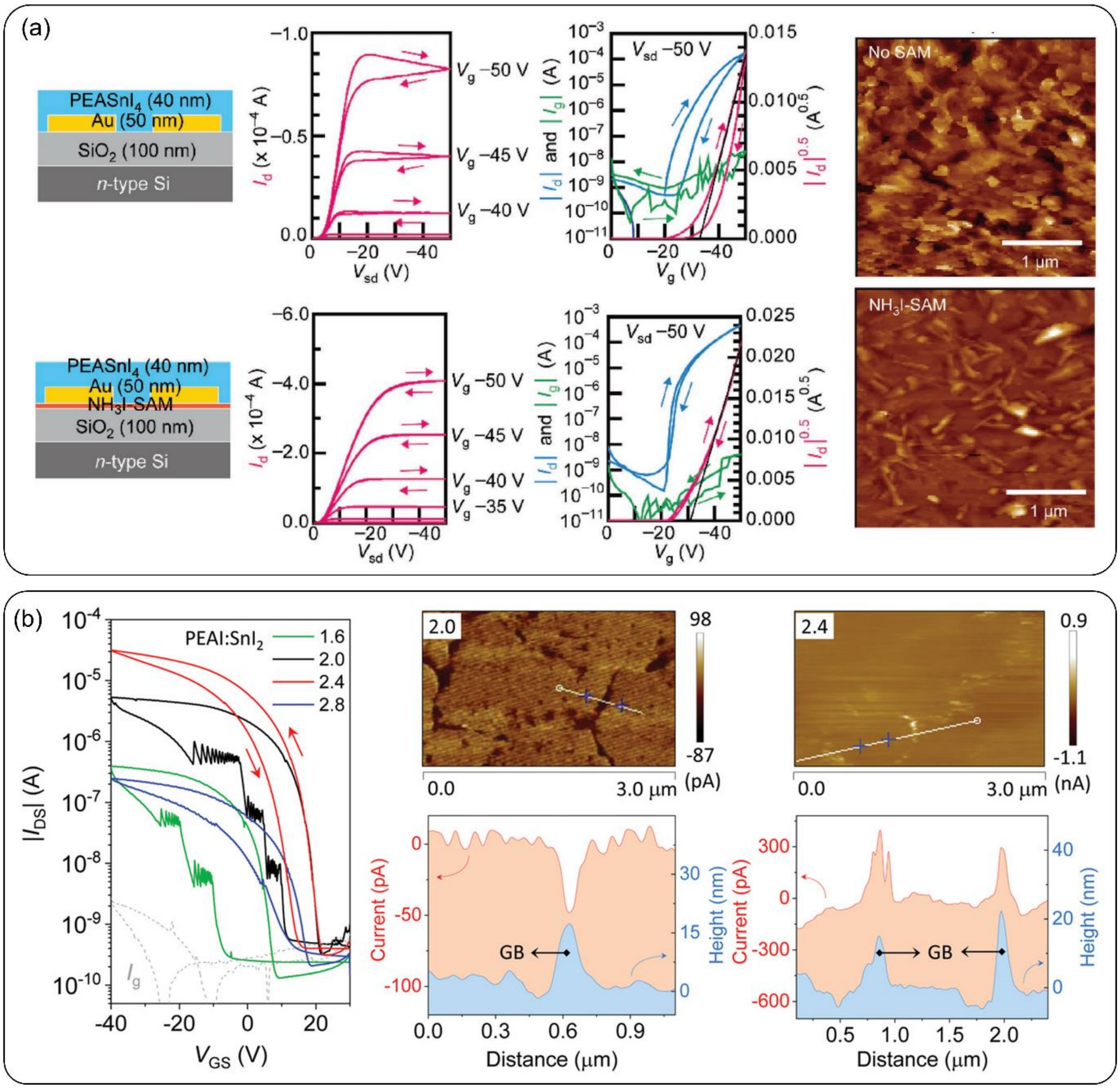

Figure 1.18. Representative output and transfer characteristics of the 2D perovskite transistors without and with NH_3I self-assembly monolayer, and the corresponding AFM images and XRD patterns of perovskite films.[81] (b) Transfer characteristics of 2D perovskite FETs obtained from precursors with different mole ratios PEAI:SnI_2 = X:1, X = 1.6, 2.0, 2.4, and 2.8, respectively ($V_{DS} = -40$ V); and conductive atomic force microscope images with line profiles of height and current.[95]

Considering that the components might be non-stoichiometric at grain boundaries, Zhu et al. controlled the molar ratio of two precursors PEAI and SnI_2 to be 1.6:1, 2.0:1, 2.4:1, and 2.8:1, respectively, and the corresponding device characteristics is shown in Figure 1.18b.[95] As evident, the FET characteristics were strongly influenced by the PEAI content. The mobility increased by a factor of 20 from 0.03 $cm^2V^{-1}s^{-1}$ at PEAI:SnI_2 molar ratio of 1.6:1 to 0.67

$cm^2V^{-1}s^{-1}$ at the ratio of 2.4:1, with notably enhanced $I_{ON/OFF}$ (≈10^5) and reduced dual-sweep hysteresis. The brighter contrast in the conductive atomic force microscopy (C-AFM) image indicates higher current flow through the perovskite layer. For the films with standard molar ratio of 2.0:1, the measured current was heterogeneous at the grain interior and grain boundary regions. Superimposing line profiles of the topography and current images spatially confirmed lower current through the grain boundaries. However, when PEAI:SnI_2 mole ratio increased to 2.4:1, the film current was markedly enhanced with improved overall homogeneity. This confirms that PEAI excess can passivate the grain boundaries effectively, facilitating charge carriers passing through the grain boundaries rather than being trapped.

1.7 Motivation

The recent emergence of metal halide perovskite semiconductors and successful achievement in the field of photovoltaics have motivated the exploration of their application in FETs. Nevertheless, a major limitation of 2D tin halide perovskites is the insulating nature of the bulky organic spacer cations, especially in single-layer structures, which show significantly reduced charge carrier mobility. To date, the understanding of the characteristics of 2D layered tin halide perovskites and exploration of their structure and properties, and the resultant FET performance are still at an early stage. A systematical investigation of the material properties and electrical parameters of 2D layered tin halide perovskite FETs is still missing. Understanding the correlation between the chemical structure of organic cations, grain size and charge carrier transport in 2D tin halide perovskite holds the key for the realization of high performance perovskite FETs.

1.7.1 Role of grain boundaries on charge carrier transport

So far, the 2D tin halide perovskite suffers from inferior film morphologies with small grain size and pinholes due to their fast crystallization process. Therefore, controlling crystal growth and reducing number of grain boundaries are crucial to achieve pronounced long-range molecular organization and high in-plane charge carrier transport in perovskites thin films. Grain engineering controlled by film deposition parameters is one of the new approaches to improve charge carrier transport. Such processing conditions, like substrate temperature, are usually not considered as a powerful tool to control surface morphology and microstructure of perovskite semiconductors.

In Chapter 2, I prepared 2D tin halide perovskite thin films by hot-casting method to fine tune the film morphologies. The correlation between grain size, charge transport properties, and ion migration was systematically studied to understand the role of grain boundaries in 2D tin halide perovskite FETs. It was found that despite a significant difference in grain size, however, the hot-casting method does not significantly affect the crystal lattice parameters and crystallinity. In contrast, the FET operation parameters, including mobility, threshold voltage, hysteresis, and subthreshold swing improve substantially with larger grain size. In addition, the dependence of the performance on channel lengths was further investigated. This Chapter provides an important insight into the grain engineering of 2D perovskites for high-performance FETs.

1.7.2 Influence of additive on tin oxidation

In Chapter 2, the role of grain boundaries in 2D layered tin halide perovskite FETs is clearly elucidated. However, the easy oxidation of Sn^{2+} in 2D tin halide perovskites is another intrinsic drawback, giving rise to high density of ionic defects and thus reducing the charge carrier transport in the channel, as described in Chapter 1.5.

In Chapter 3, I demonstrated a simple and effective additive engineering strategy by employing pentanoic acid (PA) to both modulate the crystallization process and improve charge carrier transport in 2D tin halide perovskite FETs. It was revealed that the additive is strongly coordinated to the spacer cation and inorganic framework in the perovskite precursor solution, effectively passivating defects by lowering undesired oxidation of Sn^{2+} during the film formation. The reduced defect density and decreased ion migration result in an enhanced p charge carrier mobility in FETs. These results illustrate that the additive strategy bears great potential to realize high-performance Sn-based perovskite FETs.

1.7.3 Chemical tuning of organic spacer cations

The above two Chapters helped me to have a better understanding of the crystallization process in solution-processed 2D tin halide perovskite thin films. Nevertheless, the ever-growing research field of FET devices research using 2D tin halide perovskites requires systematic understanding of the effects of the spacer cations on the crystal structure, charge carrier transport properties, and device performance. The chemical structure of organic cations is believed to strongly impact the optoelectronic properties of 2D halide perovskites and devices. However, most studies have chosen spacers randomly just like trial-and-error tests. The knowledge of the structural design rules of these organic cations, specifically the correlation between the chosen spacer and its impact on the properties of 2D perovskite film as well as the resulting device performance is far from being sufficient.

In Chapter 4, the FET structure was applied to investigate the charge carrier transport of 2D tin halide perovskite thin films with phenylalkylammonium molecules as organic cations varying alkyl chain lengths. For the first time, a strong change of the in-plane mobility in FET devices, depending on whether the number of carbon atoms on the alkyl side chain was an odd or even number was observed. Combining experimental characterization and theoretical calculation, I showed that a subtle change in the molecular structure of the organic cation has a significant impact on the molecular organization and phases as well as a surface morphology, which in turn will govern charge carrier transport in perovskite film FETs. This Chapter provides a general guideline and represents an important step toward molecular-level structural engineering in 2D tin halide perovskites to understand and control the electronic properties in FETs.

1.8 References

1. J. S. Manser, J. A. Christians and P. V. Kamat, *Chem. Rev.*, 2016, **116**, 12956.
2. L. M. Herz, *Annu. Rev. Phys. Chem.*, 2016, **67**, 65.
3. S. D. Stranks and H. J. Snaith, *Nat. Nanotechnol.*, 2015, **10**, 391.
4. Y. H. Kim, H. Cho and T. W. Lee, *PNAS*, 2016, **113**, 11694.
5. C. Y. Yi, J. S. Luo, S. Meloni, A. Boziki, N. Ashari-Astani, C. Grätzel, S. M. Zakeeruddin, U. Röthlisberger and M. Grätzel, *Energy Environ. Sci.*, 2016, **9**, 656-662.
6. J. Y. Qian, B. Xu and W. J. Tian, *Org. Electron.*, 2016, **37**, 61.
7. Y. Y. Dang, D. X. Ju, L. Wang and X. T. Tao, *Crystengcomm*, 2016, **18**, 4476.
8. J. R. Li and P. Rinke, *Phys. Rev. B*, 2016, **94**, 045201.
9. T. J. Jacobsson, M. Pazoki, A. Hagfeldt and T. Edvinsson, *J. Phys. Chem.*, 2015, **119**, 25673.
10. G. Kieslich, S. J. Sun and A. K. Cheetham, *Chem. Sci.*, 2015, **6**, 3430.
11. Z. Li, M. J. Yang, J. S. Park, S. H. Wei, J. J. Berry and K. Zhu, *Chem. Mater.*, 2016, **28**, 284.
12. C. Shi, C. H. Yu and W. Zhang, *Angew. Chem.*, 2016, **128**, 5892.
13. C. P. Fu, Z. K. Gu, Y. Tang, Q. Xiao, S. S. Zhang, Y. Q. Zhang and Y. L. Song, *Angew. Chem.*, 2022, **134**, 202117067.
14. G. Nasti and A. Abate, *Adv. Energy Mater*, 2020, **10**, 1902467.
15. Y. P. Fu, , M. P. Hautzinger, Z. Y. Luo, F. F. Wang, D. X. Pan, , M. M. Aristov, I. A. Guzei, A. L. Pan, X. Y. Zhu and S. Jin, *ACS Cent. Sci.*, 2019, **5**, 1377.
16. S. Ramos-Terrón, A. D. Jodlowski, C. Verdugo-Escamilla, L. Camacho and G. Miguel, *Chem. Mater.*, 2020, **32**, 4024.
17. H. Y. Ma, C. Q. Leng, Y. X. Ji, X. Z. Wei, K. Sun, L. L. Tang, J. Yang, W. Luo, C. L. Li, Y. S. Deng, S. L. Feng, J. Shen, S. R. Lu, C. L. Du and H. F. Shi, *Nanoscale*, 2016, **8**, 18309.
18. S. Kumar, J. Jagielski, S. Yakunin, P. Rice, Y. C. Chiu, M. C. Wang, G. Nedelcu, Y. G. Kim, S. C. Lin, E. J. G. Santos, M. V. Kovalenko and C. J. Shih, *ACS Nano*, 2016, **10**, 9720.
19. M. Saliba, S. M. Wood, J. B. Patel, P. K. Nayak, J. Huang, J. A. Alexander-Webber, B.

Wenger, S. D. Stranks, M. T. Hörantner, J. T. W. Wang, R. J. Nicholas, L. M. Herz, M. B. Johnston, S. M. Morris, H. J. Snaith and M. K. Riede, *Adv. Mater.*, 2016, **28**, 923.

20. M. I. Saidaminov, V. Adinolfi, R. Comin, A. L. Abdelhady, W. Peng, I. Dursun, M. J. Yuan, S. Hoogland, E. H. Sargent and O. M. Bakr, *Nat. Commun.*, 2015, **6**, 1.
21. M. D. Birowosuto, D. Cortecchia, W. Drozdowski, K. Brylew, W. Lachmanski, A. Bruno and C. Soci, *Sci. Rep.*, 2016, **6**, 1.
22. C. H. Chen, Z. C. Li, Q. F. Xue, Y. A. Su, C. C. Lee, H. L. Yip, W.C. Chen and C. C. Chueh, *Org. Electron.*, 2019, **75**, 105400.
23. P. P. Mohanty, R. Ahuja and S. Chakraborty, *Nanotechnology,* 2022, **33**, 292501.
24. X. Huang, W. T. Bi, P. C. Jia, Y. Tang, Z. D. Lou, Y. F. Hu, Q. H. Cui, Y. B. Hou and F. Teng, *Org. Electron.*, 2019, **67**, 101.
25. Q. Cheng, B. X. Wang, G. S. Huang, Y. X. Li, X. Li, J. Y. Chen, S. L. Yue, K. Li, H. Zhang, Y. Zhang and H. Q. Zhou, *Angew. Chem.*, 2022, **61**, 202208264.
26. J. Wang, Y. Mi, X. Gao, J. Z. Li, J. Z. Li, S. G. Lan, C. Fang, H. Z. Shen, X. L. Wen, R. Chen, X. F. Liu, T. C. He and D. H. Li, *Adv. Opt. Mater.*, 2019, **7**, 1900398.
27. A. Kumar, S. Singh, M. K. A. Mohammed and A. E. Shalan, *Sol. Energy,* 2021, **223**, 193.
28. D. Ghosh, D. Acharya, L. Pedesseau, C. Katan, J. Even, S. Tretiak and A. J. Neukirch, *J. Mater. Chem. A,* 2020, **8**, 22009.
29. H. J. Yang, J. Tang, L. L. Deng, Z. Liu, X. Yang, Z. Q. Huang, H. M. Yu, K. Wang and J. P. Li, *Phys. Chem. Chem. Phys.,* 2022, **24**, 7969.
30. D. Y. Fu, J. R. Yuan, S. C. Wu, Y. P. Yao, X. Y. Zhang and X. M. Zhang, *Inorg. Chem. Front.,* 2020, **7**, 1394.
31. M. Azeem, Y. Qin, Z. G. Li and W. Li, *Mater. Chem. Front.*, 2021, **5**, 7587.
32. R. Chakraborty and A. Nag, *J. Phys. Chem. C.*, 2020, **124**, 16177.
33. X. X. Liu, T. J. Huang, L. Y. Zhang, B. S. Tang, N. D. Zhang, D. W. Shi and H. Gong, *Eur. J. Chem.*, 2018, **24**, 4991.
34. B. Y. Kim and S. I. Seok, *Energy Environ. Sci.*, 2020, **13**, 805.
35. L. Zhu, D. W. Liu, J. P. Wang and N. N. Wang, *J. Phys. Chem. Lett.*, 2020, **11**, 8502.
36. C. Q. Jing, J. Wang, H. F. Zhao, W. X. Chu, Y. Yuan, Z. Wang, M. F. Han, T. Xu, J. Q. Zhao and X. W. Lei. *Eur. J. Chem.*, 2020, **26**, 10307.

37. B. P. Darwich, N. Guijarro, H. H. Cho, L. Yao, L. Monnier, P. Schouwink, M. Mensi, H. Yum and K. Sivula, *ChemSusChem*, 2021, **14**, 3001.

38. A. Dučinskas, G. C. Fish, M. A. Hope, L. Merten, D. Moia, A. Hinderhofer, L. C. Carbone, J. E. Moser, F. Schreiber, J. Maier, J. V. Milić and M. Grätzel, *J. Phys. Chem. Lett.*, 2021, **12**, 10325.

39. D. M. Zheng and T. Pauporté, *J. Mater. Chem. A.*, 2021, **9**, 17801.

40. Y. Vaynzof, *Adv. Energy Mater,* 2020, **10**, 2003073.

41. N. J. Jeon, J. H. Noh, Y. C. Kim, W. S. Yang, S. Ryu and S. I. Seok, *Nat. Mater.*, 2014, **13**, 897.

42. Z. Li, T. R. Klein, D. H. Kim, M. Yang, J. J. Berry, M. F. V. Hest and K. Zhu, *Nat. Rev. Mater.*, 2018, **3**, 1.

43. M.Konstantakou, D. Perganti, P. Falaras and T. Stergiopoulos, *Crystals*, 2017, **7**, 291.

44. G. Cotella, J. Baker, D. Worsley, F. D. Rossi, C. Pleydell-Pearce, M. Carnie and T. Watson, *Sol. Energy Mater. Sol. Cells.*, 2017, **159**, 362.

45. C. L. Ellis, E. Smith, H. Javaid, G. Berns and D. Venkataraman, *Perovskite Photovoltaics*, 2018, **163**. Academic Press.

46. W. J. Chen, Z. X. Gan, M. A. Green, B. H. Jia and X. M. Wen, *Small Methods*, 2021, **5**, 2000731.

47. J. Liu, J. Y. Jin, Z. Yang, J. Z. Cai, J. Y. Yue, J. Impundu, H. Liu, H. N. Wei, Z. S. Peng, Y. J. Li and L. F. Sun, *ACS Appl. Mater. Interfaces,* 2020, **12**, 31776.

48. Y. X. Zhang, Y. C. Liu, Z. Xu, Z. Yang and S. Z. Liu, *Small*, 2020, **16**, 2003145.

49. C. C. Gao, Y. Z. Jiang, C. J. Sun, J. R. Han, T. W. He, Y. M. Huang, K. L. Yao, M. Han, X. Wang, Y. K. Wang, Y. N. Gao, Y. C. Liu, M. J. Yuan and H. Y. Liang, *ACS Photonics*, 2020, **7**, 1915.

50. G. B. Wu, R. Liang, Z. P. Zhang, M. Z. Ge, G. C. Xing and G. X. Sun, *Small*, 2021, **17**, 2103514.

51. J. Cho, J. T. DuBose, A. N. T. Le and P. V. Kamat, *ACS Mater. Lett.*, 2020, **2**, 565.

52. J. Siekmann, S. Ravishankar and T. Kirchartz, *ACS Energy Lett.*, 2021, **6**, 3244.

53. Y. B. Yuan and J. S. Huang, *Acc. Chem. Res.*, 2016, **49**, 286.

54. Y. Yuan, J. Chae, Y. Shao, Q. Wang, Z. Xiao, A. Centrone and J. S. Huang, *Adv. Energy*

Mater, 2015, **5**, 1500615.

55. J. G. Labram, , D. H. Fabini, , E. E. Perry, , A. J. Lehner, , H. B. Wang, , A. M. Glaudell, G. W, H. Evans, D. Buck, R. Cotta, L. Echegoyen, F. Wudl, R. Seshadri and M. L. Chabinyc, *J. Phys. Chem. Lett.*, 2015, **6**, 3565.
56. J. Xing, Q.Wang, Q. F. Dong, Y. B. Yuan, Y. J. Fang and J. S. Huang, *Phys. Chem. Chem. Phys.*, 2016, **18**, 30484.
57. D. H. Li, H. Wu, H. C. Cheng, G. M. Wang, Y. Huang and X. F. Duan, *ACS Nano*, 2016, **10**, 6933.
58. C. Eames, J. M. Frost, P. R. F. Barnes, B. C. O'Regan, A. Walsh and M. S. Islam, *Nat. Commun.*, 2015, **6**, 7497.
59. Y. H. Ma, Y. H. Cheng, X. W. Xu, M. L. Li, C. J. Zhang, S. H. Cheung, Z. X. Zeng, D. Shen, Y. M. Xie, K. L. Chiu, F. Lin, S. K. So, C. S. Lee and S. W. Tsang, *Adv. Funct. Mater*, 2021, **31**, 2006802.
60. D. Q. Mei, L. L. Qiu, L. Chen, F. Q. Xie, L. X. Song, J. Q. Wang, P. F. Du and J. Xiong, *Thin Solid Films*, 2022, **752**, 139196.
61. M. T. Mbumba, D. M. Malouangou, J. M. Tsiba, M. W. Akram, L. Y. Bai, Y., F. Yang and M. Guli, *J. Mater. Chem. C*, 2021, **9**, 14047.
62. E. B. Bi, Z. N. Song, C. W. Li, Z. F. Wu and Y. F. Yan, *Trends Chem.*, 2021, **3**, 575.
63. P. Huang, S. Kazim, M. K. Wang and S. Ahmad, *ACS Energy Lett.*, 2019, **4**, 2960.
64. L. C. Zhao, P. Y. Tang, D. Y. Luo, M. I. Dar, F. T. Eickemeyer, N. Arora, Q. Hu, J. S. Luo, Y. H. Liu, S. M. Zakeeruddin, A. Hagfeldt, J. Arbiol, W. Huang, Q. H. Gong, T. P. Russell, R. H. Friend, M. Grätzel and R. Zhu, *Sci. Adv.*, 2022, **8**, 3733.
65. F. Jahanbakhshi, M. Mladenović, E. Kneschaurek, L. Merten, M. C. Gélvez-Rueda, P. Ahlawat, Y. Li, A. Dučinskas, A. Hinderhofer, M. I. Dar, W. Tress, B. Carlsen, A. Ummadisingu, S. M. Zakeeruddin, A. Hagfeldt, F. Schreiber, F. C. Grozema, U. Rothlisberger, J. V. Milić and M. Graetzel, *J. Mater. Chem. A*, 2020, **8**, 17732.
66. C. J. Tong, X. Cai, A. Y. Zhu, L. M. Liu and O. V. Prezhdo, *J. Am. Chem. Soc.*, 2022, **144**, 6604.
67. A. F. Castro-Méndez, J. Hidalgo and J. P. Correa-Baena, *Adv. Energy Mater*, 2019, **9**, 1901489.

68. W. L. Yao, S. Y. Fang, Z. Y. Hu, L. K. Huang, X. H. Liu, H. C. Zhang, J. Zhang and Y. J. Zhu, *Small*, 2022, **18**, 2105140.
69. H. Y. Jiao, , Z. Y. Ni, Z. F. Shi, , C. B. Fei, Y. Liu, , X. Z. Dai and J. S. Huang, *Sci. Adv.*, 2022, **8**, 4524.
70. K. Liu, B. Ouyang, X. J. Guo, Y. L. Guo and Y. Q. Liu, *npj Flexible Electron.*, 2022. **6**, 1.
71. D. Hong, G. Yerubandi, H. Q. Chiang, M. C. Spiegelberg and J. F. Wager, *Critical Reviews in Solid State and Materials Sciences*, 2008, **33**, 101.
72. M. J. Deen, O. Marinov, U. Zschieschang and H. Klauk, *IEEE Trans. Electron Devices*, 2009, **56**, 2962.
73. M. C. Hamilton, S. Martin and J. Kanicki, *Chem. Mater.*, 2004, **16**, 4699.
74. C. R. Kagan, D. B. Mitzi and C. D. Dimitrakopoulos, *Science*, 1999, **286**, 945.
75. X. H. Liu, D. J. Yu, X. F. Song and H. B. Zeng, *Small*, 2018, **14**, 1801460.
76. L. S. Liang and P. Gao, *Adv. Sci.*, 2018, **5**, 1700331.
77. D. H. Fabini, G. Laurita, J. S. Bechtel, C. C. Stoumpos, H. A. Evans, A. G. Kontos, Y. S. Raptis, P. Falaras, A. V. D. Ven, M. G. Kanatzidis and R. Seshadri, *J. Am. Chem. Soc.*, 2016, **138**, 11820.
78. C. Q. Qin, F. Zhang, L. Qin, X. Liu, H. Y. Ji, L. T. Li, Y. F. Hu, Z. D. Lou, Y. B. Hou and F. Teng, *Adv. Electron. Mater.*, 2021, **7**, 2100384.
79. P. Parkinson, C. Dodson, H. J. Joyce, K. A. Bertness, N. A. Sanford, L. M. Herz and M. B. Johnston, *Nano Lett.*, 2012, **12**, 4600.
80. D. B. Mitzi, C. D. Dimitrakopoulos and L. L. Kosbar, *Chem. Mater.*, 2001, **13**, 3728.
81. T. Matsushima, S. Hwang, A. S. Sandanayaka, C. Qin, S. Terakawa, T. Fujihara, M. Yahiro and C. Adachi, *Adv. Mater.*, 2016, **28**, 10275.
82. T. Matsushima, M. R. Leyden, T. Fujihara, C. Qin, A. S. Sandanayaka and C. Adachi, *Appl. Phys. Lett.*, 2019, **115**, 120601.
83. T. Matsushima, F. Mathevet, B. Heinrich, S. Terakawa, T. Fujihara, C. Qin, A. S. D. Sandanayaka, J. C. Ribierre and C. Adachi, *Appl. Phys. Lett.*, 2016, **109**, 253301.
84. F. Paulus, C. Tyznik, O. D. Jurchescu and Y. Vaynzof, *Adv. Funct. Mater.*, 2021, **31**, 2101029.

85. C. J. Tong, L. Li, L. M. Liu and O. V. Prezhdo, *J. Am. Chem. Soc.*, 2020, **142**, 3060.

86. P. Calado, A. M. Telford, D. Bryant, X. Li, J. Nelson, B. C. O'Regan and P. R. Barnes, *Nat. Commun.*, 2016, **7**, 13831.

87. S. P. Senanayak, B. Yang, T. H. Thomas, N. Giesbrecht, W. Huang, E. Gann, B. Nair, K. Goedel, S. Guha, X. Moya, C. R. McNeill, P. Docampo, A. Sadhanala, R. H. Friend and H. Sirringhaus, *Sci. Adv.*, 2017, **3**, 1601935.

88. F. J. Liu, L. Wang, J. W. Wang, F. Wang, Y. Y. Chen, S. Zhang, H. J. Sun, J. Liu, G. T. Wang, Y. Y. Hu and C. Jiang, *Adv. Funct. Mater.*, 2020, **31**, 2005662.

89. J. Wang, H. Z. Shen, W. C. Li, S. Wang, J. Z. Li and D. H. Li. *Adv. Sci.*, 2019, **6**, 1802019.

90. I. You and Y. Y. Noh, *Appl. Phys. Lett.*, 2021, **118**, 250501.

91. R. X. Lin, K. Xiao, Z. Y. Qin, Q. L. Han, C. F. Zhang, M. Y. Wei, M. I. Saidaminov, Y. Gao, J. Xu, M. Xiao, A. D. Li, J. Zhu, E. H. Sargent and H. R. Tan, *Nat. Energy*, 2019, **4**, 864.

92. T. Leijtens, R. Prasanna, A. Gold-Parker, M. F. Toney and M. D. McGehee, *ACS Energy Lett.*, 2017, **2**, 2159.

93. M. I. Saidaminov, I. Spanopoulos, J. Abed, W. Ke, J. Wicks, M. G. Kanatzidis and E. H. Sargent, *ACS Energy Lett.*, 2020, **5**, 1153.

94. E. J. Yeom, S. S. Shin, W. S. Yang, S. J. Lee, W. P. Yin, D. Kim, J. H. Noh, T. K. Ahn and S. I. Seok, *J. Mater. Chem. A*, 2017, **5**, 79.

95. H. H. Zhu, A. Liu, K. I. Shim, J. Hong, J. W. Han and Y. Y. Noh, *Adv. Mater.*, 2020, **32**, 2002717.

96. H. H. Zhu, A. Liu, H. Kim, J. Hong, J. Y. Go and Y. Y. Noh, *Chem. Mater.*, 2020, **33**, 1174.

97. Y.Gao, Z. T. Wei, P. Yoo, E. Z. Shi, M. Zeller, C. H. Zhu, P. L. Liao and L. T. Dou, *J. Am. Chem. Soc.*, 2019, **141**, 15577.

98. Z. T. Wei, K. Wang, W. C. Zhao, Y. Gao, Q. X. Hu, K. Chen and L. T. Dou, *Chem. Commun.*, 2021, **57**, 11469.

99. A. H. Liang, Y. Gao, R. Asadpour, Z. T. Wei, B. P. Finkenauer, L. R. Jin, J. Q. Yang, K. Wang, K. Chen, P. L. Liao, C. H. Zhu, L. B. Huang, B. W. Boudouris, M. A. Alam and L. T. Dou, *J. Am. Chem. Soc.*, 2021, **143**, 15215.

100. J. Euvrard, Y. Yan and D. B. Mitzi, *Nat. Rev. Mater.*, 2021, **6**, 531.
101. Y. J. Reo, H. H. Zhu, J. Y. Go, K. I. Shim, A. Liu, T. Y. Zou, H. Jung, H. J. Kim, J. S. Hong, J. W. Han and Y. Y. Noh, *Chem. Mater.*, 2021, **33**, 2498.
102. J. Y. Go, H. H. Zhu, Y. Reo, H. Kim, A. Liu and Y. Y. Noh, *ACS Appl. Mater. Interfaces*, 2022, **14**, 9363.
103. Y. Liu, P. A. Chen, X. X. Qiu, J. Guo, J. N. Xia, H. Wei, H. H. Xie, S. J. Hou, M. He, X. Wang, Z. B. Zeng, L. Jiang, L. Liao and Y. Y. Hu, *iScience*, 2022, **25**, 104109.

Chapter 2 Grain engineering of 2-thiopheneethylammonium tin iodide perovskite by hot-casting

2.1 Introduction

So far, several strategies have been proposed to enhance the device performance of 2D tin halide perovskite FETs including controlling the crystallization process, regulating the film microstructure and adjusting the phase orientation. These approaches involve self-assembled monolayer, non-stoichiometry engineering, mixed solvent, and additives.[1,2] FETs may also benefit from the perovskite layers parallel oriented to substrate, which should substantively reduce charge-transport resistance in in-plane direction and dramatically improve the device performance.[3] However, a simple, robust and general approach to effectively control the crystal orientation in layered 2D perovskites for FET applications is still lacking. Increasing grain size is another important strategy to improve the FET performance. The growth of large grains decreases charge transport barriers and structural defects that both increase the efficiency of perovskite solar cells have been reported.[4] Recently, high mobility 2D tin-based perovskite FETs were realized by employing π-conjugated bulky cations and optimized annealing temperatures to reach large grain sizes up to 500 µm.[5] However, the complicated synthesis of large cations might impede their potential application. For this reason, small and simple cations bear high potential for 2D perovskite FETs.

The precursor compounds and solution deposition have a strong impact on the charge carrier properties of perovskites. Thiophene derivatives have been widely used as organic semiconductors as well as spacers and passivators in perovskite optoelectronic devices, resulting in high device performances.[6,7] Chiu et al. performed theoretical simulations and found that the reduced dielectric constant of 2-thiopheneethylammonium (TEA) as compared to benchmark organic cation PEA in 2D tin perovskite, leads to the narrower band gaps and improved dielectric confinement, making TEA suitable for efficient optoelectronic device applications.[8] This gives me the motivation to selected the TEA organic spacer for the studies on the correlation between grain size and FET performance.

In this Chapter, rational grain engineering by the hot-casting method was applied for 2D tin halide perovskite thin films to drastically reduce the ion migration that limits the device performance of FETs. It showed that hot-casting is an efficient approach to precisely control the crystallization and growth kinetics of 2-thiopheneethylammonium tin iodide ($(TEA)_2SnI_4$), enabling large grain sizes. While the local charge carrier mobility improved moderately with larger grain size, the performance of the perovskite FETs was increased considerably due to a reduced density of grain boundaries that lower the charge trapping and ion migration. The insights on the role of grain boundaries on charge carrier transport and ion migration of $(TEA)_2SnI_4$ are important for the development of high-performance 2D perovskite-based FET devices.

2.2 DFT calculation

The density functional theory (DFT) calculation was firstly carried out by Dr. Mukunda Mandal and Dr. Denis Andrienko to decipher the effect of incorporating the thiophene-based TEA ligand as the organic spacer within the octahedral $[SnI_6]^{4-}$ sheets on the overall electronic properties of the 2D perovskite semiconductor. Figure 2.1a shows the molecular structures of organic cation TEA (synthesized by Sabine Frisch and Prof. Dr. Milan Kivala). The calculated lattice parameters for $(TEA)_2SnI_4$ reveal a distance 31.5 Å for adjacent double interlayers along the c-axis direction, as shown in Figure 2.1b. The band structure of $(TEA)_2SnI_4$ (Figure 2.1c) suggests a direct bandgap of 1.25 eV at the PBE at Γ-point. The density of states plot in Figure 2.1d indicates that both the valence band maximum (VBM) at 1.80 eV and the conduction band minimum (CBM) at 3.05 eV are mainly located at the inorganic layers. Specifically, the Sn 5s and I 5p orbitals contribute to the VBM, while the CBM is primarily composed of the Sn 5p orbital. The effective masses of electron (m_e^*) and hole

(m_h*), in units of the rest mass of the free electron (m_0), were also calculated from the band structure in Figure 2.1d using parabolic fitting of the band edges. Based on the DFT calculations, the computed m_h* and m_e* value of 0.137 m_0 and 0.146 m_0 (with m_0 as the electron rest *mass*) was used for the calculation of the hole mobility in the subsequent THz analysis.[9]

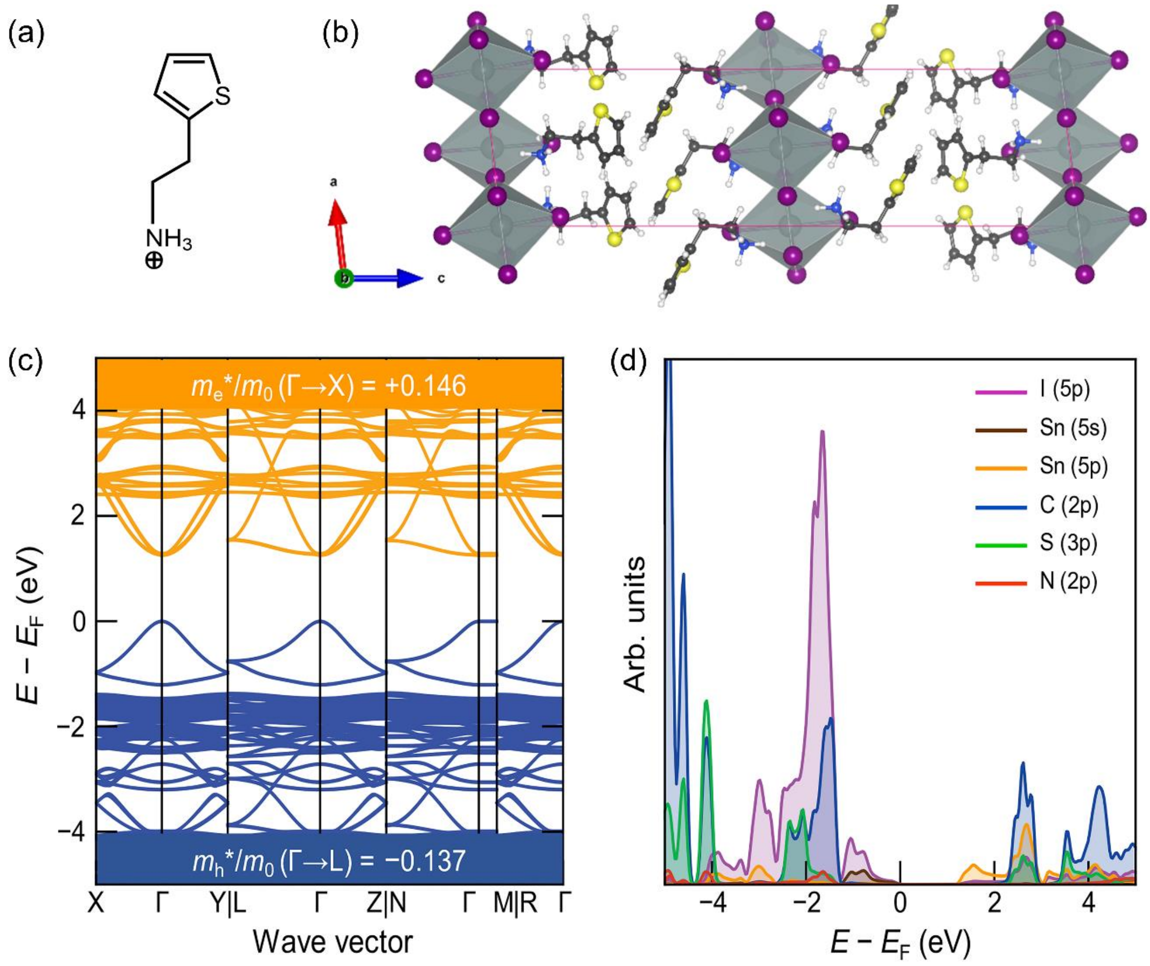

Figure 2.1. (a) Chemical structure of organic cation TEA; (b) PBE-D3(0)-optimized structure and lattice parameters for $(TEA)_2SnI_4$. (c) Band structure and (d) density of states (DOS) of $(TEA)_2SnI_4$ from DFT calculations. The total DOS is not shown in (d) for clarity. Effective mass of electron (m_e*) and hole (m_h*) are reported in the units of the free electron rest mass ($m_0 = 9.11 \times 10^{-31}$ kg).

2.3 Hot-casting of $(TEA)_2SnI_4$

Similar to organic semiconductors, the thin-film morphology is a critical factor for efficient and stable charge transport in perovskite FETs.[10] To correlate the morphology formation and crystallization kinetics of $(TEA)_2SnI_4$ with the behavior of FETs, hot-casting was applied to tune the grain size of the thin films. Figure 2.2 schematically describes the hot-casting process for deposition of $(TEA)_2SnI_4$ thin films. In contrast to the procedure reported in literature, the approach involves spin-coating a mixture of organic cation TEA and tin iodide (SnI_2) solution onto a hot substrate maintained at a temperature range from room-temperature (RT) to 160 °C to obtain a uniform film. This process was modified to the reported method to ensure continuity (pinhole-free structure) and homogeneity of the obtained film and to control the lateral grain size and film roughness which finally determine the charge carrier transport in $(TEA)_2SnI_4$ FETs.

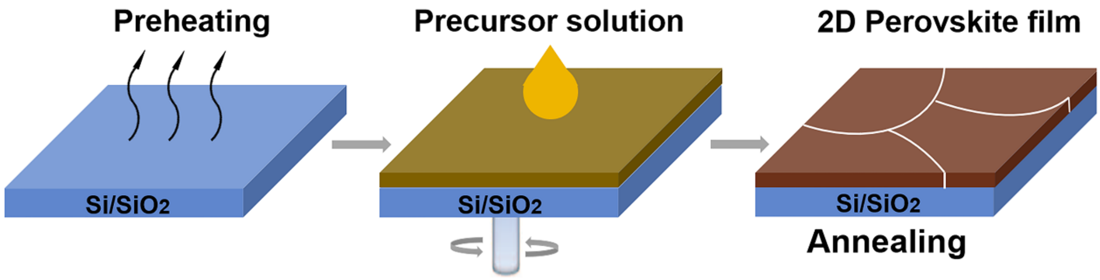

Figure 2.2. Schematic diagram of the hot-casting process of 2D $(TEA)_2SnI_4$ perovskite thin film.

2.4 Thin film characterization

2.4.1 Film morphology

Atomic force microscopy (AFM) was used to evaluate the role of substrate temperature on the $(TEA)_2SnI_4$ film morphology deposited on Si/SiO_2 substrate. Figure 2.3a-f illustrate grain structures obtained at different substrate temperatures from RT to 160°C. As evident from the AFM image, $(TEA)_2SnI_4$ deposited at RT creates 2 μm small grains surrounded by pinholes. The grain size is substantially enlarged when the substrate temperature is increased to 120 °C resulting in a more compact and uniform surface morphology. Histograms of the grain size distribution in Figure 2.3g reveal that with increasing temperature from RT to 120 °C the grain size increases from 2 μm to 9 μm, while further temperature rise leads to its reduction.

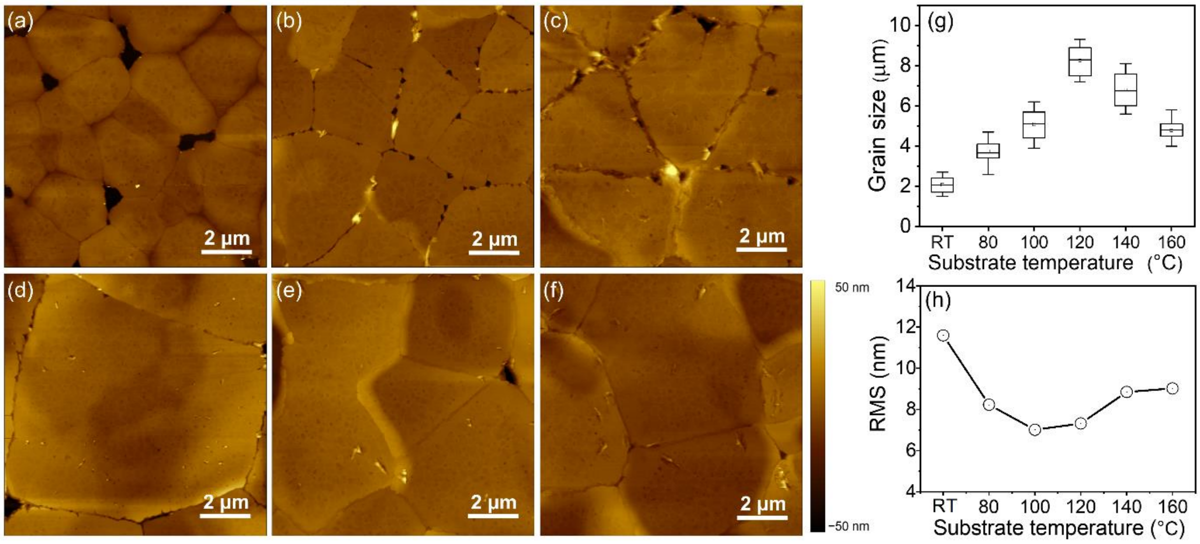

Figure 2.3. AFM height images of thin $(TEA)_2SnI_4$ films processed at the substrate temperature of (a) RT, (b) 80 °C, (c) 100 °C, (d) 120 °C, (e) 140 °C and (f) 160 °C. (g) Grain size and (h) film root mean square roughness as a function of substrate temperature.

Optical microscopy images further confirm larger grains in the hot casted films compared to RT cast ones (Figure 2.4). The optimal growth conditions for large grains at 120 °C can be attributed to a low number of nucleation sites allowing a prolonged growth of the $(TEA)_2SnI_4$ crystals. As the substrate temperature further increases, a larger number of nuclei precipitate from the supersaturation solution due to the fast solvent vaporization, yielding smaller crystal grains.[11] Increasing the grain size is of great importance for perovskite FETs because the grain boundaries act as trap centers for charge carriers and pathways for ion migration, which is one of the key reasons for the limited device performance perovskites.[12] In that case, the presence of grain boundaries generates a potential barrier for carrier transport across the active channel of the FET. Large grains together with a low density of boundaries minimize the concentration of mobile ions leading to efficient charge carrier transport and stable device performance. In addition, the film root mean square roughness (RMS) is reduced when hot-casting is applied (Figure 2.3h). The $(TEA)_2SnI_4$ films processed at 100 °C and 120 °C show the smoothest film surface with low RMS values of 7.04 and 7.26 nm. The flattened surface is beneficial to reduce the roughness-induced charge scattering effects and to improve the effective contact between the perovskite semiconducting film and electrodes.[13]

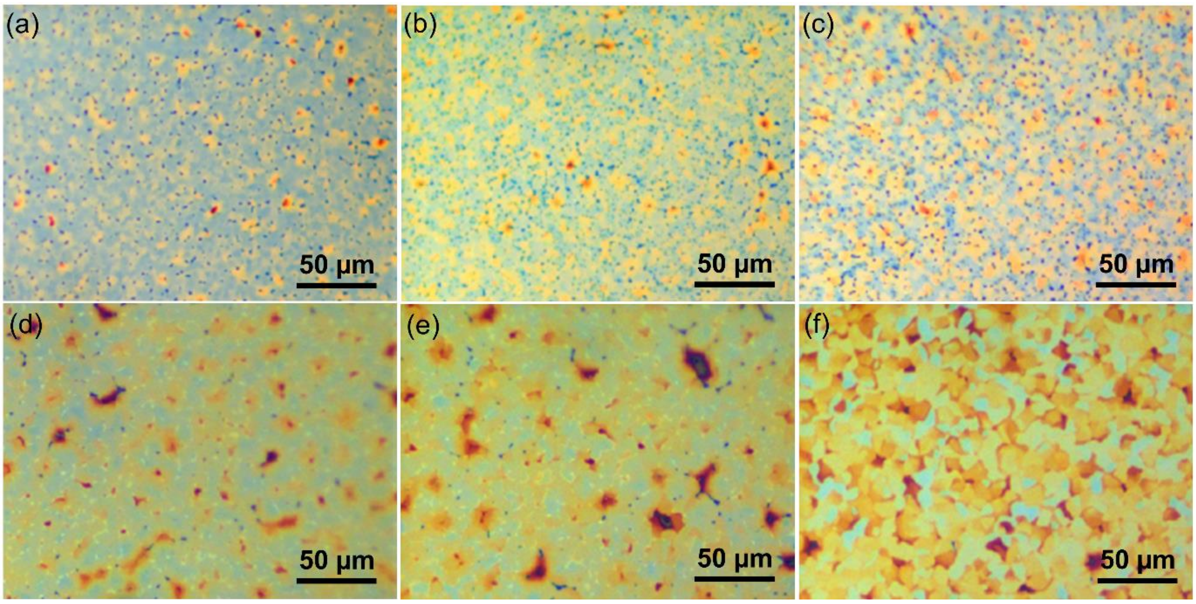

Figure 2.4. Optical microscope images for 2D $(TEA)_2SnI_4$ perovskite thin films cast at substrate temperature of (a) RT, (b) 80 °C, (c) 100 °C, (d) 120 °C, (e) 140 °C and (f) 160 °C, respectively.

2.4.2 Crystal structure and molecular organization

The optical properties of $(TEA)_2SnI_4$ thin films with traditional spin-coating at RT were investigated by ultraviolet-visible (UV-vis) absorption and steady-state photoluminescence (PL) measurements as shown in Figure 2.5a, which confirm the formation of the target layered perovskite structure.[14] The absorption peak located at 440 nm (corresponding to 2.82 eV) is attributed to the high-energy exciton transition energy levels. The absorption peak located at 529 nm (2.34 eV) is assigned to the charge transfer from TEA^+ organic cations to adjacent $[SnI_4]^{2-}$ octahedron layers, whereas the sharp absorption centered at 619 nm (2.00 eV) is attributed to the intrinsic exciton absorption of the tin iodide lattice.[15] The $(TEA)_2SnI_4$ exhibited strong photoluminescence at room temperature with the corresponding PL peak located at 649 nm (1.91 eV).

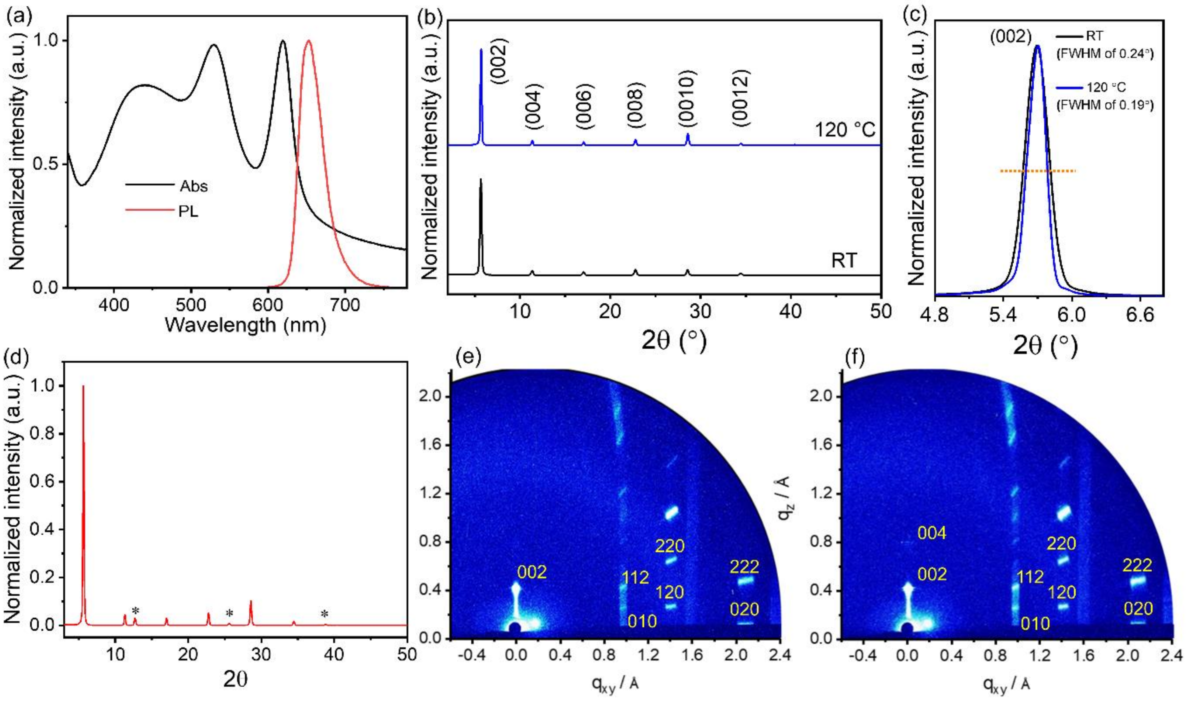

Figure 2.5. (a) UV-vis absorption and PL spectra of (TEA)$_2$SnI$_4$ thin film. (b) Out-of-plane XRD measured for (TEA)$_2$SnI$_4$ thin films cast at RT and 120 °C. (c) FWHM analysis of the (002) peak. (d) XRD pattern of the (TEA)$_2$SnI$_4$ thin film prepared with hot-casting method at 140 °C. GIWAXS patterns for (TEA)$_2$SnI$_4$ cast at (e) RT and (f) 120 °C (reflections are assigned by Miller indices).

The role of deposition temperature on the crystal structure of the 2D (TEA)$_2$SnI$_4$ thin films was further investigated by X-ray diffraction (XRD) and grazing incidence wide-angle X-ray scattering (GIWAXS). The substrate temperature of 120 °C was chosen as optimal condition due to the largest grain size in the film. The XRD patterns of the two films cast at RT and 120 °C in Figure 2.5b exhibit typical (00l) diffractions (l = 2, 4, 6, 8,10, and 12), confirming a layered and well-ordered structure of the (TEA)$_2$SnI$_4$ films. The interlayer spacing of 15.6 Å is consistent with the DFT calculations in Figure 2.2a. The diffraction peak intensity is only slightly higher for the optimized film processed at 120 °C compared to the RT deposited one. The full width at half-maximum (FWHM) of the (002) diffraction peak slightly differs and decreases from 0.24° for RT to 0.19° for the substrate temperature of 120 °C (Figure 2.5c). The slightly changed diffraction intensity and FWHM value indicate a similar out-of-plane crystallinity for the (TEA)$_2$SnI$_4$ films cast at RT and 120 °C. For films cast at 140 °C, additional peaks appear in the XRD spectra, as shown in Figure 2.5d, which are assigned to SnI_2. This suggests that the film fabricated at temperatures beyond 140 °C does not fully convert from the source compounds to the complete semiconducting perovskite phase which is also detrimental for the crystallinity and device operation.

Figure 2.5e and f shows the GIWAXS patterns of the thin films processed at RT and 120 °C (performed by Okan Yildiz). The diffraction peak with the highest intensity is assigned to the interlayer spacing (002). The in-plane (010) and (020) reflections are attributed to *Sn-I* and *I-Sn-I* bonds with corresponding *d*-spacing values of 2.9 Å and 5.8 Å, in agreement with literature.[16] The octahedral structure of the $[SnI_4]^{2-}$ sheet exhibits the 120 peak (4.1 Å) for I-I bonds. The inorganic part $[SnI_4]^{2-}$ is organized parallel to the substrate surface, which is beneficial for the in-plane charge transport of FETs. To understand the influence of the substrate temperature on the crystallite size, the coherence length (CL) is calculated for the (010) and (020) reflections. Interestingly, the films processed at RT and 120 °C reveal identical CL_{010} and CL_{020} values of ~132 nm and ~19 nm, respectively. Despite a significant difference in grain size, surprisingly, the substrate temperature does not significantly affect the crystal lattice parameters and crystallinity.

2.4.3 Optical-pump THz-probe spectroscopy

To investigate how deposition temperature and thus film morphology affect the local charge carrier transport in $(TEA)_2SnI_4$ perovskites, the contact-free, optical pump-Terahertz (THz) probe (OPTP) spectroscopy was conducted by Heng Zhang and Dr. Hai I. Wang. Unlike the FET devices, where the charge carriers are transported over the macroscopic dimension of the transistor channel, the mobility inferred from THz spectroscopy represents an intrinsic, local (~10 nm) value due to the ultrafast oscillating nature of the THz electric field (~1 ps).[17] The local probe length is substantially smaller than the grain sizes of our samples. In a typical OPTP measurement, as schematically shown in Figure 2.6a, a 400 nm pulse with a duration of ~50 femtoseconds (fs) was employed to excite charge carriers from the valence to conduction band. The photoconductivity σ dynamics was then probed by a ~picoseconds (ps) THz pulse by controlling pump-probe delay time t_P. At a given pump-probe delay, σ is directly proportional to the pump-induced THz absorption ΔE by $\sigma \propto -\Delta E / E_0$. Figure 4.6b compared the photoconductivity dynamics for films deposited at RT and 120 °C. The fast 1 ps rise corresponds to the generation of free carriers in the film, followed by decay with a lifetime in the range of 10's of ps. Given the time scale, the decay dynamics could be tentatively attributed to charge trapping at defects. In principle, the photoconductivity of free carriers σ is defined by $\sigma = ne\mu = (N_{abs}\varphi)\, e\mu$, with n the carrier density, μ the charge carrier mobility, N_{abs} the absorbed photon density, φ the photon-to-charge conversion efficiency, and e the elementary charge. For a better comparison, the photoconductivity was divided by the absorbed photon density N_{abs}. By assuming the same photon-to-charge conversion efficiency φ, such a normalization provides a direct comparison of the conductivity per charge carrier, i.e., the mobility of the samples under different treatments ($\sigma/N_{abs} \propto \mu$). As shown in Figure 4b, a ~25% higher charge carrier mobility for $(TEA)_2SnI_4$ films cast at 120 °C was observed in comparison to that deposited at RT. The estimated charge carrier mobility values at the peak of the photoconductivity are ~13 and ~16 $cm^2V^{-1}s^{-1}$ for samples prepared at RT and 120 °C, respectively, by assuming 100% photon-to-charge conversion efficiency (i.e., $N_{abs}=n$, or φ=100%). It should be noted that the estimated mobility represents the lower boundary of charge carrier mobility, as in reality $\varphi \leq 100\%$.

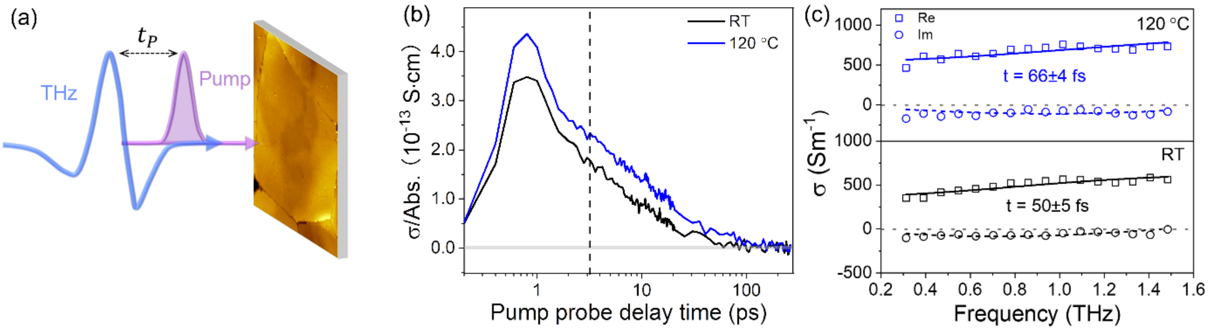

Figure 2.6. (a) Schematic of optical-pump THz-probe spectroscopic studies on the perovskites sample; (b) Comparison of photoconductivity σ normalized to the absorbed photon density

(N_{abs}) for RT and 120 °C deposited $(TEA)_2SnI_4$ perovskites films. (c) Frequency-resolved photoconductivity spectra and corresponding Drude-Smith fittings for $(TEA)_2SnI_4$ films cast at RT and 120 °C.

To gain more insights into the charge carrier transport, the frequency-resolved complex photoconductivity spectrum was recorded (at the pump-probe delay time of 3.2 ps as indicated in the dynamics) and is presented in Figure 2.6c. For both deposition conditions at RT and 120 °C, a unique combination of the significant real and nearly zero imaginary contributions to the photoconductivity are observed, indicating a free carrier-dominant charge transport behavior.[17] To quantitatively compare the charge transport in films from both deposition temperatures, the spectra were fitted by Drude-Smith (DS) model, which describes the free carrier transport in a medium with spatial confinement. The model reads:[17,18]

$$\sigma(\omega) = \frac{\omega_p^2 \varepsilon_0 \tau}{1-i\omega\tau}\left(1 + \frac{c}{1-i\omega\tau}\right) \qquad \text{(Equation 2.1)}$$

where ω_p is the plasma frequency ($\omega_p = \sqrt{\frac{n}{\varepsilon_0 \cdot m^*}}\, e$, m^* is the effective mass), τ is the charge scattering time, ε_0 is the vacuum permittivity, ω is the angular frequency. Different from the classical Drude model, the DS model takes into account the anisotropic backscattering effect due to e.g., presence of the grain boundaries by a parameter c ranging between 0 and -1. For $c = 0$, the DS model describes simply the Drude conductivity in which the free carriers transport with isotropic momentum scattering. For $c =$ -1, free carriers are assumed to experience strongly spatial confinement with 100% backscattering. From the fitting, the plasma frequency ω_p (related to charge carrier density n), c parameter, and charge scattering time τ can be inferred. Both ω_p and c parameters are found to be very similar, confirming our assumption of the same photon-to-carrier conversion efficiency and indicating the identical back scattering effect in both samples. On the other hand, the change in the scattering time dominates the charge transport, with τ =66 ± 4 fs and 50 ± 5 fs for 120 °C and RT cast films, respectively. Based on the inferred transport parameter, the charge carrier mobility in the *dc* limit was estimated, following $\mu = \frac{e \cdot \tau}{m^*} \cdot (1 + c)$. This indicates a 28% mobility enhancement from 207 ± 21 $cm^2V^{-1}s^{-1}$ for RT deposited samples to 265 ± 16 $cm^2V^{-1}s^{-1}$ for the 120 °C hot cast film. Combining the similar photoconductivity enhancement observed (in the OPTP data), our analysis on the frequency-resolved conductivity indicates the dominant role of charge scattering time on determining the charge carrier mobility. As such, it can be concluded that the hot casted film lowers the density of the charge scattering centers, very likely due to the slightly improved crystallinity as observed by GIWAXS. It should also be noted that the improvement of the local charge carrier mobility remains in a moderate range as the grain size is sufficiently large to play a minor role in dictating the local carrier mobility by THz spectroscopy.

2.4.4 Transient absorption spectroscopy

The excited state dynamics of the samples were further measured using transient absorption spectroscopy by Naz Ugur and Dr. Charusheela Ramanan. The samples were photoexcited at 529 nm. Global analysis of the data using a 3-compartment model yields the evolution associated difference spectra in Figure 2.7a and b. The transient spectra for the two samples are very similar. Negative peaks <550 nm and at 625 nm correspond to the ground-state bleach and there is an overlapping excited state absorption between 550-700 nm. The spectral evolution and the three components fit correlate with literature report of other 2D Sn-based perovskites.[19] While the spectral evolution of room temperature and hot-casted films are similar, the excited state decay dynamics differ. Hot-casted perovskite sample exhibited a longer excited state lifetime than reference sample, evidenced by the comparison of the transient kinetics at 620 nm (Figure 2.7c) and the slower decay rates from the global fit. The measured photoluminescence quantum yield (PLQY) values for the two perovskite films prepared at room temperature and 120 °C are 0.1% and 0.2%, respectively. The slower excited state decay and higher PLQY value of hot-casted film is consistent with a relative reduction in non-radiative decay from defect sites.

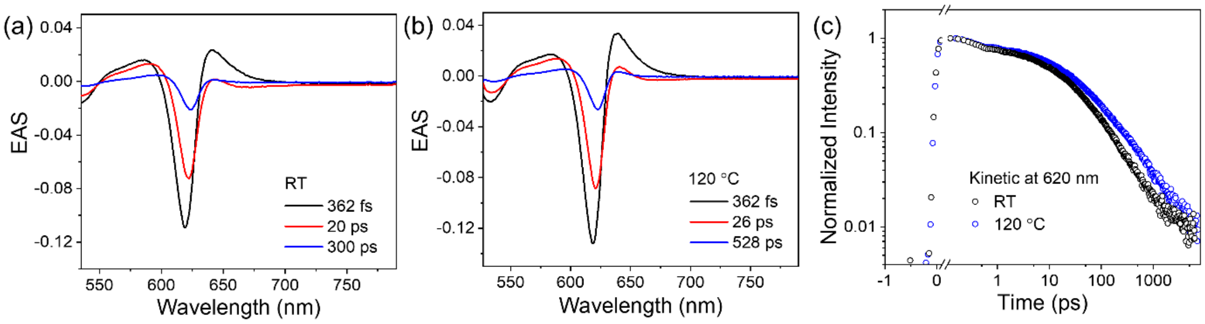

Figure 2.7. Time resolved transient absorption spectra of the 2D $(TEA)_2SnI_4$ perovskite layers prepared at (a) room temperature and (b) 120 °C by hot-casting. Delay times are indicated in the plots. (c) Kinetic traces at probe wavelength of 620 nm for the two perovskite films.

2.5 Device performance of 2D $(TEA)_2SnI_4$ perovskite FETs

To understand the role of grain size and crystallinity on the macroscopic charge carrier transport in FETs, the $(TEA)_2SnI_4$ perovskite films processed at different temperatures were integrated in bottom-gate top-contact devices (Figure 2.8a). Ultraviolet photoemission spectroscopy (UPS) was performed to analyze the electronic structure of $(TEA)_2SnI_4$, as shown in Figure 2.8b and c (measured by Dr. Hao Lu). The valence-band maximum VBM and conduction-band minimums CBM are determined to be 5.26 and 3.32 eV, respectively. The energy alignment of the $(TEA)_2SnI_4$ film at the Au/perovskite interface ensures an efficient hole injection into the active layer.[20] The hole transfer characteristics in Figure 2.8d-f were recorded at V_{DS} = –60 V with V_{GS} scanning from +60 V to –60 V for $(TEA)_2SnI_4$ FETs fabricated at RT and 120 °C. The device characteristics were measured at three typical temperatures of 100 K, 200 K, and 295 K. FETs cast at RT show weak *p*-type field modulated conduction and a high OFF current, especially at 295 K. The threshold voltage V_{TH} of 40 V is determined in the linear region and forward direction of the transfer curves. The hole mobility of 0.04 $cm^2V^{-1}s^{-1}$ at 295 K is extracted from the linear region of the square root of the transfer curve (forward sweep). In contrast, an overall improved device operation is observed for the 120 °C hot-cast $(TEA)_2SnI_4$ FETs. Meanhwile, the ΔV_{hys} is defined to analyze the degree of the hysteresis in the transfer characteristics for $|I_{ds}|$ = 1 µA under both sweeping directions. FETs hot-cast at 120 °C show ΔV_{hys} of 21 V at RT, which is smaller than 30 V of the RT processed device. The reduced hysteresis is related to the suppressed ion movement as a consequence of lower density of grain boundaries and reduced traps at the perovskite/dielectric interface. Furthermore, a significantly reduced OFF current, enhanced $I_{ON/OFF}$ over 10^4 and improved gate modulation are observed for the hot casted FETs.

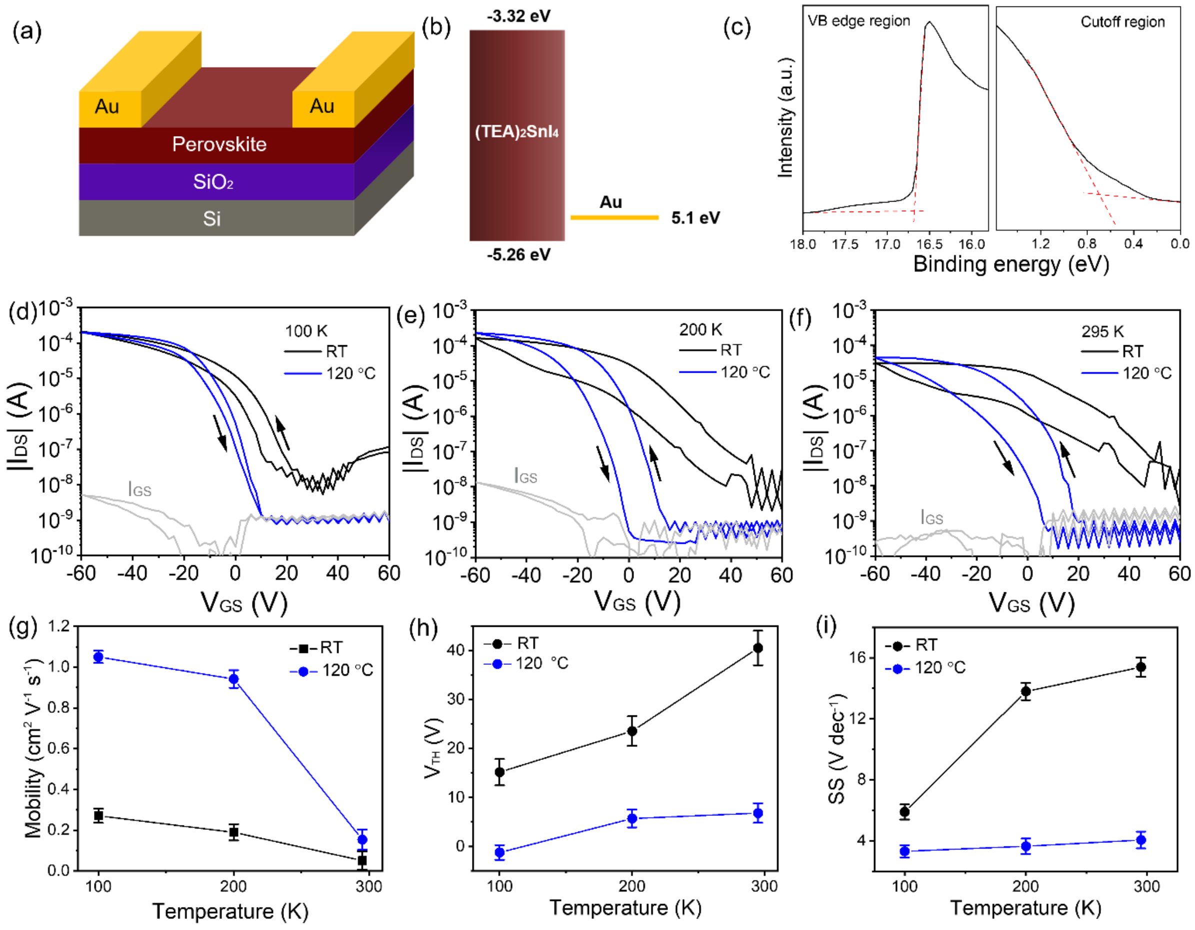

Figure 2.8. (a) Schematic of the bottom-gate top-contact $(TEA)_2SnI_4$ FET device structure. (b) The energy level of $(TEA)_2SnI_4$ semiconductor film and Au electrode. (c) Ultraviolet photoelectron spectroscopy (UPS) of $(TEA)_2SnI_4$ perovskite thin film. Transfer characteristics measured at (d) 100 K, (e) 200 K, and (f) 295 K with L = 30 μm, W = 1000 μm. The gray curves are the leakage currents (I_{GS}) between the source and gate electrodes in the 120 °C cast device. (g) Average hole charge carrier mobility, (h) threshold voltage and (i) subthreshold swing as a function of FET temperature. The error bars were calculated from 12 devices.

The optimized devices reveal higher ON current, which again confirms that the larger grain size dominantly facilitates the charge transport in the FET channel. It is worth noting that the optimized device showed significantly decreased OFF current, which originates from the leakage current I_{GS} of the device leading to poor modulation of the gate voltage.[21] The hole mobility μ in optimized FET at 295 K increases almost 4-fold to 0.15 $cm^2V^{-1}s^{-1}$ accompanied by a notably decreased V_{TH} of 6.6 V and smaller subthreshold swing SS of 4.05 V dec^{-1}. The interface trap density N_t at the dielectric/perovskite interface was further calculated from SS using the following equation:[22]

$$SS = \frac{K_B T ln10}{q}\left[1 + \frac{q^2}{C_i}N_t\right] \qquad \text{(Equation 2.2)}$$

where the C_i the areal capacitance of the dielectric layer; q the elementary charge; K_B the Boltzmann constant; and T the absolute temperature. Accordingly, the N_t of RT prepared FETs was calculated to be 1.88×10^{13} $cm^{-2}eV^{-1}$, which was notably reduced to $\sim4.8\times10^{12}$ $cm^{-2}eV^{-1}$ for the 120 °C cast FETs. These results suggest that the hot-cast strategy improves the film quality at the perovskite/dielectric interface such as order and morphology, contributing to the lower SS value and reduced interface trap density.[23] The reduced defects was also evidenced by transient absorption spectroscopy measurement (Figure 2.7). However, the experimentally determined charge mobility is under these conditions much lower than that extracted from the THz measurements. The large difference implies a critical role of grain boundaries and ion migration on charge carrier transport in FETs.[4] In general, ion migration can be significantly suppressed by lowering temperature leading to smaller hysteresis of the transfer curves, as illustrated also in this case in Figure 2.8d-f. The better device performance with smaller dual-sweep hysteresis is obtained at lower temperature for both $(TEA)_2SnI_4$ films. Specifically, at 100 K FETs cast at both temperatures, RT and 120 °C, reveal enhanced mobility values of 0.27 $cm^2V^{-1}s^{-1}$ and 1.05 $cm^2V^{-1}s^{-1}$, respectively, with the hot-casting FET mobility only an order of magnitude lower than the local mobility measured using the THz setup. The reason for the poor mobility of the RT cast $(TEA)_2SnI_4$ perovskite FETs can therefore be attributed to the large number of grain boundaries and low quality of the perovskite/dielectric interface. As mentioned before, the ion migration can be preferentially moved at grain boundaries.[24] Considering the varied density of grain boundaries in the $(TEA)_2SnI_4$ films cast at different temperatures and the above analysis, two primary mechanisms take place in the FET devices. At low operation temperature, at which ion migration is suppressed at a great extent, the grain boundaries act mainly trap centers for the charge carriers. This is the primary reason for the better hot-casting FET performance. As the operating temperature increases, grain boundaries facilitate ion drift, screening of the gate potential, and finally hindering of the gate modulation of the electronic current. Therefore, for FETs with large grain sizes, V_{TH} shifts only slightly to higher voltages with higher temperatures, while for the devices with small grains, this shift is much more pronounced.[25]

2.6 Channel length dependence of 2D $(TEA)_2SnI_4$ perovskite FETs

Notably, the device performance of the hot-cast films was further improved by using longer channel lengths. Figure 2.9 shows the device performance of 120 °C hot-cast $(TEA)_2SnI_4$ FETs for various channel lengths (10, 30, 50 and 80 µm). Upon the increase of the channel length, the operational parameters of the FETs are improved at both room and low temperature. When the channel length is enlarged from 10 µm to 80 µm for devices measured at 295 K, the charge carrier mobility increases from 0.08 $cm^2V^{-1}s^{-1}$ to 0.34 $cm^2V^{-1}s^{-1}$, and at the same time a reduction of V_{TH} from 14 V to 7 V and of SS from 4.3 V dec^{-1} to 3.7 V dec^{-1} are obtained. On the other hand, $I_{\mathrm{ON/OFF}}$ is almost independent of channel length. A similar enhancement in charge carrier mobility, as well as V_{TH} and SS values are observed at 100 K. The maximum mobility of 1.8 $cm^2V^{-1}s^{-1}$ is achieved for the device at 100 K with the channel length of 80 µm. The higher device performance is ascribed to the reduced contribution of the contact resistance (R_{C}) relative to the total resistance.[26] Additionally, to better understand the correlation between the channel length and ion movement, the impedance spectroscopy was utilized to explore the processes in transistors with various channel lengths at 295 K. Figure 2.10 compares the real parts of the dielectric constant for $(TEA)_2SnI_4$ FETs with different channel lengths as a function of frequency. The dielectric constant for the transistor with the channel length of 80 µm slightly increases at low-frequency.

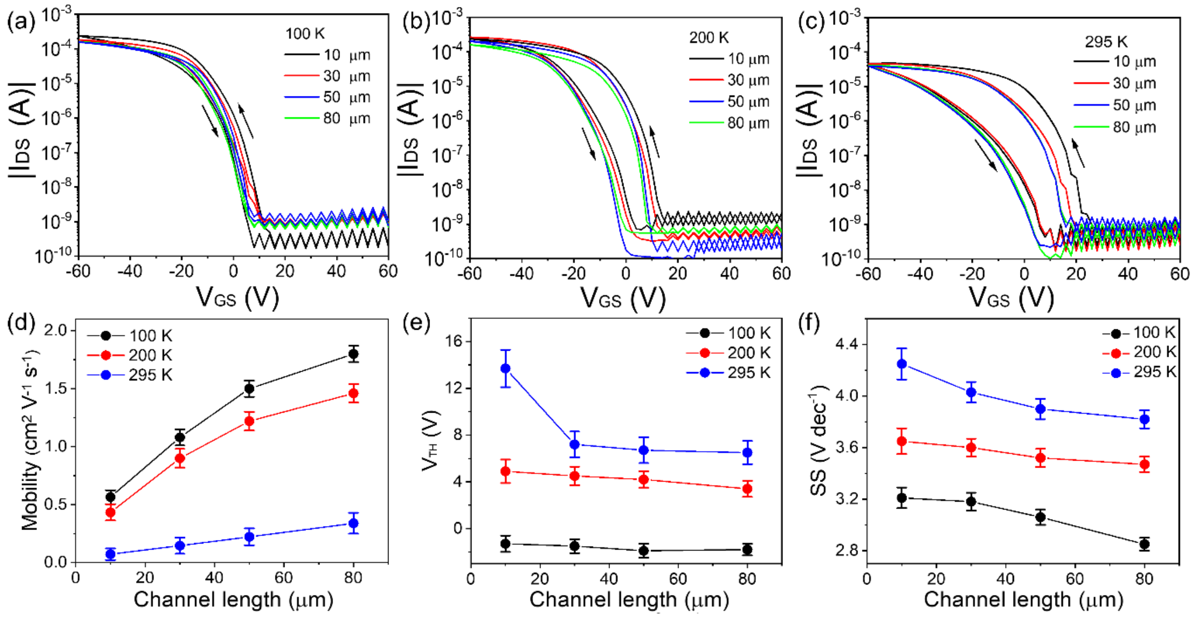

Figure 2.9. Transfer characteristics measured at (a) 100 K, (b) 200 K, and (c) 295 K of 120 °C hot-casting $(TEA)_2SnI_4$ FETs with different channel lengths L from 10 µm to 80 µm and constant W = 1000 µm. (d) Average charge carrier mobility, (e) threshold voltage, and (f) subthreshold swing as a function of channel length measured for $(TEA)_2SnI_4$ FETs at 100 K, 200 K and 295 K. The error bars were calculated from 12 devices.

The devices with shorter channels show a significantly higher dielectric response in the low-frequency region in comparison to devices with larger channel lengths because of the accumulation of mobile ions at the electrodes. Such electrode polarization is in fact typical for perovskite-based devices and can significantly influence the spatial distribution and response behavior of the charge carriers within the active perovskites film.[27] When the positive ions accumulate at the negatively charged electrode interface, charge carriers extraction is blocked by the accumulated ions. Meanwhile, an ion-induced electric field is formed with the direction opposite to the external electric field, which impedes charge carrier transport.[28] As the channel length increases, the polarization effect has lower impact on the total channel resistance resulting in high performance of the devices, which is consistent with the observed reduction in hysteresis for longer channel lengths.

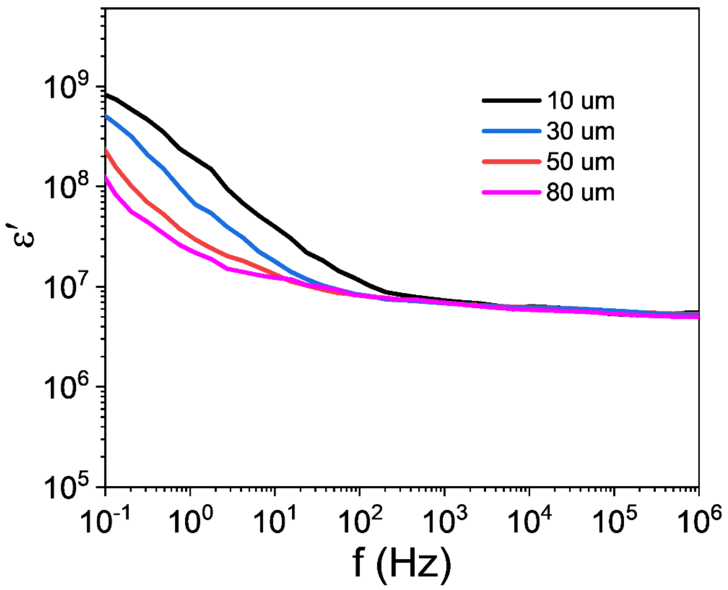

Figure 2.10. The real part of dielectric constant for perovskite films as a function of frequency measured in the top contact geometry for different channel lengths.

2.7 Conclusion

In this Chapter, I studied the device behavior of 2D lead-free perovskite FETs based on $(TEA)_2SnI_4$ thin films. The hot-casting strategy was employed to control the growth kinetics and morphology of the perovskite film to enhance the charge carrier transport and mitigate ion migration in the FET devices. An optimized substrate temperature was identified for the growth of large grains. Since film crystallinity remains identical for all deposition temperatures, only a moderate increase in the local charge carrier mobility of 16 $cm^2V^{-1}s^{-1}$ at room temperature, is observed, as confirmed by THz spectroscopy. On the other hand, the device parameters such as mobility, threshold voltage, subthreshold swing and hysteresis are significantly improved in devices with larger grains, as well as in devices with an increased channel length or/and low operation temperature. The reduced grain boundaries enabled drastic mitigation of the ion migration and the corresponding screening effects of the effective applied electric field in the device. Devices with maximum hole mobility of 0.34 $cm^2V^{-1}s^{-1}$ at 295 K and 1.8 $cm^2V^{-1}s^{-1}$ at 100 K were obtained.

The content of this chapter has been published in: Materials Horizons

Reprinted with permission from (Mater. Horiz. 2022, 9.10: 2633-2643)

Author contributions

Dr. Tomasz Marszalek conceived the idea; Dr. Tomasz Marszalek and Prof. Dr. Wojciech Pisula supervised the study; Shuanglong Wang prepared the samples and fabricated the devices. Sabine Frisch synthesized the organic cations under the supervision of Prof. Dr. Milan Kivala; Okan Yildiz carried out GIWAXS measurement and data analysis under the supervision of Dr. Tomasz Marszalek; Heng Zhang performed THz measurement and analyzed the data with support from Dr. Hai I. Wang; Dr. Mukunda Mandal conducted the DFT calculations and analyzed the data with support from Denis Andrienko; Naz Ugur, and Dr. Charusheela Ramanan performed transient absorption spectroscopy measurement; Dr. Beomjin Jeong provided helpful discussion; Prof. Dr. Mischa Bonn and Prof. Dr. Paul W. M. Blom coordinated the work. Shuanglong Wang prepared the manuscript with support from all co-authors; all authors discussed the results and contributed to this work.

2.8 Reference

1. T. Matsushima, S. Hwang, A. S. Sandanayaka, C. Qin, S. Terakawa, T. Fujihara, M. Yahiro and C. Adachi, *Adv. Mater.*, 2016, **28**, 10275.
2. H. Zhu, A. Liu, K. I. Shim, J. Hong, J. W. Han and Y. Y. Noh, *Adv. Mater.*, 2020, **32**, 2002717.
3. C. Jie, Y. Zhou, Y. P. Fu, J. Pan, O. F. Mohammed and O. M. Bakr, *Chem. Rev.*, 2021, **121**, 12112.
4. W. Nie, H. Tsai, R. Asadpour, J. C. Blancon, A. J. Neukirch, G. Gupta, J. J. Crochet, M. Chhowalla, S. Tretiak, M. A. Alam and H. L. Wang, *Science*, 2015, **347**, 522.
5. A. Liang, Y. Gao, R. Asadpour, Z. Wei, B. P. Finkenauer, L. Jin, J. Yang, K. Wang, K. Chen, P. Liao and C. Zhu, *J. Am. Chem. Soc*, 2021, **143**, 15215.
6. C. Ni, Y. Huang, T. Zeng, D. Chen, H. Chen, M. Wei, A. Johnston, A. H. Proppe, Z. Ning, E. H. Sargent and P. Hu, *Angew. Chem.*, 2020, **132**, 14081.
7. D. Lu, G. Lv, Z. Xu, Y. Dong, X. Ji and Y. Liu, *J. Am. Chem. Soc.*, 2020, **142**, 11114.
8. J. T. Lin, C. C. Liao, C. S. Hsu, D. G. Chen, H. M. Chen, M. K. Tsai, P. T. Chou and C. W. Chiu, *J. Am. Chem. Soc.*, 2019, **141**, 10324.
9. M. Dyksik, H. Duim, X. Zhu, Z. Yang, M. Gen, Y. Kohama, S. Adjokatse, D. K. Maude, M. A. Loi, D. A. Egger and M. Baranowski, *ACS Energy Lett.*, 2020, **5**, 3609.
10. F. Paulus, C. Tyznik, O. D. Jurchescu and Y. Vaynzof, *Adv. Funct. Mater.*, 2021, **31**, 2101029.
11. D. B. Kim, S. Lee, C. H. Jang, J. H. Park, A. Y. Lee and M. H. Song, *Adv. Mater. Interfaces*, 2020, **7**, 1902158.
12. Z. Li, C. Xiao, Y. Yang, S. P. Harvey, D. H. Kim, J. A. Christians, M. Yang, P. Schulz, S. U. Nanayakkara, C. S. Jiang and J. M. Luther, *Energy Environ. Sci.*, 2017, **10**, 1234.
13. Q. Chen, H. Zhou, Z. Hong, S. Luo, H. S. Duan, H. H. Wang, Y. Liu, G. Li and Y. Yang, *J. Am. Chem. Soc*, 2014, **136**, 622.
14. R. Li, C. Yi, R. Ge, W. Zou, L. Cheng, N. Wang, J. Wang and W. Huang, *Appl. Phys. Lett.*, 2016, **109**, 151101.
15. Z. Wang, F. Wang, B. Zhao, S. Qu, T. Hayat, A. Alsaedi, L. Sui, K. Yuan, J. Zhang, Z. Wei and Z. A. Tan, *J. Phys. Chem. Lett.*, 2020, **11**, 1120.

16. Y. Gao, Z. Wei, P. Yoo, E. Shi, M. Zeller, C. Zhu, P. Liao and L. Dou, *J. Am. Chem. Soc*, 2019, **141**, 15577.
17. R. Ulbricht, E. Hendry, J. Shan, T. F. Heinz and M. Bonn, *Rev Mod Phys.*, 2011, **83**, 543.
18. N. V. Smith, *Phys. Lett. A*, 1968, **26**, 126.
19. T. J. Zhang, C. C. Zhou, X. Z. Feng, N. N. Dong, H. Chen, X. F. Chen, L. Zhang, J. Lin and J. Wang, *Nat. Commun.*, 2022, **13**, 1.
20. S. Shao, W. Talsma, M. Pitaro, J. Dong, S. Kahmann, A. J. Rommens, G. Portale and M. A. Loi, *Adv. Funct. Mater*, 2021, **31**, 2008478.
21. F. Zhang, Q. Zhang, X. Liu, Y. Hu, Z. Lou, Y. Hou and F. Teng, *ACS Appl. Mater. Interfaces*, 2021, **13**, 4272.
22. Y. Reo, H. Zhu, J. Y. Go, K. I. Shim, A. Liu, T. Zou, H. Jung, H. Kim, J. Hong, J. W. Han and Y. Y. Noh, *Chem. Mater*, 2021, **33**, 2498.
23. S. P. Senanayak, B. Yang, T. H. Thomas, N. Giesbrecht, W. Huang, E. Gann, B. Nair, K. Goedel, S. Guha, X. Moya and C. R. McNeill, *Sci. Adv*., 2017, **3**, 1601935.
24. R. Lin, K. Xiao, Z. Qin, Q. Han, C. Zhang, M. Wei, M. I. Saidaminov, Y. Gao, J. Xu, M. Xiao and A. Li, *Nat. Energy*, 2019, **4**, 864.
25. J. Chen, T. Shi, X. Li, B. Zhou, H. Cao and Y. Wang, *Appl. Phys. Lett*, 2016, **108**, 053302.
26. T. Matsushima, S. Hwang, S. Terakawa, T. Fujihara, A. S. Sandanayaka, C. Qin and C. Adachi, *Appl. Phys. Express*, 2017, **10**, 024103.
27. R. Su, Z. Xu, J. Wu, D. Luo, Q. Hu, W. Yang, X. Yang, R. Zhang, H. Yu, T. P. Russell and Q. Gong, *Nat. Commun*, 2021, **12**, 1.
28. S. Zhang, Z. Y. Lin, E. Shi, B. P. Finkenauer, Y. Gao, A. J. Pistone, K. Ma, B. M. Savoie and L. Dou, *Adv. Mater*., 2021, **33**, 2105183.

Chapter 3 Modification of 2-thiopheneethylammonium tin iodide perovskite by pentanoic acid

3.1 Introduction

2D Sn-based perovskites are promising semiconductors for high performance FETs.[1,2] The Sn-based perovskites typically show high charge carrier mobility due to the smaller in-plane effective mass and longer carrier lifetime compared with their Pb analogues.[3] Nevertheless, there are several drawbacks for 2D Sn-based perovskite FETs. Firstly, an easy oxidation of Sn^{2+} to its tetravalent state Sn^{4+}, especially during solution processing, giving rise to ionic defects and leading to *p*-type self-doping.[4] Secondly, the fast crystallization rate of Sn-based perovskites as compared to Pb counterparts results in poor film morphology and low surface coverage.[5] Therefore, controlling the crystallization and oxidation to reduce defects and charge traps are crucial in suppressing ion migration and maximizing the charge carrier transport in 2D Sn-perovskite films with respect to the ultimate FET performance.

As described in Chapter 3, I introduced $(TEA)_2SnI_4$ perovskite thin films by hot-casting to control the film crystallization and morphology. The increased grain size resulted in an overall enhanced FET performance with pronounced gate modulation.[6] Nevertheless, the oxidation issue is still a challenge for $(TEA)_2SnI_4$ perovskite FETs. As an alternative strategy, introducing additives into the precursor solution has been demonstrated to be an effective and facile method in modulating perovskite crystallization, passivating defects and improving charge transport in solar cells.[7-9] However, a deep understanding of the influence of additives on the crystallization process of 2D tin halide perovskites is still missing, which prevents further rational design of additive molecules for perovskites FETs.

In this Chapter, I proposed a simple and effective additive engineering strategy via incorporation of a pentanoic acid (PA) molecule with a carboxylic group into the perovskite precursor solution. The effects of PA on the passivation of defects, film formation, crystallinity, and device performance of two-dimensional $(TEA)_2SnI_4$ based FETs were systematically investigated. It was demonstrated that PA interacts with TEAI and $[SnI_6]^{4-}$ through hydrogen and coordination bonding effectively improving crystallinity, enlarging grain size, and reducing defect density. Kelvin probe force microscopy (KPFM) measurement further confirmed the additive effect and the origin of the improvement in FET performance. As a result, the *p*-channel $(TEA)_2SnI_4$ transistors exhibited increased charge carrier mobility at room temperature from 0.2 $cm^2V^{-1}s^{-1}$ of the control device to 0.7 $cm^2V^{-1}s^{-1}$ with additive treatment. The higher mobility of 2.3 $cm^2V^{-1}s^{-1}$ along with reduced dual-sweep hysteresis was further obtained at low temperature 100 K.

3.2 NMR of precursor solution

The chemical structures of the organic spacer TEA and additive PA are shown in Figure 3.1a. Liquid-state ^1H and ^{119}Sn nuclear magnetic resonance (NMR) spectroscopy was firstly performed by Constantin Haese and Dr. Robert Graf in order to understand and identify the interaction between PA and the perovskite precursors TEAI and SnI_2. Different contents of PA are used from 0, 0.25, 0.5, 0.75, to 1 vol % in the precursor solution. The preparation details of the precursor solution are described in the Experimental Section. Firstly, a plain PA solution without the perovskite precursors is probed and the result is shown in Figure 3.1b. The resonance signal with ^1H chemical shift at 11.9 parts per million (ppm) can be attributed to the active hydrogen in the carboxylic group of PA. Then PA is added as additive at various volumes to the TEAI precursor deuterated dimethyl sulfoxide-*d*$_6$ (DMSO-d_6) solution. In the ^1H NMR spectra for the PA+TEAI mix solution, gradual emerging of the PA signal is observed with its higher concentration indicating the formation of $O{=}C{-}OH\cdots I^-$ hydrogen bonding with a significant exchange dynamic. In addition, ^{119}Sn NMR spectra are analyzed after addition of PA to the SnI_2 solution at different concentrations (Figure 3.1c). Figure 3.1d shows the ^{119}Sn chemical shift as a function of the PA volume ratio. The observed down-field shift of the ^{119}Sn

signal with increasing PA concentration can be explained by the electronic deshielding of the Sn^{2+} ion during its coordination bonding to the oxygen of PA in the form of HO─C═O···Sn^{2+}.[10] From these results, it can be concluded that PA undergoes hydrogen (O─H···I) and coordination bonding (C═O···Sn) by the carboxylic group with iodide and tin atoms of the precursors (Figure 3.1e).

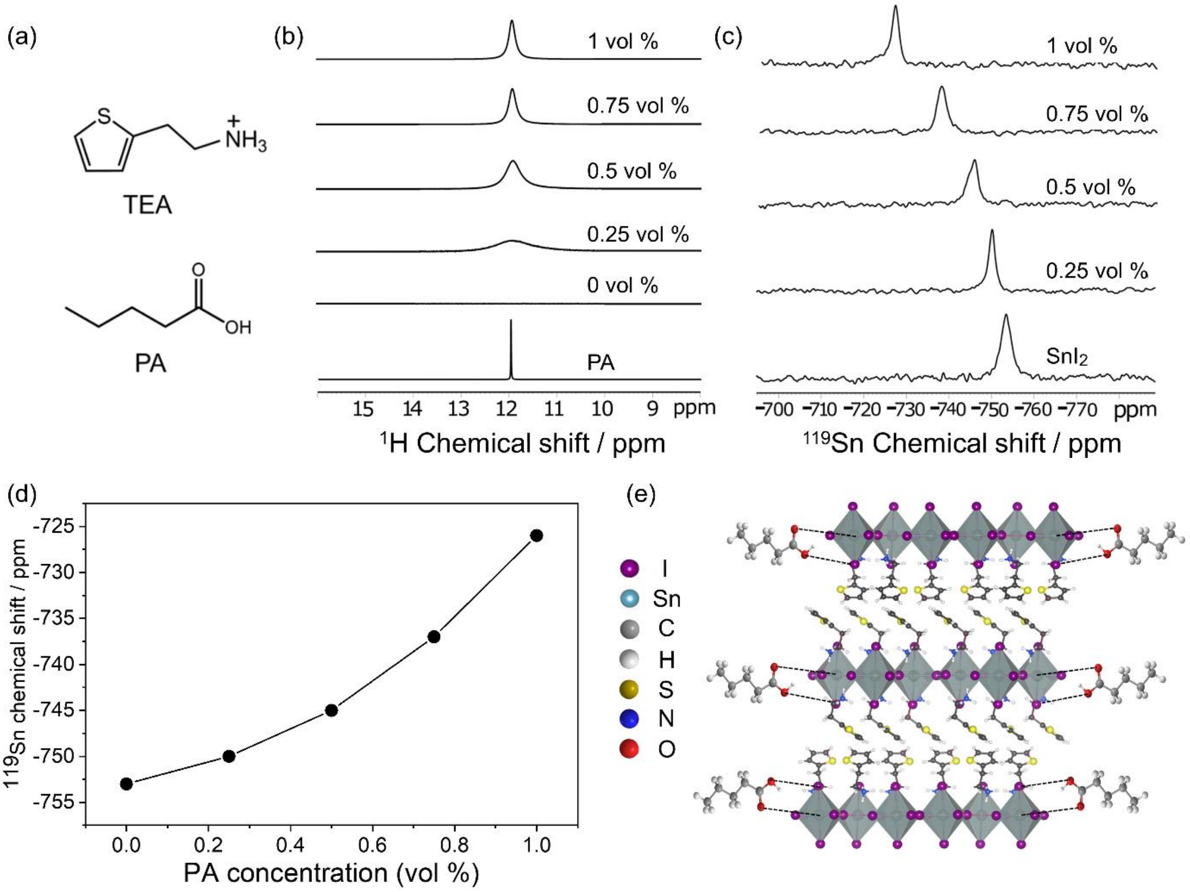

Figure 3.1. (a) Chemical structures of organic spacer TEA and additive PA; (b) ^{1}H NMR spectra of TEAI with different concentrations of PA (from bottom to top: pristine to 1 vol %) in DMSO-d_6 solution; (c) ^{119}Sn NMR spectra of SnI_2 with different concentrations of PA in DMSO-d_6 solution; (d) Summarized ^{119}Sn chemical shifts as a function of the PA volume ratio. (e) Representation of hydrogen bonding (O─H···I) and coordination bonding (C═O···Sn) between PA and $(TEA)_2SnI_4$.

3.3 Thin Film characterizations

To verify the influence of the PA additive on the surface morphology of the perovskite films, AFM measurements were performed for pristine and PA modified $(TEA)_2SnI_4$ films deposited on a silicon/silicone dioxide wafer and the corresponding results are shown in Figure

3.2a-e. The control film without additive exhibits small grain size as confirmed by literature.[11] Inferior film morphology and poor film coverage with numerous inevitably unfavorable pinholes appear due to the fast crystallization, which is a typical drawback for tin-based perovskites.[12] Upon addition of PA to the $(TEA)_2SnI_4$ precursor solution, smoother and more homogeneous films with less pinholes are obtained. Furthermore, the grain size increases to around 4 µm at a PA concentration of 0.5 vol %. The dependence of the grain size on PA concentration is shown in Figure 3.2f. It was postulated that the strong interaction between the PA additive and the precursors initiates heterogeneous nucleation centers inducing crystal growth preferentially at these nucleation sites, which induces the growth of perovskite grains with high surface coverage.[13]

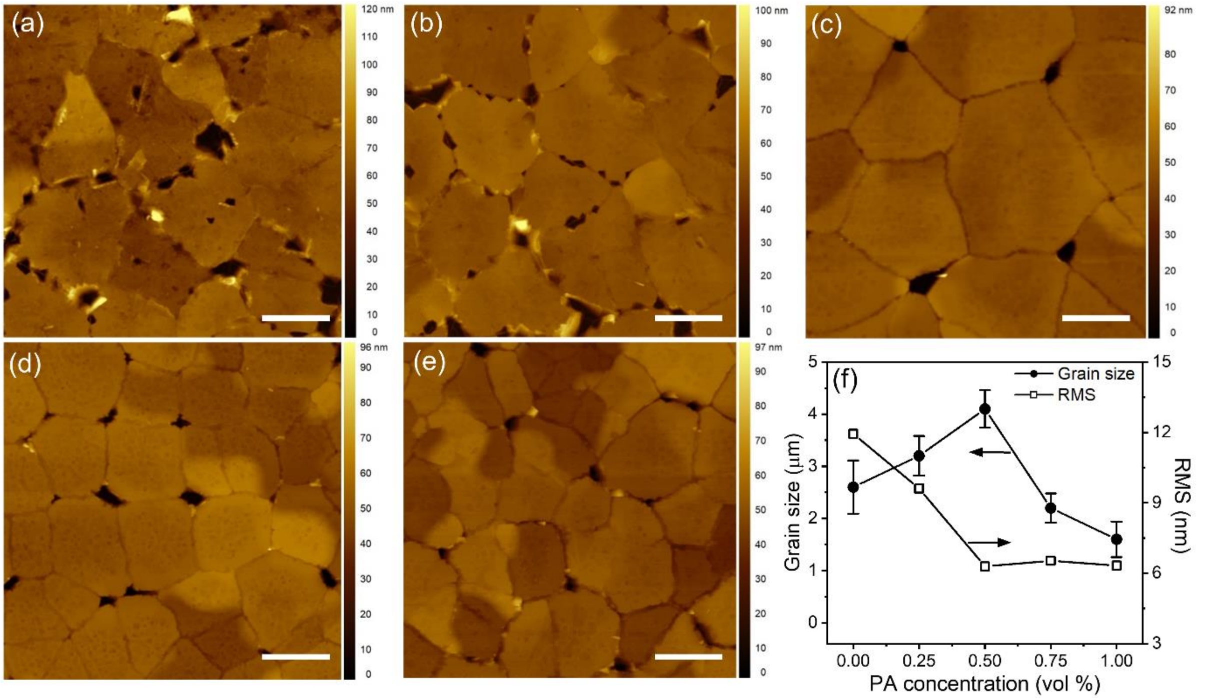

Figure 3.2. AFM height images of $(TEA)_2SnI_4$ films with PA at the concentration of (a) pristine; (b) 0.25 vol %; (c) 0.5 vol %; (d) 0.75 vol % and (e) 1 vol %. Scale bar in all images is 2 µm. (f) Grain size distribution and surface roughness of $(TEA)_2SnI_4$ films as a function of PA concentration.

In addition, the perovskite film with 0.5 vol % PA exhibits a much smaller surface roughness with a root-mean-square RMS value of 6.3 nm in comparison to 11.9 nm for the pristine sample. A smoother film surface is beneficial for the contact between the electrodes and perovskite film in the FET facilitating carrier injection and extraction.[14] The RMS values for all perovskite films are summarized in Figure 3.2f. At higher PA levels between 0.5 vol % to 1 vol % the grain size clearly decreases compared with the pristine sample, probably due to an excessive formation of heterogeneous nucleation sites in the precursor solution.[15] The results demonstrate that the PA additive effectively tunes the crystallization process and improves film morphology including the surface roughness and grain size, which is expected to enhance the electronic properties of the perovskite films in FET devices.

Based on the above AFM results, the PA concentration of 0.5 vol % as an optimum was chosen to investigate the impact of the additive on the crystal structure and molecular organization of the $(TEA)_2SnI_4$ films by XRD and GIWAXS measurements. Figure 3.3a shows the XRD patterns of the corresponding two $(TEA)_2SnI_4$ films without and with 0.5% vol PA. The two samples exhibit the typical (00l) out-of-plane organization (l = 2, 4, 6, 8, 10, and 12) indicating a layered structure.[16] Both films show the same position for the (002) diffraction peak at 5.68°, while the calculated interlayer spacing D_{002} is 15.6 Å. These results prove that the PA additive does not cause any disruption of the out-of-plane lattice in the layered perovskite structure. The films with 0.5% vol PA additive exhibit substantially increased intensities of the main diffraction peaks compared with the pristine film, although the two films have the same thickness. In addition, the corresponding full width at half maximum FWHM values are extracted to be 0.23° and 0.21°, respectively, suggesting slightly improved out-of-plane crystallinity of the film with PA. GIWAXS measurements was further executed to understand the contribution of the PA additive on the molecular organization (performed by Okan Yildiz). The crystal coherence lengths in the (002) direction calculated from the Scherrer equation are 197 nm for pristine and 236 nm for the optimized $(TEA)_2SnI_4$ film as shown in Figure 3.3b and c. Higher order reflections including (004) are observed in the film with PA indicating a long-range organization of crystal structures in out-of-plane direction of the film, further confirming the XRD results. From the out-of-plane position of the (00l) reflections it is possible to conclude that the inorganic part $[SnI_6]^{4-}$ is organized parallel to the substrate, which is favorable for the in-plane charge carrier transport in FETs.[17] The in-plane integration of the peak intensity for q_{xy} from 0° to 15° is shown in Figure 3.3d. The in-plane (010) and (020) reflections are attributed to Sn-I and I-Sn-I bonds with corresponding *d*-spacing values of 2.9 Å and 5.8 Å, which agree well with literature.[18] However, the (020) reflection is missing for the film with PA additive compared to the pristine $(TEA)_2SnI_4$ film, probably due to the strong interaction between PA and the inorganic $[SnI_6]^{4-}$ framework.

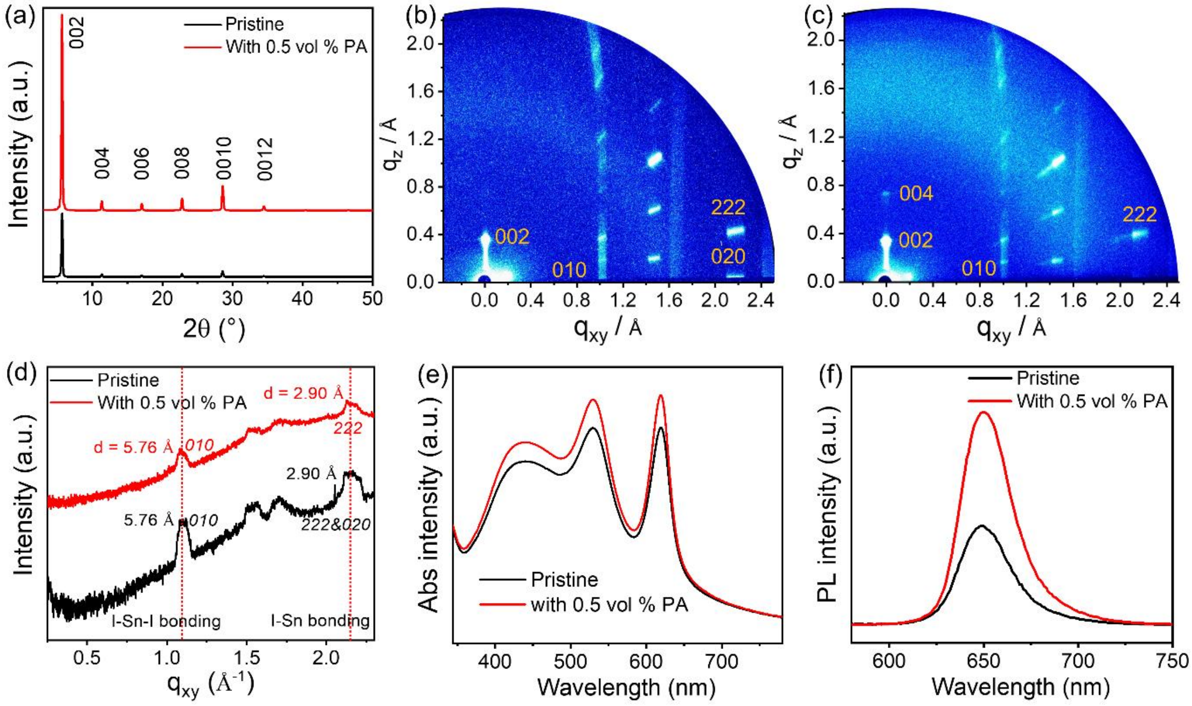

Figure 3.3. (a) XRD and (b, c) GIWAXS patterns (main reflections are assigned by Miller indices) for pristine and PA containing $(TEA)_2SnI_4$ films; (d) the in-plane profiles of both GIWAXS patterns; (e) UV-vis absorption and (f) PL spectra.

To evaluate the impact of the PA additive on the optoelectronic properties of the $(TEA)_2SnI_4$ films, the UV-vis absorption and steady-state PL spectra of pristine and films with 0.5 vol % PA were measured, as shown in Figure 3.3e and f. In the absorption spectra, both $(TEA)_2SnI_4$ films without and with 0.5 vol % PA show three peaks at 440, 529, and 619 nm, where the sharp absorption peak at 619 nm can be attributed to the intrinsic exciton absorption in the crystal lattice. The film with 0.5 vol % PA exhibits slightly stronger absorption than the pristine one. Similar behavior is observed in the PL spectra. The stronger PL intensity for the film with 0.5 vol % PA in comparison to the pristine sample indicates a reduced number of defects within the optimized perovskite layer.[19]

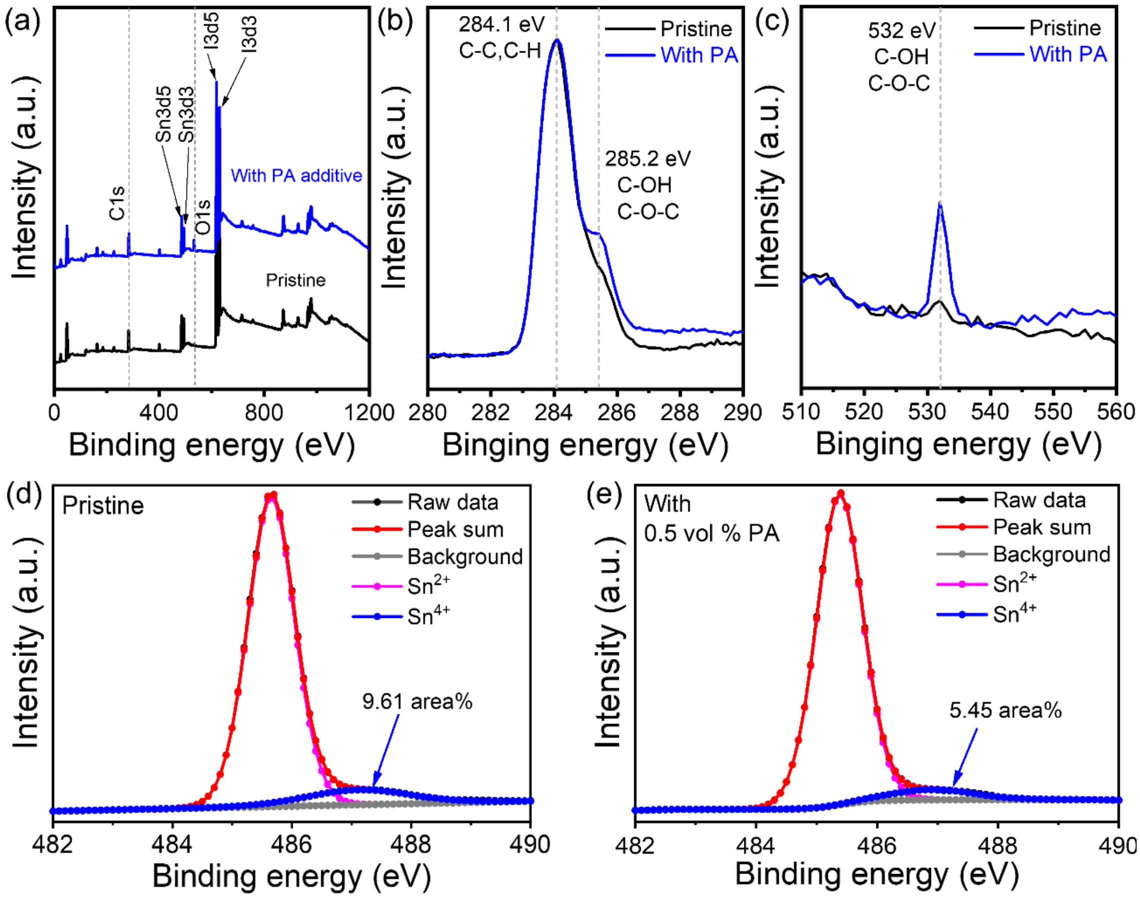

Figure 3.4. XPS wide spectra (a) and the corresponding high-resolution spectra for C1s (b), and (c) O1s of pristine and optimized PA added $(TEA)_2SnI_4$ films; XPS spectra of Sn3d for $(TEA)_2SnI_4$ films prepared without (d) and with (e) PA. The peak fitting indicates the ratio changes of Sn^{4+} upon additive.

X-ray photoelectron spectra (XPS) characterization was used to identify the existence of PA additive and Sn^{2+} oxidation for pristine and 0.5 vol % PA based $(TEA)_2SnI_4$ films (measured by Leon Prädel). Then the XPS wide spectra was analyzed in-depth for pristine and optimized PA added $(TEA)_2SnI_4$ films (Figure 3.4a). As the PA additive contains carbon and oxygen elements, the XPS peaks of C1s, and O1s for pristine and PA-based $(TEA)_2SnI_4$ films were compared. From elemental analysis, I found a distinct shoulder peak for C1s at 285.2 eV

(Figure 3.4b and c) and an overall increased amount of C concentration for the $(TEA)_2SnI_4$ film with PA additive. For O1s, a dominant peak at 532 eV was observed, which can be assigned to C−OH and C−O−C groups. Therefore, the above analysis confirmed that the PA additive is successfully incorporated into the perovskite film. Additionally, the Sn3d XPS spectra confirms that Sn from $(TEA)_2SnI_4$ is the active site to coordinate with the O=C─OH units in PA, since the peak exhibits a shift towards a lower binding energy from pristine to PA added $(TEA)_2SnI_4$ films (Figure 3.4d and e). More importantly, a reduced proportion of Sn^{4+} from 9.61 atomic % for the pristine sample to 5.45 atomic % for the PA-based $(TEA)_2SnI_4$ film was also observed. Since Sn^{2+} is prone to be oxidized to the Sn^{4+} ionic defect which can occur either in precursor solution and/or during film formation processing. Therefore, minimizing the Sn^{4+} valence state is desirable to reduce the trap density and prolong the carrier diffusion length in the film.[20] From the XPS results, it could be concluded that the PA additive can effectively passivate defects through strong retardation of Sn^{2+} oxidation.

3.4 PA modified $(TEA)_2SnI_4$ perovskite FETs

To study the effect of PA on the electrical properties of the $(TEA)_2SnI_4$ semiconducting film and determine the optimum concentration of PA in the perovskite films regarding the device performance, FETs with a bottom-gate top-contact geometry were fabricated, as shown in Figure 3.5a. The transfer characteristics were recorded at V_{DS} = –60 V with V_{GS} scanned from +60 V to –60 V in pulse mode (see more details in experimental part). Figure 3.5b and c shows the statistics of the charge carrier mobility and hysteresis (V_{GS} difference at $|I_{DS}| = 10^{-7}$ A of both sweeping directions) in the transfer characteristics as a function of the PA concentration at 295 K. The mobility is extracted from the saturation region of the transfer curve in forward direction. The pristine $(TEA)_2SnI_4$ FET reveals *p*-channel FET characteristics with average hole mobility of 0.2 $cm^2V^{-1}s^{-1}$, SS of 5 V dec^{-1}, $I_{ON/OFF}$ of 1.5×10^4, and V_{TH} of 33 V. The FETs based on the additive PA at various concentrations exhibit markedly improved overall performance.

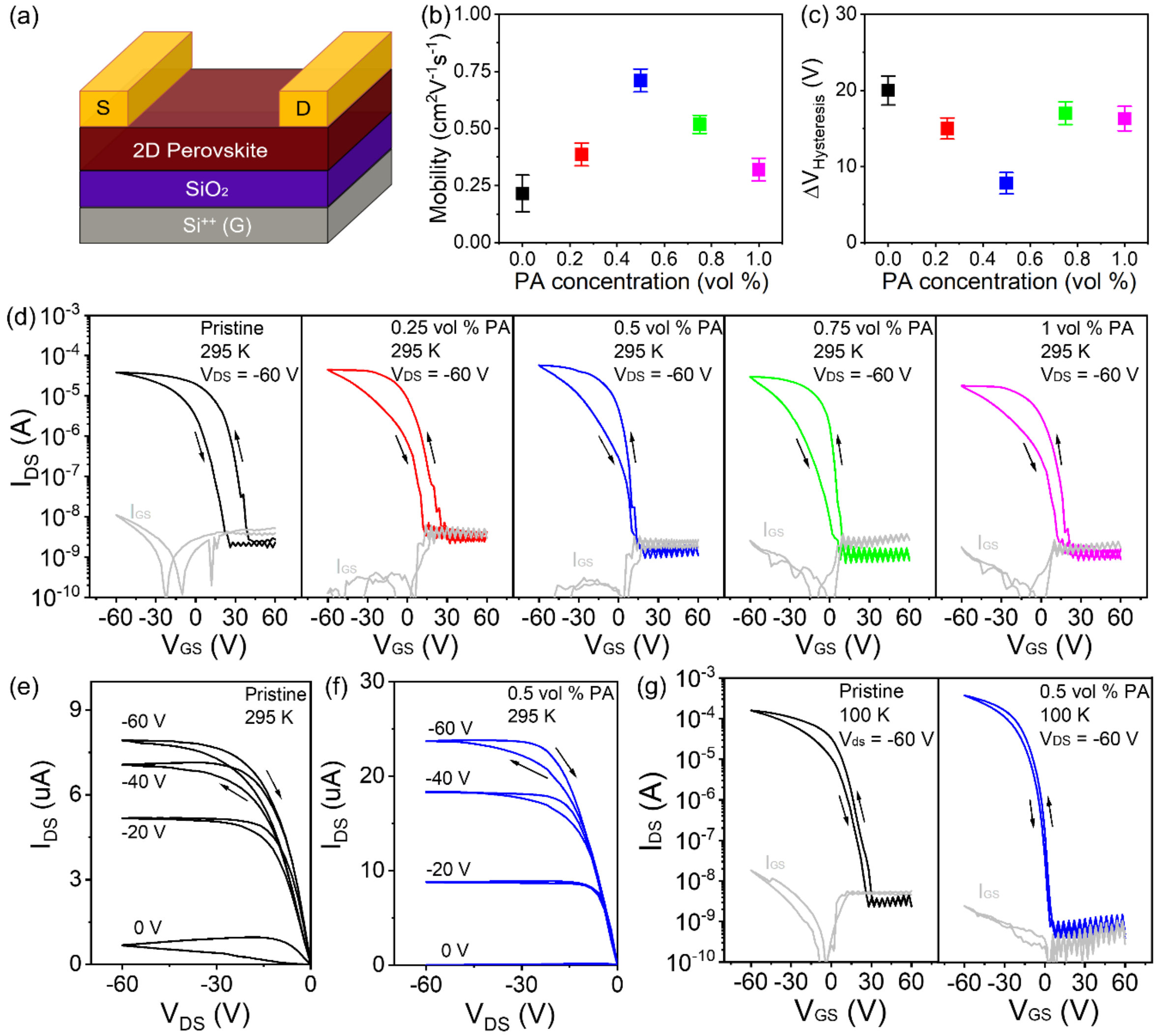

Figure 3.5. (a) Device structure of $(TEA)_2SnI_4$ FETs. (b) Charge carrier mobility and (c) hysteresis width of $(TEA)_2SnI_4$ FETs with different PA concentrations. Error bars present standard deviation calculated from 12 devices per type. (d) Transfer characteristics at 295 K (I_{GS} is the gate leakage current). Corresponding output characteristics of pristine (e) and PA-based (at 0.5 vol %) devices (f) at 295 K. (g) Transfer characteristics of pristine and modified devices with PA concentration of 0.5 vol % at 100 K. Arrows indicate the direction of the sweeps.

Notably, the device with 0.5 vol % PA demonstrates the best performance. At the optimal PA concentration of 0.5 vol % the maximum channel current in the transfer curve corresponds to a smaller SS value of 2.9 V dec^{-1}, a charge carrier mobility of 0.7 cm^{2}V^{-1}s^{-1}, an $I_{ON/OFF}$ of 6×10^4, and a V_{TH} of 9.0 V, representing a remarkable improvement in the transistor performance. In the device with PA additive, the V_{TH} values are significantly reduced compared to the pristine FET demonstrating that the PA additive effectively eliminates defects. However, V_{TH} increases for higher concentration of PA possibly due to the insulating nature of the PA additive, reduced grain size, and increased number of grain boundaries. Based on the repeated measurements of a large number of devices, the device performance is confirmed to be highly reliable and reproducible with a small standard deviation of ± 0.053 $cm^2V^{-1}s^{-1}$. The trap density N_t at the dielectric/perovskite interface with the whole channel area of 80 µm × 1000 µm is calculated using SS values by the described Equation 2.2 in Chapter 2. Accordingly, N_t decreases from 6.1×10^{12} $cm^{-2}eV^{-1}$ for the pristine FET to 3.5×10^{12} $cm^{-2}eV^{-1}$ for the 0.5 vol % PA-based FET. However, when the PA concentration is further increased to 1 vol %, the trap density N_t rises again to 5.6×10^{12} $cm^{-2}eV^{-1}$, which can be ascribed to the decreased grain size leading to a high density of grain boundaries. These results suggest that the additive at optimal concentration improves the film quality at the perovskite/dielectric interface contributing to lower SS and reduced trap density. When the PA concentration is further increased, a declined device performance is observed. The PA concentration of 1 vol % leads to a decreased mobility of 0.3 $cm^2V^{-1}s^{-1}$, as shown in Figure 3.5d.

The above results reveal an optimum PA concentration to achieve the highest device performance. At a too high concentration, the insulating properties of the additive and reduced grain size possibly result in poor charge transport.[21] The output characteristics of the optimal device at 295 K in Figure 3.5f is significantly improved compared to the pristine device in Figure 3.5e, which shows a weak gate modulation of the current. These observations further confirm the beneficial effect of PA on the electronic properties of $(TEA)_2SnI_4$ FETs and more details on the charge transport are discussed below. It is worth noting that the hysteresis directions of the output and transfer curves are opposite. Perovskite-based transistors exhibit gradually expanded hysteresis when the bias sweep rate changes in the presence of ion migration.[8] For this reason, the transfer characteristics were recorded by using pulse mode to eliminate this effect. Nevertheless, V_{DS} in the output characteristics is changed in sweep mode. The sweep range of the output curve is from 0 V to -60 V and then back from -60 V to 0 V. These are the typical measurement modes for perovskite transistors.[22] It was assumed that due to the sweeping mode the polarization of the source and drain area occurs which results in clockwise hysteresis in the output characteristics. However, this aspect should be studied in more detail in the future. Photoelectron yield spectra was performed to analyze the electronic structure of pristine and optimized 0.5 vol % PA-based $(TEA)_2SnI_4$. As shown in Figure 3.6, the valence-band maximum VBM values are determined to be 5.18 and 5.23 eV, respectively. This indicates that the PA additive has negligible impact on the charge injection barrier at Au/perovskite interface in the FET devices.[23]

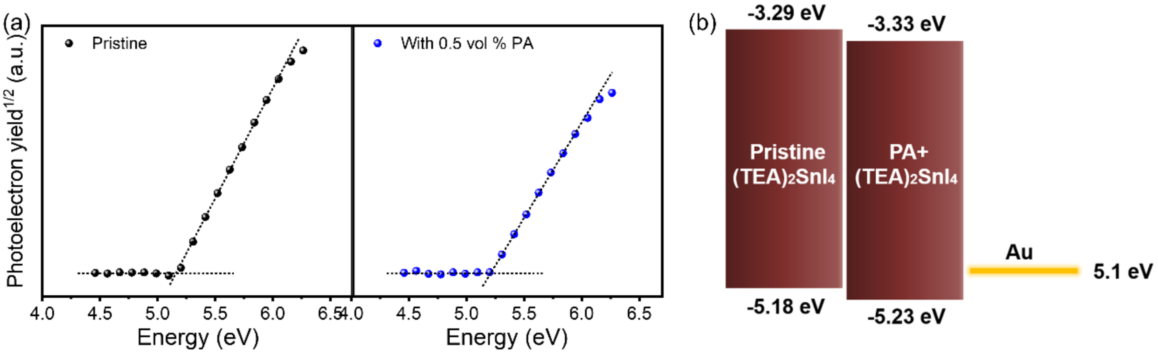

Figure 3.6. (a) Photoelectron yield spectra of pristine and optimized PA-based $(TEA)_2SnI_4$ thin films. (b) Schematic of the energy level of the corresponding perovskite thin films and Au electrode.

In addition to higher mobilities, the FETs based on $(TEA)_2SnI_4$ with PA also exhibit reduced dual-sweep hysteresis. To quantitatively analyze the hysteresis for the FET devices operating at room temperature, the width of the hysteresis for V_{GS} (ΔV) in forward and backward direction is calculated at $|I_{DS}| = 10^{-7}$ A, which is around halfway between the on and off states.[24,25] The pristine devices demonstrate a large ΔV of 19 V, which decreases to 8 V at the optimized PA concentration of 0.5 vol %. The lowered hysteresis is attributed to the strong interaction between PA and precursors which passivates defects, increases grain size, and inhibits ion migration in the film. It should be pointed out that the optimized device with 0.5 vol % PA additive still exhibits a gate voltage-dependent hysteresis in the transfer characteristics. When positive (negative) ions drift towards (away from) the interface under a negative gate voltage, the accumulation of these mobile ions shields the applied gate field and reduce the concentration of holes in the accumulation layer of the FET. The larger negative V_{GS} significantly increases the number of accumulated ions and strengthens the screening of the gate voltage.[8] At higher gate bias in the saturation region, it is assumed that all mobile ions are accumulated at the perovskite/dielectric interface. In this case, a further increase of the gate voltage has only negligible influence on the screening effect but increases the number of charge carriers, resulting in a lower hysteresis.

The hysteresis in metal halide perovskite transistors is generally believed to originate from ion migration and interface traps. The hysteresis induced by mobile ions is strongly dependent on the presence of defects in the perovskite films.[24] The enlarged grain size is also beneficial for the device performance due to the reduced grain boundaries which act as trap centers for charge carriers and pathways for ions in the perovskite film, as confirmed by our previous work.[6] Iodide vacancies are believed as main ionic defects in the solution-processed tin halide polycrystalline perovskite thin films due to their low formation energy during film processing.[26] In 2D $(TEA)_2SnI_4$ FETs, the spacer cation TEA is stable because of its large molecular size, so iodine anions are considered to be the dominant undesired mobile ions. The lateral mobile ions accumulate at electrode/semiconductor interface in the channel and create a built-in electric field opposite to the external applied V_{DS}, which seriously retards the in-plane charge carrier transport in the FET.[27] Due to the strong hydrogen and coordination bonding between PA and source materials, the density of defect-associated mobile ions is significantly suppressed accompanied with enlarged grain size, greatly improving charge transport, and reducing ion migration in the device during operation.

To further confirm the reduction of the defect density by PA treatment, the FET characteristics of pristine and PA treated films at low temperature of 100 K were investigated. Figure 3.5g shows the transfer characteristics of the pristine and optimized devices. The device with PA additive exhibits a high average μ of 2.3 $cm^2V^{-1}s^{-1}$ at 100 K. As the temperature decreases to 100 K, all devices show a reduced hysteresis compared with 295 K. This suggests that the mobile ions significantly contribute to the FET hysteresis at 295 K since it is generally believed that ion migration is drastically inhibited at low temperature. Nevertheless, even greatly suppressed, a hysteresis can be still observed at 100 K. The residual hysteresis at 100 K can be attributed to traps at the dielectric/perovskite interface.[28] In addition, the interface trap densities N_t were also calculated for the devices operated at 100 K based on the SS values extracted from transfer curves in forward direction. All devices show lower N_t values at 100 K than at 295 K, which are 5.8×10^{12}, 5.4×10^{12}, 2.7×10^{12}, 2.9×10^{12}, and 3.3×10^{12} $cm^{-2}eV^{-1}$, for the PA concentrations of 0, 0.25%, 0.5%, 0.75%, and 1%, respectively. The slightly increased interface trap densities N_t with higher PA concentration can be attributed to the moderately decreased grain size. It clearly shows that the N_t values are reduced with the PA concentration, further confirming that the strong hydrogen and coordination bonding between PA additive and precursor materials can effectively passivate the defects in the film and consequently improve the quality of the dielectric/perovskite interface. These results are in line with the drastically suppressed hysteresis in the output curves at 100 K. It should be pointed out that the output curve at 100 K shows a sublinear region at a small V_{DS}, which indicates contact resistance in the device. The effect of stationary ions cannot be neglected and they might contribute to the remaining contact resistance.[29] Through optimization of the contact resistance and/or the choice of optimized interlayers, some improvements in performance are expected to be achieved in the future.

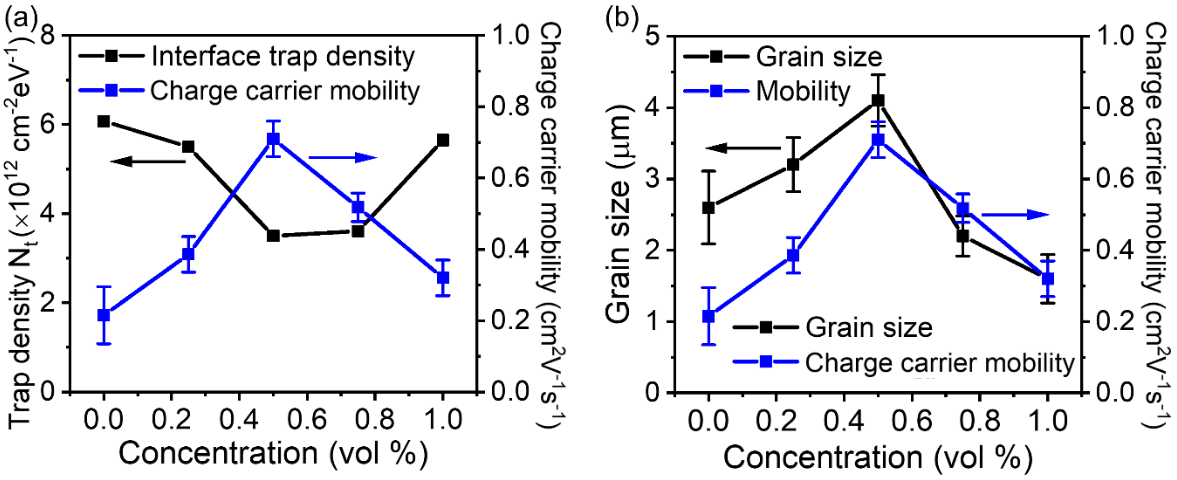

Figure 3.7. (a) Correlation between interface trap density and charge carrier mobility and the corresponding (b) correlation between grain size and charge carrier mobility for $(TEA)_2SnI_4$ FETs processed with different PA concentrations.

The correlation between the interface trap density and field-effect mobility for different PA concentrations at 295 K was then checked. Figure 3.7a reveals a clear correlation between trap density and mobility. The charge carrier mobility increases with lower interface trap density. On the contrary, the grain size is not closely linked to the charge carrier mobility as presented in Figure 3.7b, although both parameters exhibit similar trend with differences regarding the concentration of PA additive. For example, the pristine film shows grain size of around 2.6 μm, which is much larger than that of 1.6 μm in the film with the highest PA concentration of 1.0 vol %. However, the corresponding pristine device results a lower mobility. Additionally, $(TEA)_2SnI_4$ film without and 0.75 vol % PA exhibit similar grain sizes of around 2.6 and 2.2 μm, respectively. Nevertheless, the pristine $(TEA)_2SnI_4$ FET leads to a charge carrier mobility of 0.2 $cm^2V^{-1}s^{-1}$. This is significantly lower than the mobility of 0.52 $cm^2V^{-1}s^{-1}$ for the device with 0.75 vol % PA. Therefore, the above discussion further confirms that the superior FET performance for $(TEA)_2SnI_4$ films with optimized PA concentration can be ascribed to the two factors: defect passivation by suppressing Sn^{2+} oxidation and improved film morphology. Both of these effects synergistically result in the improved charge carrier transport and inhibited ion migration.

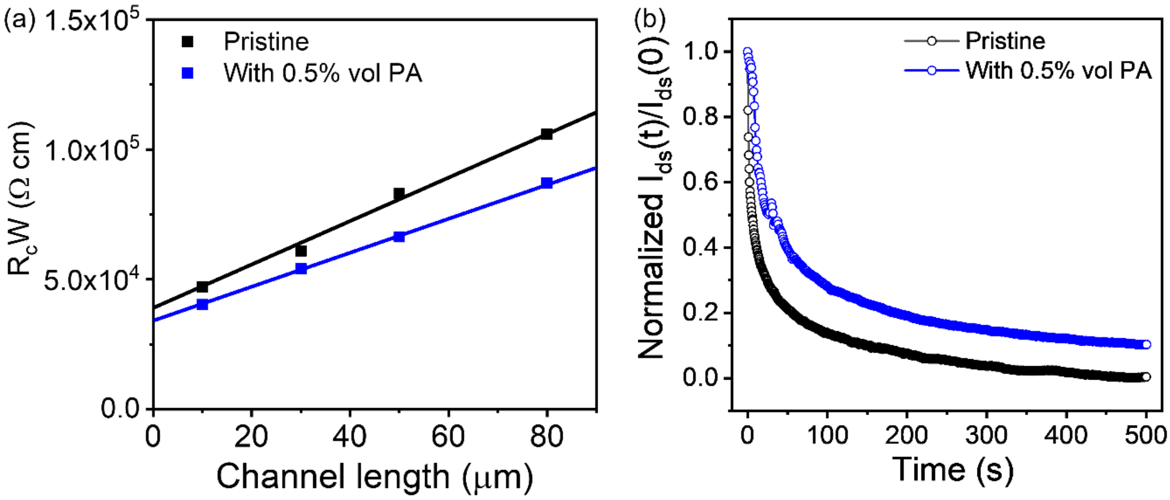

Figure 3.8. (a) Transmission-line method with RcW as a function of channel length for pristine and optimal 0.5 % vol PA-based $(TEA)_2SnI_4$ perovskite FETs at 295 K. The contact resistance is determined from the y-axis intercept. The drain current was collected from the linear region at V_{GS} = -60 V and V_{DS} = -6 V; (b) Normalized source-drain current as a function time under a constant bias of $V_{GS} = V_{DS}$ = -60 V for pristine (without PA) and optimized (with 0.5% vol PA) FETs.

The influence of the PA additive on the contact resistance (R_CW) in the devices was examined through the transmission line method (TLM).[6] As shown in Figure 3.8a, the contact resistance of 4.1×10^4 Ω cm for pristine devices is reduced to 3.5×10^4 Ω cm for the optimized 0.5 % vol PA-based FETs, which can be attributed to the decreased ionic defects by PA additive. The reduction of contact resistance is expected to improve the charge injection in FET devices. The bias stress stabilities were also investigated for pristine and 0.5 vol % PA optimized $(TEA)_2SnI_4$ FETs. Figure 3.8b shows the change in source-drain current under a constant bias of $V_{GS} = V_{DS}$ = -60 V for 500 s. The normalized source-drain current ($I_{DS}(t)/I_{DS}(0)$) of the pristine $(TEA)_2SnI_4$ FET degrades significantly faster than the optimized device. For example, the decay time to reach 20% of the initial channel current is significantly increased from 56 s to 185 s for the $(TEA)_2SnI_4$ FET with 0.5 vol % PA. The above results further confirm that the PA additive plays an efficient role in improving the device stability by effectively reducing defects and inhibiting ion migration.

3.5 Kelvin probe force microscopy

The above results demonstrate the beneficial effects of the additive engineering strategy proposed here on film formation and FET operation. To further investigate the microscopic origin of the improved FET performance by the addition of PA, the film morphology and the potential distribution were examined using KPFM (by Konstantinos Bidinakis, Franziska Hasenburg, and Prof. Dr. Stefan A. L. Weber). KPFM correlates the nanoscale sample topography with the local surface potential. With all electrodes grounded, the contact potential difference (CPD) between tip and sample give rise to electrostatic forces.[30] Compensating these electrostatic forces by applying an external bias to the tip allows to map the CPD variations. By establishing electrical connections for the source, drain and gate electrode, the voltage distribution across the FET channel can be mapped under operating conditions (See more details in Experimental part).[31] In order to avoid cross-talk to the KPFM signal from accentuated topographical features at the grain boundaries, heterodyne frequency-modulation KPFM was employed, which is deemed as most reliable KPFM method.

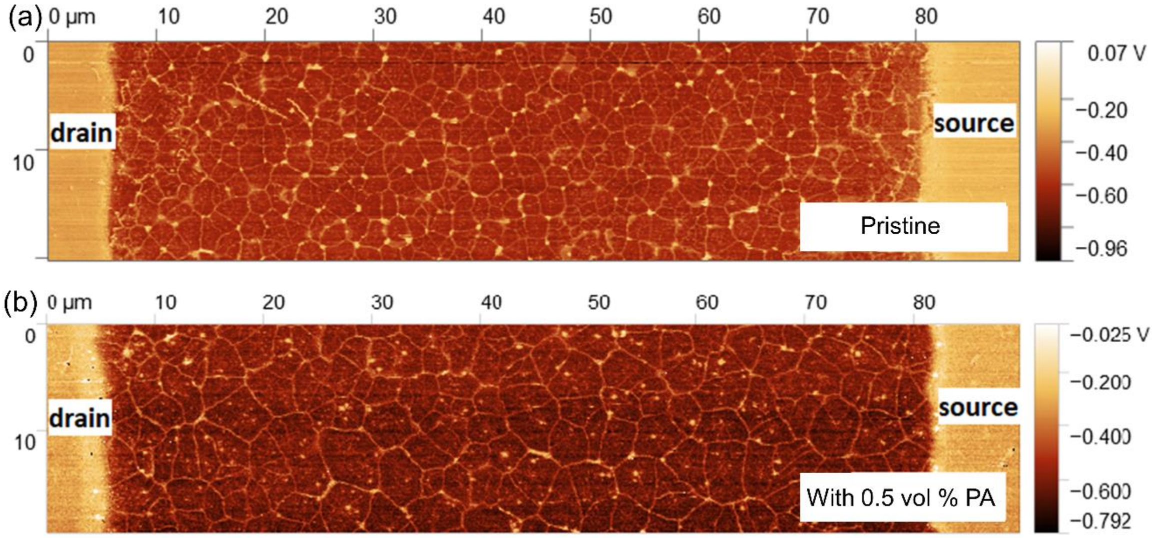

Figure 3.9. KPFM imaging when drain, source and gate are connected to ground for (a) the pristine and (b) the optimally modified device with 0.5 % vol PA.

Firstly, the effect of the additive in terms of the localization and passivation of defects in the perovskite film was analyzed. Since the charge carrier transport occurs laterally along the channel, defects giving rise to deep trap states within the band gap would pose a hindrance to charge flow from source to drain, and therefore negatively affecting the transistor performance. Moreover, these energy states are expected to cause band bending leading to a change in the measured CPD at the grain boundaries. At first step, KPFM was conducted while keeping all three FET electrodes grounded in order to map the relative work functions of the gold electrodes, perovskite grain interiors and grain boundaries. For both the pristine (Figure 3.9a) and the 0.5 vol % PA modified films (Figure 3.9b), a clear increase of the CPD at the grain boundaries with respect to the grain interiors was observed, which corresponds to energetic barriers for charge carrier movement. The superior structure in the sample treated with the additive in terms of a larger grain size distribution was identified. Having larger grains along the channel path means that charge carriers migrate through less energetically unfavorable boundaries, which could explain the better electronic characteristics for the optimized device when current flows across the channel.

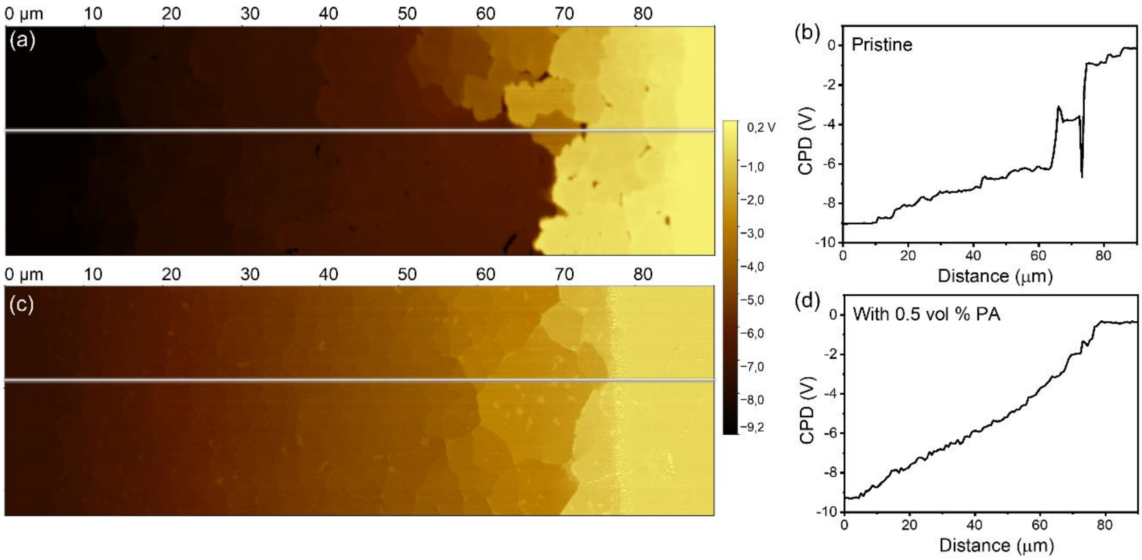

Figure 3.10. Potential maps and corresponding profiles of (a and b) for pristine and (c and d) optimized device measured with KPFM for V_{GS} = -44 V and V_{DS} = -9 V.

To investigate the advantage of the optimized morphology with additive engineering in transistors, KPFM measurements on pristine and modified devices under operating conditions were conducted (Figure 3.10a and c). Specifically, a voltage of -9 V was applied on the drain, while keeping the source grounded, which corresponded to the output characteristics (Figure 3.5e and f) in the linear regime. Additionally, a voltage of -44 V was applied to the gate accordingly, which exceeds the threshold voltage from the transfer characteristics in Figure 3.5 d and corresponds to a conductive channel. In the case of the pristine device, it can be seen that a potential decreases from source to drain in a step-wise manner. The large voltage drops correspond to resistive barriers to charge carrier flow, which seem to be more pronounced on certain grain boundaries. Previous studies on perovskite solar cells and FETs have linked this behavior to a pronounced ion migration and accumulation inside the perovskite film.[31] The extent by which ionic accumulation obstructs electronic charge carrier flow can be explained through simple electrostatics. It was proposed that the high density of ionic defects in the pristine device leads to an accentuated ion drift due to the source-drain voltage and hence ionic accumulation close to the electrode/semiconductor interfaces. This screens the applied electric field, thus inhibiting the charge flow required for device operation, as mentioned earlier. Since electrostatic fields are conservative, they relate to their corresponding electrical potential as: $E = -\nabla V$, or in 1D as: $E = -\frac{dV}{dx}$. For the calculation of the electric field in the pristine device due to ion migration n, the adjacent-averaging smoothing method is employed for the potential plot, in order to avoid artifacts in the electric field plot due to the differentiation.[32] On the other hand, the modified device exhibits a mostly continuous linear decline along the channel, implying that the current is only limited by the bulk lateral resistance of the perovskite. These results once again confirm that the addition of 0.5 vol % PA to the perovskite precursor solution is beneficial for device operation, as the current flow is less governed by the energy barriers at the grain boundaries.

3.6 Conclusion

In this Chapter, PA was incorporated as additive into the precursor solution for fabricating high performance 2D tin halide $(TEA)_2SnI_4$ FETs. I have found that the PA additive effectively modifies the perovskite nucleation process through the formation of hydrogen and coordination bonding. As a result, the $(TEA)_2SnI_4$ film with 0.5% vol PA shows significantly suppressed Sn^{2+} oxidation, improved film morphology regarding the surface roughness and grain size, and increased crystallinity, which synergistically augmented the FET performance with the highest mobility of 0.7 $cm^2V^{-1}s^{-1}$ at 295 K. This is a more than threefold enhancement compared to the control pristine device with 0.2 $cm^2V^{-1}s^{-1}$. In addition, the ionic induced hysteresis is greatly inhibited and the corresponding mechanism is elucidated. Moreover, benefiting from the reduced defects and ion migration, the optimal device results in a higher mobility of 2.3 $cm^2V^{-1}s^{-1}$ at 100 K.

The content of this chapter has been published in: Small

Reprinted with permission from (Small, 2023: 2207426.)

Author contributions

Shuanglong Wang conceived the idea and designed the experiment; Dr. Tomasz Marszalek and Prof. Dr. Wojciech Pisula supervised the study; Konstantinos Bidinakis and Franziska H. Hasenburg performed KPFM measurement and analyzed the data with support from Dr. Stefan A. L. Weber; Constantin Haese conducted the solution NMR measurement and analyzed the data with support from Dr. Robert Graf; Okan Yildiz and Zhitian Ling carried out GIWAXS measurement and data analysis under the supervision of Dr. Tomasz Marszalek; Sabine Frisch synthesized the organic cations under the supervision of Prof. Dr. Milan Kivala; Prof. Dr. Paul W. M. Blom coordinated the work. Shuanglong Wang prepared the manuscript with support from all co-authors. All authors discussed the results and contributed to this work.

3.7 References

1. C. R. Kagan, D. B. Mitzi and C. D. Dimitrakopoulos, *Science*, 1999, **286**, 945.
2. T. Matsushima, S. Hwang, A. S. Sandanayaka, C. Qin, S. Terakawa, T. Fujihara and C. Adachi, *Adv. Mater.*, 2016, **28**, 10275.
3. C. Qin, F. Zhang, L. Qin, X. Liu, H. Ji, L. Li, Y. Hu and Z. Lou, *Adv. Electron. Mater.*, 2021, **7**, 2100384.
4. A. Treglia, F. Ambrosio, S. Martani, G. Folpini, A. J. Barker, M. D. Albaqami and A. Petrozza, *Mater. Horiz.*, 2022, **9**, 1763.
5. J. Wang, Z. Gao, J. Yang, M. Lv, H. Chen, D. J. Xue and S. Yang, *Adv. Energy Mater.*, 2021, **11**, 2102131.
6. S. L. Wang, S. Frisch, H. Zhang, O. Yildiz, M. Mandal, N. Ugur, B. Jeong, C. Ramanan, D. Andrienko, H. I. Wang, M. Bonn, P. W. M. Blom, M. Kivala, W. Pisula and T. Marszalek, *Mater. Horiz.*, 2022, **9**, 2633.
7. J. Y. Go, H. Zhu, Y. Reo, H. Kim, A. Liu and Y. Y. Noh, *ACS Appl. Mater. Interfaces*, 2022, **14**, 9363.
8. Y. Reo, H. Zhu, J. Y. Go, K. In Shim, A. Liu, T. Zou and Y. Y. Noh, *Chem. Mater.*, 2021, **33**, 2498.
9. F. Zhang, Q. Zhang, X. Liu, L. Qin, Y. Hu, Z. Lou and F. Teng, *J. Mater. Chem. A*, 2021, **9**, 22842.
10. M. A. Ruiz-Preciado, D. J. Kubicki, A. Hofstetter, L. McGovern, M. H. Futscher, A. Ummadisingu and M. Grätzel, *J. Am. Chem. Soc.*, 2020, **142**, 1645.
11. Z. Zhu, X. Jiang, D. Yu, N. Yu, Z. Ning and Q. Mi, *ACS Energy Lett.*, 2022, **7**, 2079.
12. D. Cui, X. Liu, T. Wu, X. Lin, X. Luo, Y. Wu and L. Han, *Adv. Funct. Mater.*, 2021, **31**, 2100931.
13. X. Meng, Y. Li, Y. Qu, H. Chen, N. Jiang, M. Li and S. Yang, *Angew. Chem.*, 2021, **133**, 3737.
14. M. E. Kayesh, K. Matsuishi, R. Kaneko, S. Kazaoui, J. J. Lee, T. Noda and A. Islam, *ACS Energy Lett.*, 2018, **4**, 278.

15. M. Ulfa, P. Wang, J. Zhang, J. Liu, W. D. de Marcillac, L. Coolen and T. Pauporte, *ACS Appl. Mater. Interfaces*, 2018, **10**, 35118.

16. F. Lédée, P. Audebert, G. Trippé-Allard, L. Galmiche, D. Garrot, J. Marrot and C. Quarti, *Mater. Horiz.*, 2021, **8**, 1547.

17. H. Jia, H. Shi, R. Yu, H. Ma, Z. Wang, C. Zou and Z. A. Tan, *Small*, 2022, **18**, 2200036.

18. Y. Gao, Z. Wei, P. Yoo, E. Shi, M. Zeller, C. Zhu and L. Dou, *J. Am. Chem. Soc.*, 2019, **141**, 15577.

19. D. Hong, Y. Zhou, S. Wan, X. Hu, D. Xie and Y. Tian, *ACS Photonics*, 2018, **5**, 2034.

20. H. Liang, F. Yuan, A. Johnston, C. Gao, H. Choubisa, Y. Gao and E. H. Sargent, *Adv. Sci.*, 2020, **7**, 1903213.

21. M. Abdel-Shakour, T. H. Chowdhury, K. Matsuishi, I. Bedja, Y. Moritomo and A. Islam, *Sol. RRL*, 2021, **5**, 2000606.

22. S. P. Senanayak, M. Abdi-Jalebi, V. S. Kamboj, R. Carey, R. Shivanna, T. Tian and H. Sirringhaus, *Sci. Adv.*, 2020, **6**, 4948.

23. Z. Wang, F. Wang, B. Zhao, S. Qu, T. Hayat, A. Alsaedi and Z. A. Tan, *J. Phys. Chem. Lett.*, 2020, **11**, 1120.

24. H. Zhu, A. Liu, K. I. Shim, H. Jung, T. Zou, Y. Reo, H. Kim, J. W. Han, Y. Chen, H. Y. Chu, J. H. Lim, H.-J. Kim and Y. Y. Noh, *Nat. Commun.*, 2022, **13**, 1741.

25. H. Wan, Y. Cao, L. W. Lo, J. Zhao, N. Sepulveda and C. Wang, *ACS Nano*, 2020, **14**, 10402.

26. S. Zhao and L. Xiao, *Phys. Chem. Chem. Phys.*, 2022, **24**, 403.

27. F. Jiang, J. Pothoof, F. Muckel, R. Giridharagopal, J. Wang and D. S. Ginger, *ACS Energy Lett.*, 2020, **6**, 100.

28. I. Vladimirov, S. Müller, R. P. Baumann, T. Geßner, Z. Molla, S. Grigorian and R. T. Weitz, *Adv. Funct. Mater.*, 2019, **29**, 1807867.

29. F. Liu, L. Wang, J. Wang, F. Wang, Y. Chen, S. Zhang and C. Jiang, *Adv. Funct. Mater.*, 2021, **31**, 2005662.

30. A. Axt, I. M. Hermes, V. W. Bergmann, N. Tausendpfund, S. A. Weber and J. Beilstein, *Nanotechnol*, 2018, **9**, 1809.

31. L. Bürgi, H. Sirringhaus and R. H. Friend, *Appl. Phys. Lett.*, 2002, **80**, 2913.

32. S. A. Weber, I. M. Hermes, S. H. Turren-Cruz, C. Gort, V. W. Bergmann, L. Gilson and R. Berger, *Energy Environ. Sci.*, 2018, **11**, 2404.

Chapter 4 Odd-even effect in 2D tin halide perovskite FET based on spacer cation engineering

4.1 Introduction

In Chapter 2 and 3, I reported a TEA organic spacer in the 2D tin halide perovskite and demonstrated its feasibility for FET applications by grain and additive engineering. Meanwhile, with the rapid growth in the field of perovskite semiconductors, it has been shown that chemical structure tuning of organic spacer cations in 2D perovskite opens a simple but an effective pathway to improve the performance of optoelectronic devices.[1-3] In-depth insights into the relationship of organic cations and field-effect characteristics hold the key for understanding the mechanism of charge carrier transport in perovskite transistors. Nevertheless, most research of 2D tin halide perovskite FETs more focused on the morphology or grain engineering, doping or ionic substitution strategy.[4-6] The features of the bulky cation affect have yet to be fully explored, in part because the number of commercially available spacers is limited to the benchmarked cation phenylethylammonium (PEA).[7] The knowledge of the structural design rules of these organic cations, specifically the correlation between the chosen spacer and its impact on the properties of 2D perovskite film as well as the resulting FET performance, is thus far from being enough. Therefore, it’s an interesting yet under-explored direction to understand the mechanism of the targeted cation molecule and charge carrier dynamics in 2D quantum-well structure, thus driving the design and discovery of new organic spacer cations for FET applications.

In this Chapter, I systematically investigated the in-plane charge carrier transport properties in 2D tin halide perovskite FETs based on phenylalkylammonium iodides and demonstrated the influence of the molecular structure of cation spacers on charge carrier mobility by varying the alkyl chain length. These device mobilities exhibited strong oscillation regarding the number of carbon atoms on alkyl side chain. Combining optical pump-Terahertz probe (OPTP) spectroscopy and theoretical computational modeling, the correlations between structure formation and surface morphology as well as local and device mobility were determined, highlighting the importance of the molecular conformation of organic cations. These results indicate that the so far largely ignored alkyl chain length of PEA based organic cations plays a critical role in governing the microstructural morphology and crystal structure in 2D layered tin halide perovskite FETs, thus leading to mobility changes. This work provides a molecular-level understanding of the role of organic cations in optimizing the FETs devices performance based on 2D organic-inorganic perovskites.

4.2 Film characterization

The chemical structures of these four spacer cations with different alkyl chain lengths, namely phenylmethylammonium (PMA), PEA, phenylpropylammonium (PPA), and phenylbutanammonium (PBA), as shown in Figure 4.1a, have been previously reported as molecular passivators in three-dimensional perovskite light-emitting diodes, where the presence of the passivation treatment reduces the surface defects, leading to the high device performances.[8] For transistor applications, the PEA cation-based 2D perovskite has been already widely studied. On the other hand, little has been done to understand how the FET performance is impacted by the cations' chain length. This gives me the motivation to systematically investigate the correlation between the above bulky cations and their charge carrier transport properties in transistors. The optical absorption spectra of perovskite thin films deposited from different cations show overall similar patterns with three main absorption peaks. The third absorption peak at 593 nm, 612 nm, 581 nm, and 605 nm for $(PMA)_2SnI_4$, $(PEA)_2SnI_4$, $(PPA)_2SnI_4$ and $(PBA)_2SnI_4$, respectively, is attributed to the intrinsic exciton absorption in layered perovskite lattice (Figure 4.1b). Interestingly, there is a large blue-shifted with the presence of PMA and PPA spacer cation especially compared to other counterparts, indicating an increase in the optical bandgap. The variation of the absorption onset and the bandgap is generally believed to closely link to the changes in the structural properties of the perovskites. Previous works have shown that the distorted crystal geometries can increase the bandgap of perovskite materials.[9] Several parameters, including the octahedral tilt, Sn−I−Sn bond angles and penetration depth of the spacers, can affect the energetic landscape. Therefore, the crystal structures of these perovskites are critical to identify which of these factors has the most significant impact on the widening of their bandgap, and this will be discussed later in details.

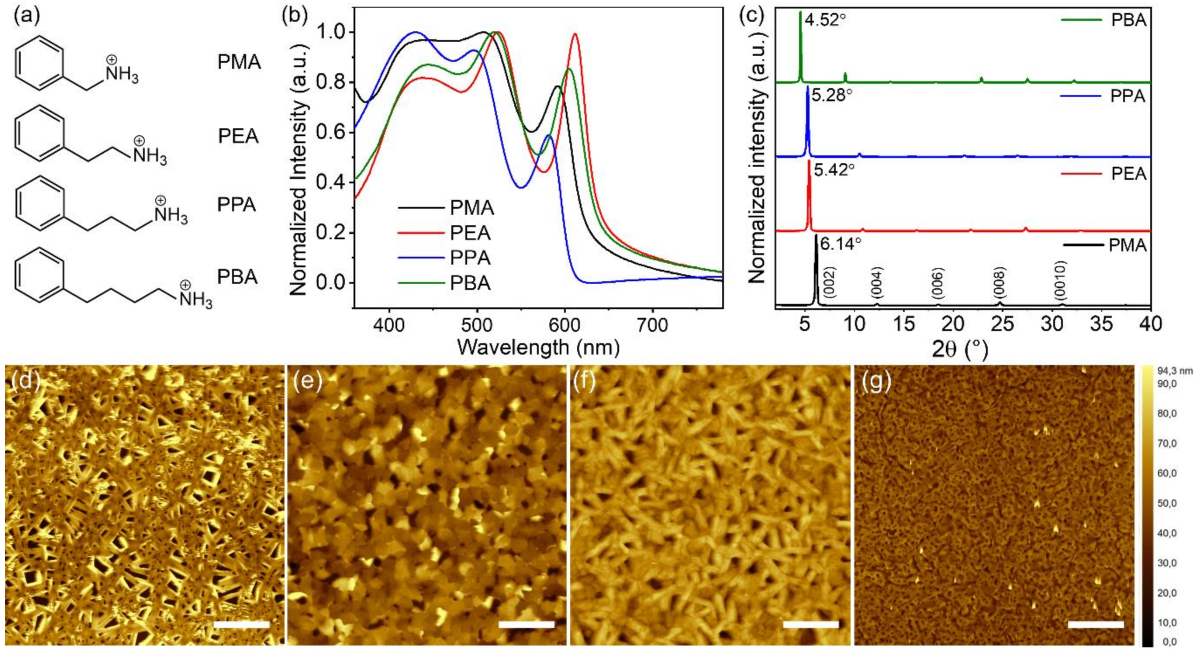

Figure 4.1. (a) The chemical structures of otganic spacers PMA, PEA, PPA and PBA; (b) The corresponding UV absorption spectra; (c) XRD patterns and (d-g) AFM height images (Scale bar: 10 µm) of the perovskite thin films based on these four cations.

XRD measurements at room temperature were performed to investigate the out-of-plane molecular organization of these four perovskites. As shown in Figure 4.1c, all the perovskite films display typical (00l) (l = 2, 4, 6, 8, 10, 12) diffraction peaks, indicating the formation of layered structure in the film. Based on the diffraction angle of the sharp (002) peak at 6.14°, 5.42°, 5.28°, and 4.58°, the interlayer distances between the inorganic layers are calculated as 14.4 Å, 16.3 Å, 16.7 Å, and 19.6 Å for (PMA)$_2$SnI$_4$, (PEA)$_2$SnI$_4$, (PPA)$_2$SnI$_4$ and (PBA)$_2$SnI$_4$ films, respectively. It is worth noting that the interlayer distances of the perovskites show nonlinear increase for PPA- and PBA-based cations. This may indicate the longer alkyl chain lengths offer a higher molecular degree of freedom, resulting in tilted alignment to the inorganic $[SnI_6]^{4-}$ compared to the shorter alkyl chains.[10] The surface morphology of perovskites is another key parameter to heavily influence the charge transport, which is referred to its uniformity, coverage, and roughness. AFM was then employed to evaluate the film morphology, as shown in Figure 4.1d-g. Interestingly, PMA and PPA based films (with odd number of carbon atoms in the side chain of the cation) exhibited a similar dense web of nanorod-like structure with pinholes and cracks on the whole surface indicating that the perovskite crystals tend to grow in one direction. These inferior morphologies for $(PMA)_2SnI_4$ and $(PPA)_2SnI_4$ showed RMS roughness values of 21.3 and 18.6 nm, respectively. The high surface roughness could be detrimental to the charge carrier transport in the channel. In contrast, a smooth film morphology with full coverage was obtained using cations with even numbers (PEA and PBA) and the surface roughness was dramatically reduced to 8.9 nm and 6.4 nm, respectively. It can be assumed that the morphological differences are due to different crystallization induced by various organic spacers.[11]

4.3 FETs performance based on phenethylammonium derivatives

To investigate the in-plane charge carrier transport in these four perovskites FETs, the FET devices with bottom-gate and top-contact configuration were fabricated where the channel length L and width W were 80 μm and 1000 μm, respectively. Figure 4.2 presents *p*-type performance of the FET devices based on $(PMA)_2SnI_4$, $(PEA)_2SnI_4$, $(PPA)_2SnI_4$ and $(PBA)_2SnI_4$, respectively. The device characteristics were measured at different temperatures during heating from 100 K to 295 K. Transfer curves were recorded at V_{DS} of - 60 V during V_{GS} scans from +60 V to -60 V. It is noteworthy that the devices based on the cations with odd numbers of carbon atoms in the alkyl chain, PMA and PPA, showed an extremely poor field effect behavior even at low temperature (Figure 4.2a and c). On the contrary, the $(PEA)_2SnI_4$

based FET device at 295 K exhibited V_{TH} of 10 V, $I_{ON/OFF}$ ratio of 1×10^4, and field-effect mobility μ of 0.33 $cm^2V^{-1}s^{-1}$ (Figure 4.2b), demonstrating similar electrical parameters to the previously reported $(PEA)_2SnI_4$ perovskite FETs (all the parameters were extracted from transfer curves in forward direction).[4] Surprisingly, with further increasing the side alkyl chain length to even number (PBA), a notable *p*-type field effect transport is observed. As shown in Figure 4.2d, the $(PBA)_2SnI_4$ perovskite FETs yielded a mobility of 0.17 $cm^2V^{-1}s^{-1}$ with V_{TH} of 15 V, and $I_{ON/OFF}$ of 9×10^3, which is comparable to $(PEA)_2SnI_4$ based perovskite FETs. The performance of the PEA and PBA based FETs was notably improved by decreasing the temperature with a higher channel current and reduced dual-sweep hysteresis. This indicates that reduction of the temperature can effectively suppress the migration of mobile ions.[12]

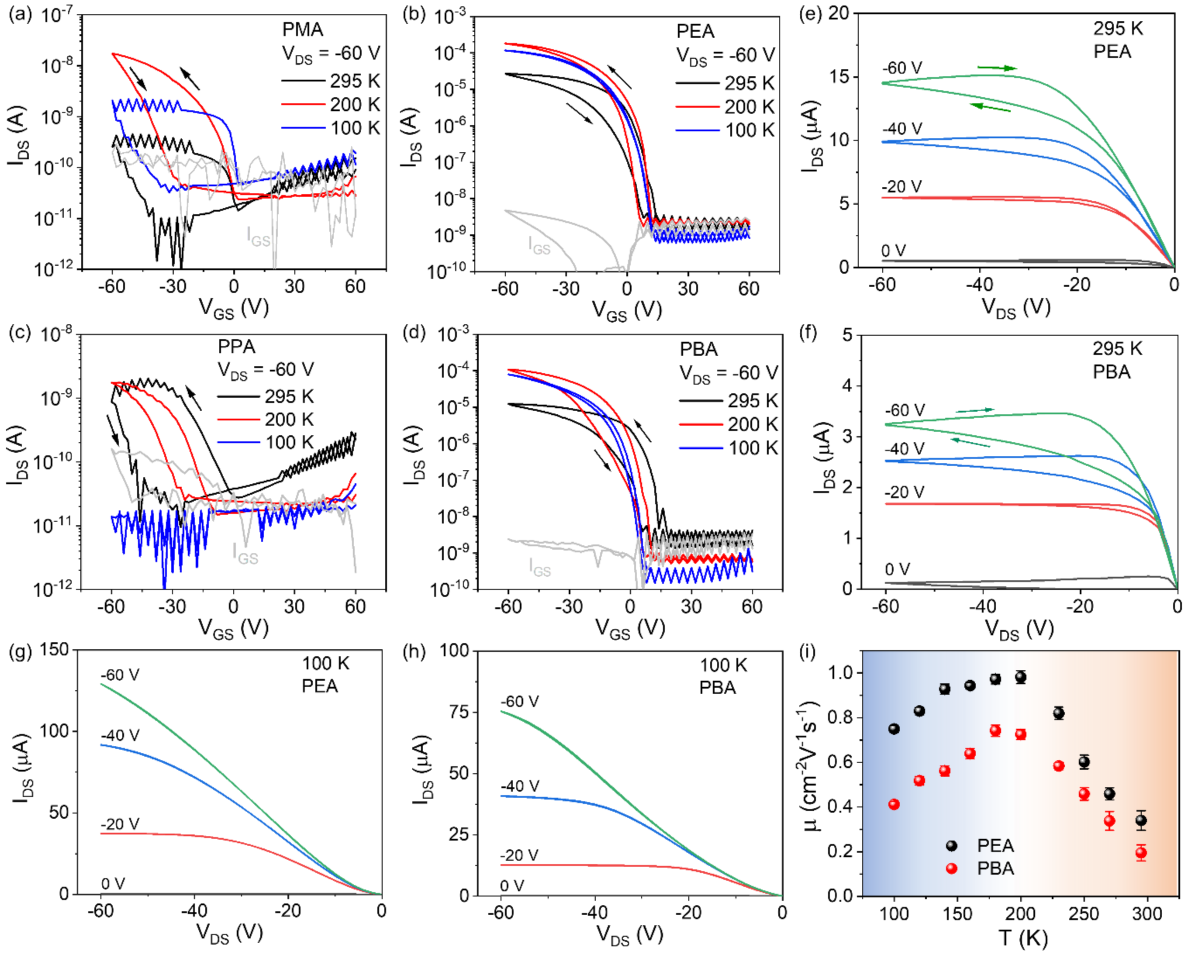

Figure 4.2. Transfer curves of perovskite FET devices based on (a) PMA, (b) PEA (c) PPA, and (d) PBA cations at three temperatures of 295 K, 200 K and 100 K, respectively.

Corresponding output curves of PEA and PBA based FET devices at (e, f) 295 K and (g, h) 100 K. (i) Temperature dependence of device mobility of PEA and PBA based FET devices.

The corresponding output characteristics at 295 K with clear linearity at low V_{DS} and current saturation at high V_{DS} were observed for both $(PEA)_2SnI_4$ and $(PBA)_2SnI_4$ FET devices (Figure 4.2e and f), indicating the negligible charge injection barriers between the perovskite films and source-drain electrodes. Interestingly, at 100 K, a sublinear region at a small V_{DS} is observed in the output curves, which manifests the contact resistance in the transistors (Figure 4.2g and h).[13] Since ion migration is not likely to account for this contact behavior because it is effectively suppressed at such low temperatures, stationary ions close to the source-drain electrodes might contribute to the remaining contact resistance.[14]

Temperature dependent measurements were performed for the range from 100 to 295 K to further elucidate the charge transport mechanism in these perovskite films based on PEA and PBA, and the resulting μ_{FET} as a function of temperature is shown in Figure 4.2i. The temperature dependent mobility plots exhibit two distinct regimes, specifically, increasing mobility from 100 K to 200 K, and decreasing mobility from 200 K to 295 K. For both $(PEA)_2SnI_4$ and $(PBA)_2SnI_4$ devices, the hole mobility reached a maximum at around 200 K. The increased charge carrier mobility at low temperature from 100 to 200 K is attributed to thermally activated charge transport mechanism.[15] In the second regime, the carrier mobility strongly decreased upon increasing temperature. The temperature dependence of the charge carrier mobility is generally considered to be closely related to the charge scattering mechanism in the semiconductors and can be analyzed by fitting a typical power law behavior as $\mu \propto T^{-\gamma}$, where γ reflects the magnitude of charge scattering.[16] The two $(PEA)_2SnI_4$ and $(PBA)_2SnI_4$ FET devices show γ values of 2.34 and 2.59 between 200 and 295 K, respectively, which indicates that the charge transport in this regime is dominated by ion migration.[17] The presence of mobile ions is likely because, in this regime, the hysteresis in the transfer characteristics is increased as the immobilized ions are activated at higher temperature.

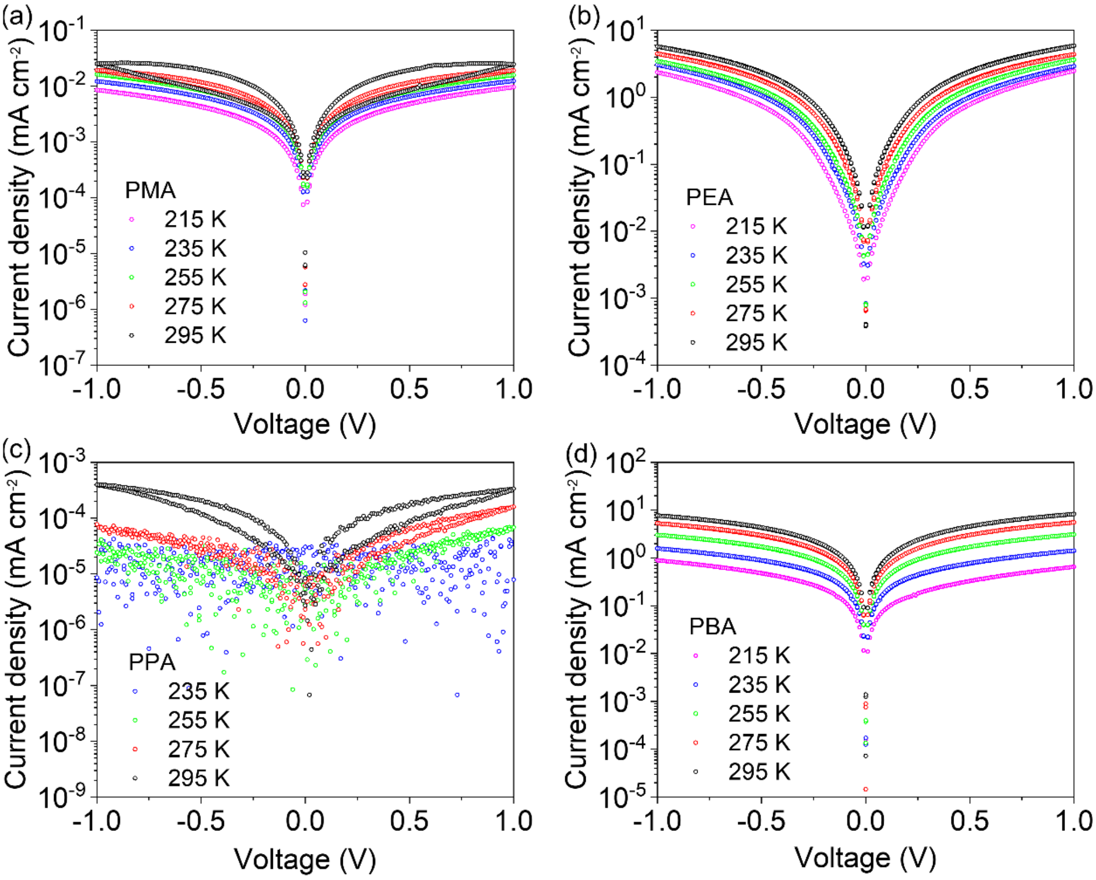

Figure 4.3. Temperature dependent current-voltage characteristics of (a) PMA, (b) PEA, (c) PPA and (d) PBA based perovskite thin films sandwiched between Au electrodes.

The charge transport in out-of-plane direction in these 2D perovskite thin films was additionally examined by temperature dependent current density-voltage characteristics as shown in Figure 4.3 for sandwich-structure devices with shadow mask-patterned top and bottom Au electrodes. Additionally, the film thickness increased to around 300 nm to minimize leakage current and obtain reliable devices. High current density and hysteresis-free current-voltage curves are observed for the devices based on PEA and PBA spacer cations. On the contrary, PMA and PPA based devices exhibit large dual-sweeping hysteresis and much lower current density, suggesting that the out-of-plane charge transport in these two films are significantly reduced, which is in line with the above discussion.

4.4 THz spectroscopy measurement

To confirm the odd-even effect observed in the FETs and to probe the local transport of charge carriers within 10s of nm, contact-free, ultrafast terahertz time-domain spectroscopy (THz-TDS) with sub-picosecond (sub-ps) time resolution was performed by Heng Zhang and Dr. Hai I. Wang. A photoexcitation with photon energy of 3.10 eV (i.e., pump) was firstly used to generate electrons and holes in the conduction and valence bands, respectively. Subsequently, a single-cycle THz probe pulse with ~1 ps duration transmits collinearly through the perovskite thin film on fused silica substrate, interacting with the photoexcited charge carriers. This interaction leads to the attenuation $\Delta E(t)$ of the incident THz electric field $E(t)$, which is related to the real part of the photoconductivity $\Delta\sigma$ ($\propto -\Delta E/E$).[18]

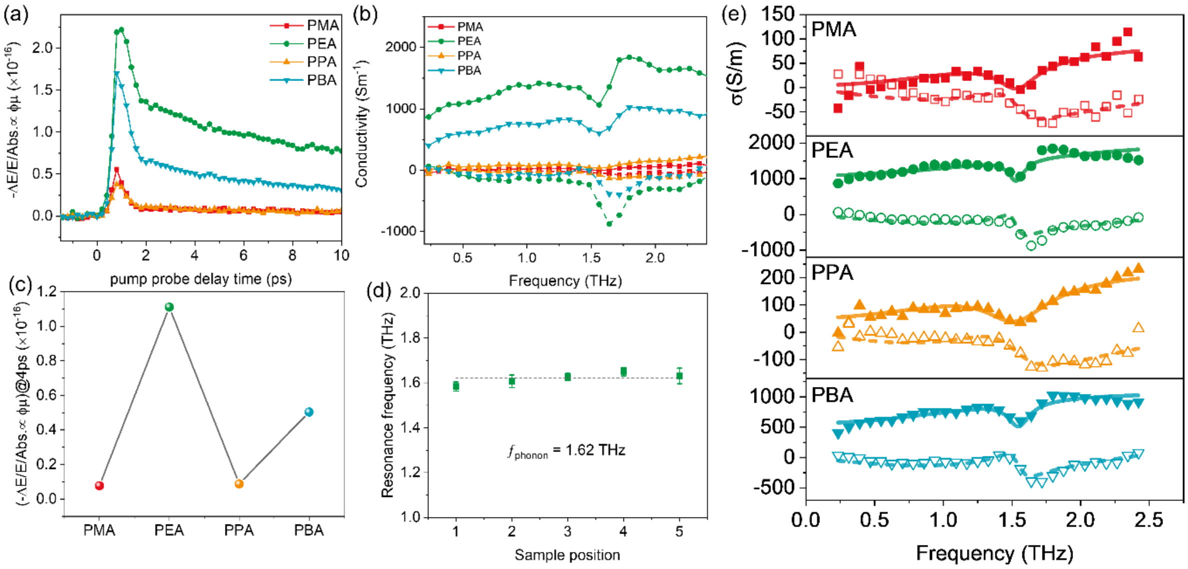

Figure 4.4. (a) Normalized OPTP dynamics pumped with photon energy of 3.1 eV, fluence of 56.3 uJ cm^{-2} at room temperature. (b) Comparison of –ΔE/E/Abs. at pump probe delay time of 4 ps. (c) Photoconductivity spectra at pump probe delay time of 4 ps. (d-e) Comparison of scattering times and parameter c, extracted from fits described in the main text.

Figure 4.4a shows the photoconductivity dynamics normalized to the absorbed photon densities (i.e., $-\Delta E/E\ /Abs. \propto \phi\mu$, with ϕ the quantum yield, μ the charge mobility) for PMA, PEA, PPA, and PBA. Though possessing similar recombination dynamics, the perovskite films exhibited distinct intensities suggesting a largely varied charge mobility (assuming a similar photon-to-carrier quantum yield). As clearly illustrated in Figure 4.4b, an enhanced charge mobility up to one order of magnitude for PEA and PBA was observed, and it showed an odd-even modulation from PMA, PEA, PPA to PBA.

To further corroborate this effect and gain more insights into the intrinsic variation in charge transport, the frequency-resolved photoconductivity spectra were recorded and are shown in Figure 4.4c for all samples at pump probe delay time of 4 ps. These spectra can be adequately described by a combined Drude-Smith model ($\Delta\sigma_{DS}$, for the free carrier response) and a Lorentz model ($\Delta\sigma_{ph}$, for the phonon mode at 1.62 THz):[19] $\Delta\sigma(\omega) = \Delta\sigma_{DS} + \Delta\sigma_{ph}$. From the fits, the scattering time τ and parameter c were obtained, which are related to the charge mobility by the formula: $\mu = \frac{e\tau}{m^*}(1 + c)$. The parameter c ($-1<c<0$) accounts for the charge backscattering effect due to e.g., the polycrystalline boundaries and lattice distortions.[20,21] When c =0, the charge carrier transport with momentum-randomizing scattering evens; when c =-1, the charge carriers are subject to a complete preferential backscattering, resulting in a charge localization. From Figure 4.4d, the scattering times keep almost the same within the errors, indicating the same intrinsic transport in all the samples. This result is in line with the preferential charge transport in the inorganic [SnI_6] sub-lattice.[22] However, the parameter c shows a large and similar odd-even variation in a same order as for the charge carrier mobility (Figure 4.4e). This result indicates that the structural change in the crystallinity or the lattice distortion gives rise to the varied charge transport properties, i.e., the odd-even variation in charge mobility.

4.5 GIWAXS characterization

In the exploration of the structure-property relationship of these 2D hybrid layered perovskites and the origin of odd-even effect in FETs, understanding their crystal structure is crucial. However, experimental determination of crystal structures for these materials has proven to be challenging. To this end, computational modeling was used to generate initial guesses for the structures of these materials. The grazing-incidence wide-angle X-ray scattering (GIWAXS) patterns were simulated (performed by Prof. Dr. Dag W. Breiby) for the generated conformers and compared to experimentally observed GIWAXS spectra (performed by Okan Yildiz) to identify the most promising candidate structures. For PMA, the crystal structure of $(PMA)_2SnI_4$ was characterized in a previous report by Mao et al.[23] This structure was used as starting point for further optimization using DFT (Figure 4.5a). The simulated GIWAXS spectra using this optimized structure showed excellent agreement with the experimentally obtained GIWAXS spectra, as depicted in Figure 4.5b and c (column 1), respectively. For PEA, two different crystal structure geometries have been reported in the literature.[24-27] Both structures were explored to simulate the GIWAXS pattern. In the simulation, the GIWAXS pattern obtained using the structure reported by Gao et al. as the initial guess demonstrated better agreement with the experimental GIWAXS spectra (column 2). [24] For the two systems with longer organic spacers, PPA and PBA, the study of Kamminga et al. on Pb-based layered hybrid perovskites with the same organic cations is referred. [28] By replacing Pb with Sn and optimizing both structures, the PPA structure (column 3) was obtained which showed the best correspondence between the simulated GIWAXS pattern and experimental GIWAXS pattern, and thus was chosen for further electronic structure analysis. However, the analogous structure for PBA cation was discarded, having both corner and face-sharing SnI_6-octahedron, based on simulated and experimental GIWAXS pattern comparison. Instead, for $(PPA)_2SnI_4$ a structure with regular corner-sharing octahedral (column 4) was proposed which showed better agreement between the simulated and experimental GIWAXS data. In addition to comparing the GIWAXS spectral pattern, the inter-inorganic layer distance ($d_{\text{int-layer}}$) was utilized as a crucial parameter for screening various DFT-computed structures. The conformers presented in the main text showed reasonable agreement between the computed and experimentally measured $d_{\text{int-layer}}$ values (experimentally obtained values are in parenthesis): 14.2 Å (14.4 Å), 16.2 Å (16.3 Å), 16.5 Å (16.7 Å), and 19.5 Å (19.6) Å for PMA through PBA-based perovskite, respectively. The consistency of the calculated and experimental $d_{\text{int-layer}}$ values further justifies the selection of these conformers as the most probable structures of the systems under consideration.

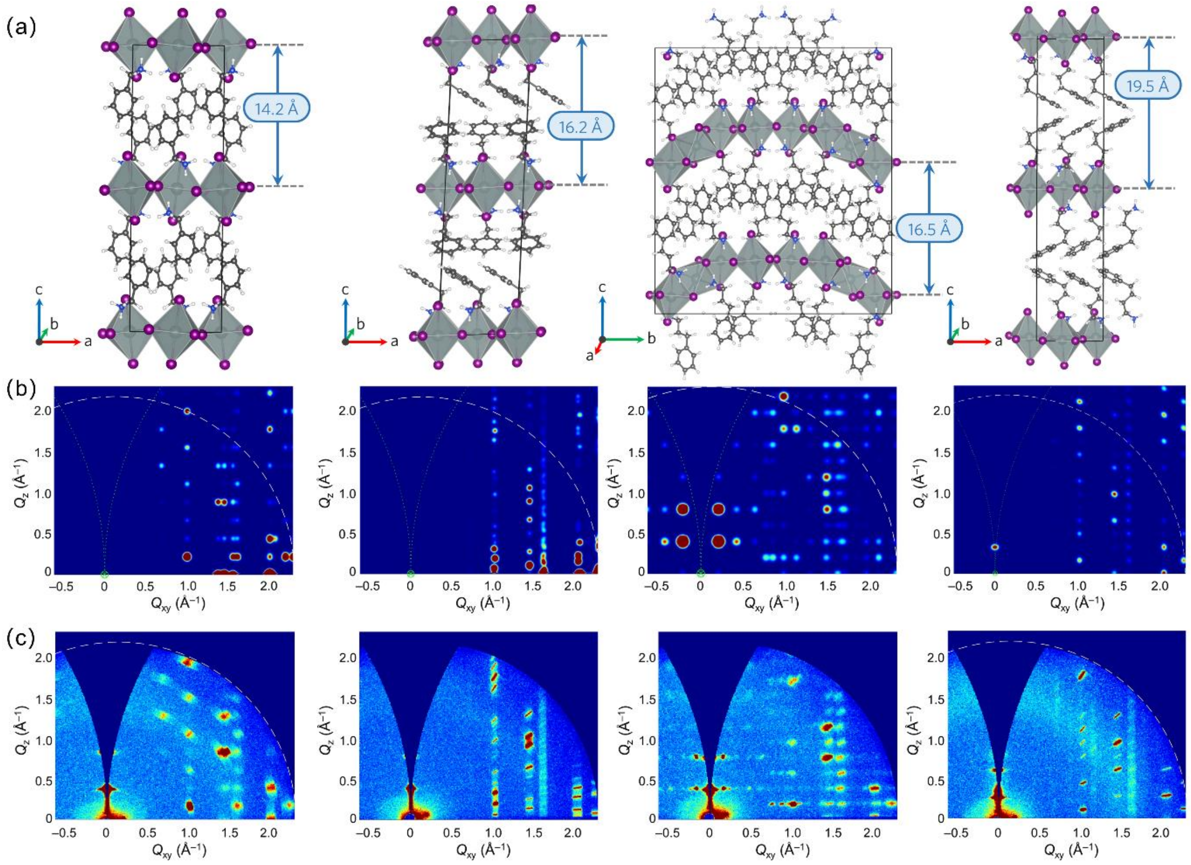

Figure 4.5. (a) Models for the four 2D perovskites. The organic spacer chain length was varied by altering the number of aliphatic carbon atoms between the phenyl ring and the NH_3^+ head group, resulting in structures named PMA to PBA. The distance between adjacent inorganic layers was also shown for each structure. (b) Simulation and (c) experimental GIWAXS patterns of the 2D perovskite structures.

4.6 DFT calculation

Next, DFT calculations were carried out by Dr. Mukunda Mandal and Dr. Denis Andrienko to investigate the influence of organic spacer length on the electronic properties of these “well/barrier” composite 2D-perovskite semiconductors. Figure 4.6 depicts the densities of states (DOS) of the four materials studied. Figure 4.6a shows the DOS contribution exclusively due to the inorganic component of the composite material, which comprises Sn and I atoms. The analysis reveals that mainly the I 5p and Sn 5s orbitals contribute to the valence band maximum VBM, while the Sn 5p and I 5p orbitals make a substantial contribution to the conduction band minimum CBM. To assess the contribution of the organic spacer alone, the partial DOS contributions due to C, H, and N atoms are plotted in Figure 4.6b. These findings show that the organic layer does not have a “direct” impact on the electronic properties of the materials, as its contribution is located away from both the VBM and the CBM. Nevertheless, it is crucial to emphasize that the organization and orientation of the organic spacers significantly affect the structural order within the inorganic sheets, eventually leading to the octahedral tilting on the inorganic $[SnI_6]^{4-}$ units. This, in turn, has a direct influence on the electronic properties of the material, which were elaborated on in subsequent sections.

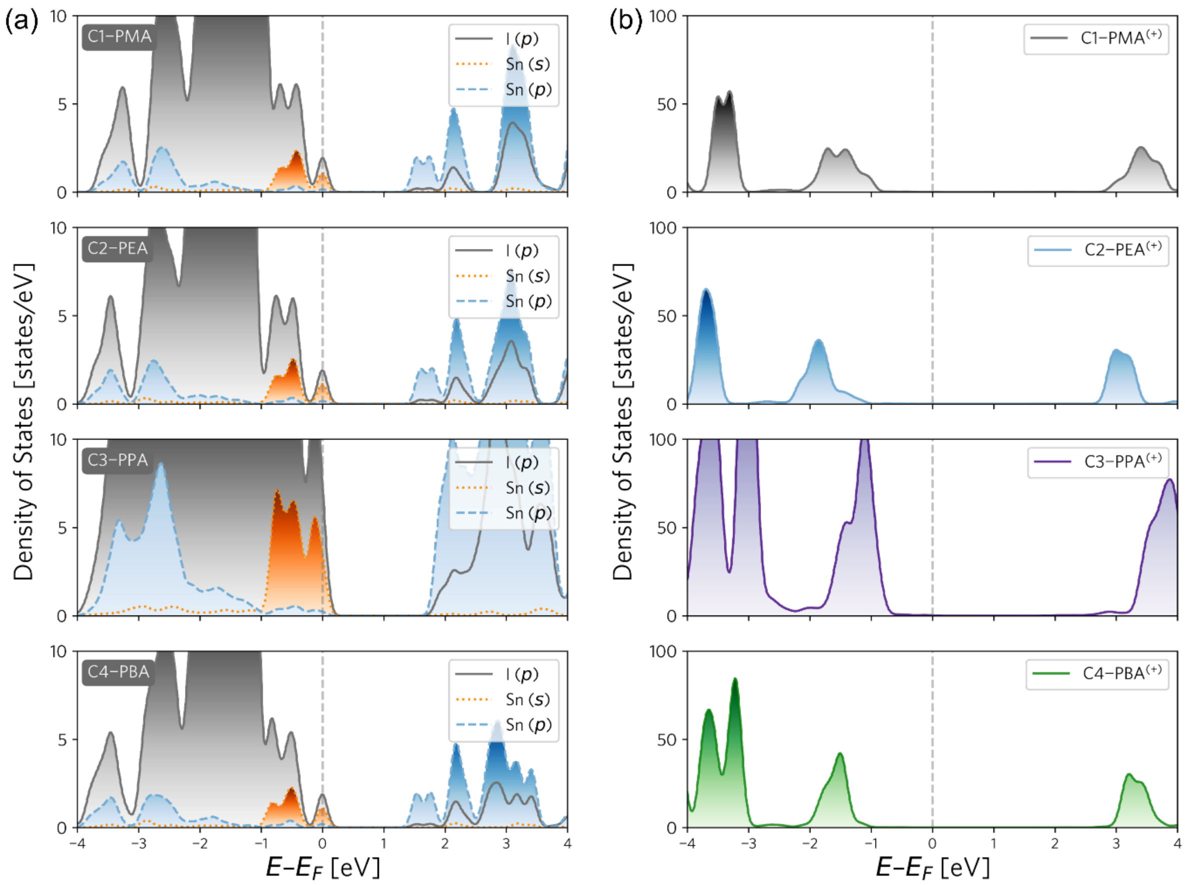

Figure 4.6. The electronic densities of states (DOS) computed using DFT are presented. (a) The DOS projected onto I(p), Sn(s), and Sn(p) orbitals in the vicinity of the VBM, which provides the DOS contribution from the inorganic layer. (b) The sum of orbital contributions from C, H, and N atoms, which provides the net DOS contribution from the organic spacer.

The electronic band structures of these four materials along high symmetry points of the first Brillouin zone are presented in Figure 4.7 a-d, which reveals that the VBM and CBM both occur at the *Γ*-point in all cases. The calculated direct band gaps for PMA to PBA are 1.19 eV, 1.26 eV, 1.82 eV, and 1.15 eV, respectively. It should be noted that the band gaps are significantly underestimated compared to experimental values (1.97 eV, 1.92 eV, 2.04 eV, 1.93 eV, respectively, for experimental values), but this is expected since GGA functional PBE was employed for the calculations.[29-31] Effective hole masses were calculated by fitting the band edges to a third-order polynomial, which revealed lower effective hole masses for PEA and PBA as compared to PMA and PPA, with values of –0.193 (Γ→Y), –0.176 (Γ→Y), –0.655 (Γ→X), and –0.157 (Γ→Y) for PMA to PBA, respectively (in the units of free electron rest mass, m_0). The larger effective hole mass of PPA indicates a lower predicted mobility, possibly due to its structural disorder as evident from Figure 4.5a (column 3) showing both corner and face-sharing octahedral in the inorganic sheet, suggesting a 1D confinement effect. On the other hand, 2D confinement is predicted for both PEA and PBA, making them good candidates for device applications. The poor performance of PMA may be attributed to structural disorder arising from octahedral tilting (vide infra). It is generally believed that charge carriers are confined in inorganic octahedral layers in 2D layered perovskite structure due to the dielectric effect. The tilted crystal structure is expected to retard the charge transport in the perovskite channel, leading to the inferior performance of FET devices.

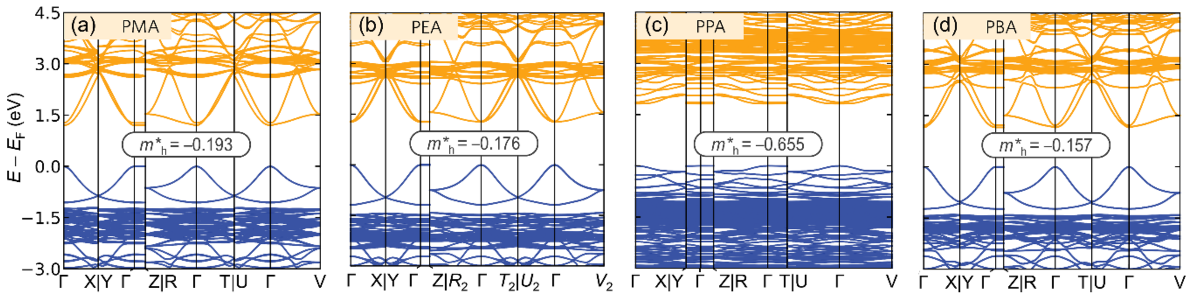

Figure 4.7. The corresponding electronic band-structure of (c) PMA, (d) PEA, (e) PPA, and (f) PBA based perovskites computed using density functional theory (DFT) is shown. The VBM is set to zero in all panels. Effective masses of holes (m_h^*) are reported in the Γ→Y direction for

all cases, except for PPA, where the value is reported in the Γ→X direction. The reported values are in the units of free electron rest mass ($m_0 = 9.11 \times 10^{-31}$ kg).

As noted previously, the presence of organic cations significantly impacts the structure of the inorganic layer. To better understand the influence of organic cations on the level of disorder within inorganic sheets, the parameter of organic cation penetration depth (d_P) is introduced following the approach of Du et al.[32] The parameter d_P measures the average distance between the plane containing the N atoms of the organic cation and the plane of the axial I atoms of the inorganic sheet (Figure 4.8a). A larger d_P value implies a stronger steric interaction between the organic cation and the inorganic framework, which leads to greater distortion of the octahedral units.[32,33] This distortion is reflected in both the in-plane distortion of the inorganic sheet, indicated by the ∠Sn–I–Sn bond angle (Figure 4.8b), and the out-of-plane distortion angle, δ (Figure 4.8c).[33]

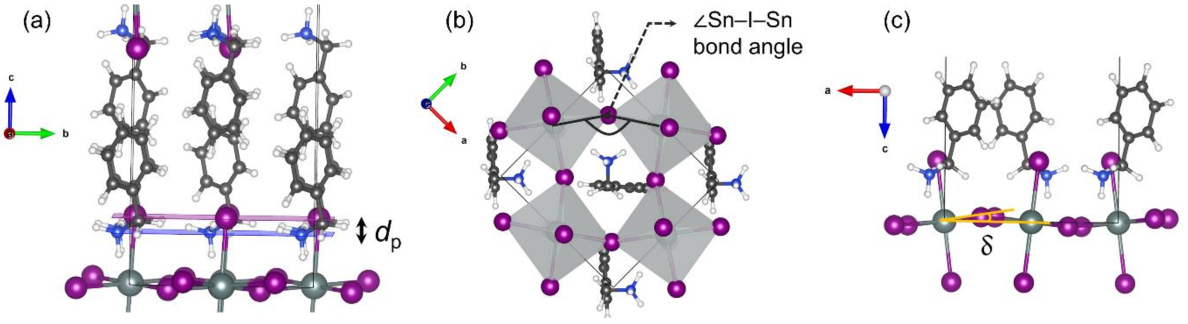

Figure 4.8. Definition of (a) organic cation penetration depth (d_P), (b) ∠Sn–I–Sn bond angle, and (c) the out-of-plane distortion angle, δ.

A slightly larger d_P value is observed for PMA than for PEA (0.71 and 0.56 Å, respectively). This difference is expected to induce more distortion within the inorganic sheets, which is confirmed by a larger out-of-plane distortion in PMA ($\delta = 7°$) compared to PEA ($\delta = 2°$). Additionally, the average ∠Sn–I–Sn bond angle is larger in PMA (~159°) than in PEA (~153°). These data support the notion that the inorganic sheet in PMA is more distorted than in the analogous PEA, leading to inferior electronic properties such as charge carrier mobility. For the longer-chained systems, the electronic properties of PBA were found to be superior to those of PPA, which can also be attributed to structural changes induced by the organic linker. As previously observed, the presence of the PPA cation leads to the formation of both corner and face-sharing octahedral in the inorganic layer, resulting in 1D confinement and hence inferior electronic properties.

4.7 Conclusion

In summary, FETs were applied to investigate the effect of molecular structure of phenylalkylammonium with various alkyl side chains as spacer cations on the charge carrier transport in 2D Sn based perovskite films. Combining with OPTP spectroscopy, GIWAXS measurement and detailed theoretical calculation. A correlation among the conformation of the organic cations, crystallinity, and the charge-carrier mobility was established. It was found that the device mobility shows odd-even effect with strong dependence on the molecular conformation of organic spacers. The presence of unique crystal structures with an inorganic framework containing face- and corner-sharing octahedra was identified for the PPA based low-dimensional perovskite. Additionally, temperature-dependent charge transport measurements on the FET devices revealed a transition from a negative mobility coefficient with dominated ion migration to a thermally activated regime at around 200 K. Taken together, This work provides a molecular level understanding of the important role of organic cation conformation in optimizing the electronic properties of 2D Perovskite FETs.

4.8 Reference

1. Q. H. Li, Y. X. Dong, G. W. Lv, T. T. Liu, D. Lu, N. Zheng, X. Y. Dong, Z. Y. Xu, Z. Q. Xie and Y. S. Liu, *ACS Energy Lett.*, 2021. **6**, 2072.
2. Y. Liu, S. G. Han, J. Q. Wang, Y. Ma, W. Q. Guo, X. Y. Huang, J. H. Luo, M. C. Hong and Z. H. Sun, *J. Am. Chem. Soc*, 2021, **143**, 2130.
3. B. Saparov and D. B. Mitzi, *Chem. Rev.*, 2016, **116**, 4558.
4. H. H. Zhu, A. Liu, K. I. Shim, J. Hong, J. W. Han and Y. Y. Noh, *Adv. Mater.*, 2020, **32**, 2002717.
5. J. Y. Go, H. H. Zhu, Y. Reo, H. Kim, A. Liu and Y. Y. Noh, *ACS Appl. Mater. Interfaces*, 2022, **14**, 9363.
6. Y. J. Reo, H. H. Zhu, J. Y. Go, K. I. Shim, A. Liu, T. Y. Zou, H. Jung, H. J. Kim, J. S. Hong, J. W. Han and Y. Y. Noh, *Chem. Mater.*, 2021, **33**, 2498.
7. T. Matsushima, S. Hwang, A. S. Sandanayaka, C. Qin, S. Terakawa, T. Fujihara, M. Yahiro and C. Adachi, *Adv. Mater.*, 2016, **28**, 10275.
8. Y. W. Guo, S. Apergi, N. Li, M. Y. Chen, C. Y. Yin, Z. C. Yuan, F. Gao, F. Y. Xie, G. Brocks, S. X. Tao and N. Zhao, *Nat. Com.*, 2021, **12**, 1.
9. Y. Takahashi, R. Obara, K. Nakagawa, M. Nakano, J. Y. Tokita and T. Inabe, *Chem. Mater.*, 2007, **19**, 6312.
10. P. H. Denis, M. Mertens, W. T. V. Gompel, K. V. Hecke, B. Ruttens, J. D’Haen, L. Lutsen and D. Vanderzande, *Chem. Mater.*, 2021, **33**, 5177.
11. S., Sánchez, L. Pfeifer, N. Vlachopoulos and A. Hagfeldt, *Chem. Soc. Rev.*, 2021, **50**, 7108.
12. Y. Lin, Y. Bai, Y. J. Fang, Q. Wang, Y. H. Deng and J. S. Huang, *ACS Energy Lett.*, 2017, **2**, 1571.
13. X. J. She, C. Chen, G. Divitini, B. D. Zhao, Y. Li, J. Z. Wang, J. F. Orri, L. S. Cui, W. D. Xu, J. Peng, S. Wang, A. Sadhanala and H. Sirringhaus, *Nat. Electron.*, 2020, **3**, 694.
14. F. J. Liu, L. Wang, J. W. Wang, F. Wang, Y. Y. Chen, S. Zhang, H. J. Sun, J. Liu, G. T. Wang, Y. Y. Hu and C. Jiang, *Adv. Funct. Mater.*, 2020, **31**, 2005662.
15. C. H. Lin, T. Y. Li, B. Cheng, C. X. Liu, C. W. Yang, J. J. Ke, T. C. Wei, L. J. Li, A. Fratalocchi and J. H. He, *Nano Energy*, 2018, **53**, 817.

16. S. P. Senanayak, B. Yang, T. H. Thomas, N. Giesbrecht, W. Huang, E. Gann, B. Nair, K. Goedel, S. Guha, X. Moya, C. R. McNeill, P. Docampo, A. Sadhanala, R. H. Friend and H. Sirringhaus, *Sci. Adv.*, 2017, **3**, 1601935.
17. Y. Liu, P. A. Chen, X. X. Qiu, J. Guo, J. N. Xia, H. Wei, H. H. Xie, S. J. Hou, M. He, X. Wang, Z. B. Zeng, L. Jiang, L. Liao and Y. Y. Hu, *iScience*, 2022, **25**, 104109.
18. R. Ulbricht, E. Hendry, J. Shan, T. F. Heinz and M. Bonn, *Rev. Mod. Phys.*, 2011, **83**, 543.
19. D. M. Zhao, H. W. Hu, R. Haselsberger, R. A. Marcus, M. E. Michel-Beyerle, Y. M. Lam, J. X. Zhu, C. La-o-vorakiat, M. C. Beard and E. E. M. Chia, *ACS Nano*, 2019, **13**, 8826.
20. X. Ai, M. C. Beard, K. P. Knutsen, S. E. Shaheen, G. Rumbles and R. J. Ellingson, *J. Phys. Chem. B*, 2006, **110**, 25462.
21. P. D. Cunningham and L. M. Hayden, *J. Phys. Chem. C*, 2008, **112**, 7928.
22. A. A. O. El-Ballouli, O. M. Bakr and O. F. Mohammed, *J. Phys. Chem. Lett.*, 2020, **11**, 5705.
23. L. Mao, H. Tsai, W. Nie, L. Ma, J. Im, C. C. Stoumpos, C. D. Malliakas, F. Hao, M. R. Wasielewski, A. D. Mohite and M. G. Kanatzidis, *Chem. Mater.*, 2016, **28**, 7781.
24. Y. Gao, Z. Wei, P. Yoo, E. Shi, M. Zeller, C. Zhu, P. Liao and L. T. Dou, *J. Am. Chem. Soc*, 2019, **141**, 15577.
25. E. I. Marchenko, S. A. Fateev, A. A. Petrov, V. V. Korolev, A. Mitrofanov, A. V. Petrov, E. A. Goodilin and A. B. Tarasov, *Chem. Mater.*, 2020, **32**, 7383.
26. G. C. Papavassiliou, I. Koutselas, A. Terzis and M. H. Whangbo, *Solid State Commun.*, 1994, **91**, 695.
27. Y. Takahashi, R. Obara, K. Nakagawa, M. Nakano, J. Tokita and T. Inabe, *Chem. Mater.*, 2007, **19**, 6312.
28. M. E. Kamminga, H. H. Fang, M. R. Filip, F. Giustino, J. Baas, G. R. Blake, M. A. Loi and T. T. M. Palstra, *Chem. Mater.*, 2016, **28**, 4554.
29. P. Mori-Sánchez, A. J. Cohen and W. Yang, *Phys. Rev. Lett.*, 2008, **100**, 146401.
30. H. Yuce, M. Mandal, Y. Yalcinkaya, D. Andrienko and M. M. Demir, *J. Phys. Chem. C*, 2022, **126**, 11277.

31. J. M. Crowley, J. Tahir-Kheli and W. A. Goddard, *J. Phys. Chem. Lett.*, 2015, **6**, 3792.

32. K. Z. Du, Q. Tu, X. Zhang, Q. Han, J. Liu, S. Zauscher and D. B. Mitzi, *Inorg. Chem.*, 2017, **56**, 9291.

33. M. Dyksik, H. Duim, X. Zhu, Z. Yang, M. Gen, Y. Kohama, S. Adjokatse, D. K. Maude, M. A. Loi, D. A. Egger, M. Baranowski and P. Plochocka, *ACS Energy Lett.*, 2020, **5**, 3609.

Chapter 5 Conclusions

The operation of perovskite FETs is complicated due to their mixed ionic-electronic conducting nature and the presence of traps and defects, as well as external factors such as oxygen, water, and light. The influence of all these factors, renders perovskites not very prospective as a semiconducting channel layer for high-performance FET devices. Although some advances have been made in recent years, perovskite FETs still need to overcome several challenges to reach the level of maturity and penetrate the commercial markets. To date, most of the reports for perovskite FETs suffers from non-ideal current-voltage characteristics and large dual-sweeping hysteresis. Therefore, understanding the origin of these phenomena and developing the corresponding strategies for suppression remain an important priority for perovskite FETs. The requirement of overall improved device performance, accompanied by the increase in mobility, the inhibition of hysteresis, and even the device stability, for commercialization, calls for the significantly more research in this field.

In this thesis, 2D tin halide perovskites were employed for the FET applications. 2D tin halide perovskites not only provide a barrier towards ion migration, but also endow effective field-effect modulation in FET devices by suppression of high hole concentration in the presence of non-conducting organic spacer cations. In order to understand the crystallization process and charge carrier transport properties 2D tin halide perovskite FETs, different approaches, including grain engineering, additive engineering and molecular engineering were designed. The correlation of chemical structure of spacer cations, film morphology, crystallinity, molecular orientation, and carrier mobility were well established. Hence, the coalition of all these factors strongly backs the use of 2D tin halide perovskite as a significant and effective approach to modulate electronic properties of FETs. The main conclusions are conceived and summarized as follows:

1. One of the main obstacles in achieving a reliable operation of perovskite transistors at room temperature is severe ion migration, which can screen the applied gate field,

resulting in poor field-effect behavior and large dual-sweeping hysteresis. Hot-casting method has been employed to regulate the crystallization and growth kinetics of 2D perovskite $(TEA)_2SnI_4$ to understand the charge transport properties and reveal the role of grain boundaries in perovskite FETs, as presented in Chapter 2. By tailoring the substrate temperature, the grain size substantially increased but with not much enhancement in the crystallinity and orientation THz spectroscopy transient absorption measurement confirmed the above results since the local charge carrier mobility and excited state dynamics were found to increase moderately.

However, in contrast, the FET operation parameters, including mobility, threshold voltage, hysteresis, and subthreshold swing improved drastically with larger grain size. In this regard, grain boundaries can be viewed as trap centers for charge carrier transport and pathway for ion migration. Therefore, reducing the number of grain boundaries is believed to be an efficient way to increase the gate modulation of the electronic current and consequently the FET performance.

2. In order to further enhance the charge mobility in FETs, the limitation of 2D tin halide perovskite concerning the oxidation issue of Sn^{2+} should be addressed to minimize the defects in the film. Molecular interactions play a fundamental role in material science to induce material functionality. Rationally designed molecules were employed to precisely trigger non-covalent interactions and direct self-assembly of the building blocks resulting in desired properties of the bulk material. This approach can be adapted to hybrid perovskite semiconductors that suffer from fast crystallization, easy oxidation, inferior film morphologies and high charge trap density limiting their application in FETs. Chapter 3 described the impact of additive on device performance of 2D $(TEA)_2SnI_4$ perovskite FETs. A simple and an effective additive engineering strategy using small molecule PA were introduced to both modulate crystallization process and improve charge carrier transport in $(TEA)_2SnI_4$ perovskite FETs.

Combine with various characterizations, it was revealed that PA with carboxylic group is strongly coordinated to the cation TEAI and $[SnI_6]^{4-}$ framework in perovskite precursor solution, inducing heterogeneous nucleation and lowering undesired oxidation of Sn^{2+} during the film formation. These factors contributed to the reduced defects by suppression of generating ionic defects Sn^{4+}, improved film morphology including lower surface roughness and larger grain size. On the basis of these findings, the overall enhanced transistor characteristic was achieved in the presence of reduced defects and decreased ion migration.

3. In order to unveil the impact of chemical tuning of organic cations on the electronic properties of 2D tin halide perovskite FETs, the effects of the spacer on the structure, properties, and device performance requires to be systematic investigated. It is generally believed that the best possible way to tailor photophysical properties of low-dimensional perovskites is to structurally maneuver organic ligands. This opens-up a plethora of opportunities for synthetic chemists to explore different possibilities to diversely engineer and functionalize organic cations for tailoring and developing perovskites FET. In Chapter 4, a molecular engineering was proposed to understand the influence of the molecular structure of cation spacers on in-plane charge carrier transport in 2D tin halide perovskite FETs, by employing four cations with different alkyl chain lengths.

A strong change of in-plane mobility in FET devices, depending on whether the carbon atoms on alkyl side chain was of odd or even number, was observed. Combining experimental characterization and theoretical simulation, it showed that a subtle change in molecular structure of organic cation has a significant impact on the molecular conformation, film morphology, as well as the charge transport in perovskite film.

This thesis has revealed the correlation of crystallization, thin film morphology, molecular orientation, and charge transport properties, as well as the device performance of 2D tin halide perovskite FET, fueled by a better understanding of the parameters from the materials properties to device physics, suggesting that perovskite FETs might be able to catch up with the other perovskite optoelectronic devices and become contenders for practical applications. Nevertheless, still, many challenges remain to be addressed, in particular, issues related to field-effect mobility and device stability.

Owing to their intrinsic ionic defects, perovskites most likely attain the low mobilities compared to their local or intrinsic mobility by THz characterization, and also other semiconductors like crystalline silicon, or organic materials. However, a high mobility is indeed necessary in order to achieve commercialization, but it is by no means sufficient. Other device parameters, such as the operating voltage, channel length and source/drain electrodes, are also critical and should be accounted into the overall performance in perovskite FETs. The stability of perovskite FETs in different environments is the second biggest problem, which requires more efforts to tackle this key challenge in the future.

Chapter 6 Experimental appendix

6.1 Materials

The organic salts Phenylmethylammonium iodide (PMAI), Phenethylammonium iodide (PEAI), Phenylpropylammonium iodide (PPAI) and Phenylbutanammonium iodide (PBAI) were all ordered from Xi'An Polymer Light Technology Corp (Xi'An, China). Pentanoic acid solution (CAS Number: 109-52-4), Formamidinium iodide (FAI), Tin (II) iodide (SnI_2, 99.999%), N,N-Dimethylformamide (DMF, anhydrous, 99.8%), Dimethyl sulfoxide (DMSO, anhydrous, ≥99.9%) were purchased from Sigma-Aldrich. All chemical reagents and solvents were used without further purification. Heavily doped silicon wafers were obtained from Ossila Ltd.

In Chapter 2, the organic spacer TEAI was synthesed by Sabine Frisch, and Dr. Milan Kivala at the Organisch-Chemisches Institut, Centre for Advanced Materials, Ruprecht-Karls-Universität Heidelberg.

6.2 Substrate preparation

The heavily p-doped bare Si wafers (1.5 × 2 cm) with a 300 nm thick SiO_2 layer were used as the substrates and cleaned in an ultrasonic bath by deionized water, acetone, and isopropyl alcohol and then blown dry with N_2. The substrates were treated by oxygen plasma for 3 min and then transferred into a glove box for the perovskite film deposition.

6.3 Precursor solution preparation

In Chapter 2, the 2D perovskite $(TEA)_2SnI_4$ precursor solution with the concentration of 0.1 M was prepared in a stoichiometric ratio of TEAI and SnI_2 (2:1) by dissolving TEAI and SnI_2 in mixed DMF/DMSO solvent (1:1). The solution was stirred overnight at 60 °C in a glove box and cooled to room temperature before use.

In Chapter 3, the precursor solution was obtained by mixing the precursor materials TEAI and SnI_2 at a molar ratio of 2:1 in DMF at 0.1 M concentration. For the PA-incorporated

$(TEA)_2SnI_4$ precursor, 0.25, 0.5, 0.75, and 1 vol % of PA were added to pristine $(TEA)_2SnI_4$ solution. The solution then was stirred overnight at 60 °C in a glovebox and cooled to room temperature before use.

In Chapter 4, the perovskite precursor solution with the concentration of 0.15 M was prepared by dissolving the organic cations (PMAI, PEAI, PPAI, PBAI) and SnI_2, with standard molar ratio of 2:1 in mixed DMF/DMSO (1:1) and kept stirring overnight at room temperature in N_2 glovebox before use.

6.4 Film and device fabrication

During spin-coating, the substrate was transferred to the spin coater chuck and the spin coating process was immediately started when the solution was drop casted onto the substrate in the glovebox (Figure 6.1). All the as-prepared fresh precursor solution was spin-coated with a 0.2 μm polytetrafluorethylene (PTFE) filter at 4000 rpm for 60 s and annealed at 100 °C for 10 or 30 min. Finally, the source and drain electrodes were deposited with the thickness of 80 nm by gold thermal evaporation through a shadow mask (from Ossila) to construct L × 1000 μm (length × width) transistor channels with various L value (10, 30, 50, and 80 μm).

In Chapter 4, for temperature dependent current-voltage characteristics of measurement, the devices with sandwich structure of Au/Perovskite/Au were fabricated by using shadow mask-patterned electrode based on the above-mentioned fabrication procedure accordingly. Thicker perovskite films with the thickness more than 300 nm were employed to minimize leakage current. All electrical measurements were performed inside a nitrogen-filled glovebox with a Keithley 2400 source meter.

Figure 6.1. (a) Glovebox system for perovskite thin film preparation.

6.5 Film characterizations

6.5.1 Abs and PL spectra

The optical absorption spectra of perovskite films were measured using an ultraviolet/visible (UV/Vis) spectrophotometer from a PerkinElmer Lamda 900 instrument with an all-reflecting, double-monochromator optical system and holographic gratings used in each monochromator for the UV-vis range (Figure 6.2). Data was collected from 300 - 800 nm using a dwell time of 0.1 s. During all measurements, the samples were kept in air and at room temperature. The PL spectra were recorded with a HORIBA Jobin-Yvon Fluorolog 3-22 Tau-3 using a photomultiplier tube (PMT) as detector and FluorEssence (version 3.9.0.1; Origin version 8.6001) as software (Figure 6.3). Photoluminescence quantum yield was measured using the aforementioned Fluorolog-3 with an integrating sphere (F-3018 from Horiba Jobin Yvon) under nitrogen flow to avoid the degradation of perovskite samples.

Figure 6.2. Perkin Elmer Lambda 900 UV/Vis/NIR spectrometer.

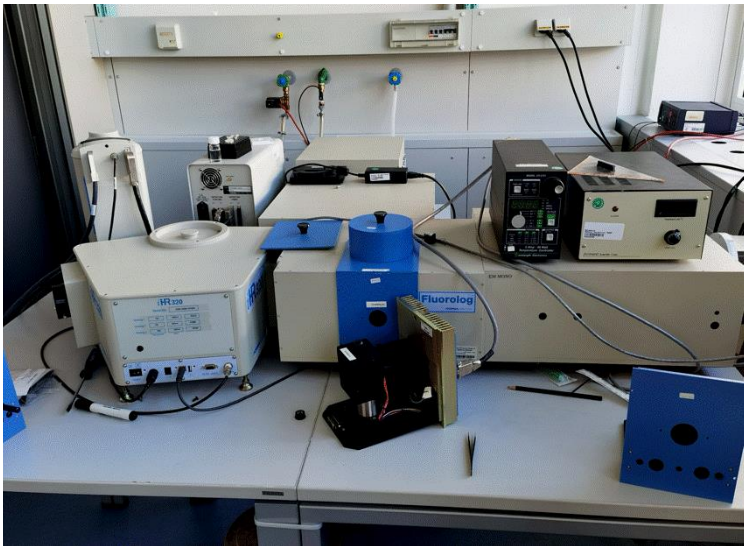

Figure 6.3. HORIBA Jobin-Yvon Fluorolog 3–22 Tau-3

6.5.2 Transient absorption

Transient absorption spectroscopy was measured using a Helios-Fire pump-probe setup (Ultrafast Systems) (Figure 6.4). This was paired with a regeneratively amplified 1030 nm laser (Light Conversion Pharos, 200 fs, 200 uJ), set at an effective repetition rate of 1 kHz via an internal pulse picker. A small portion (20%) of the 1030 nm fundamental was directed to an optical delay line, and, subsequently, to a sapphire crystal to generate the broadband probe light.

The remaining 80% of the 1030 nm fundamental was directed to an optical parametric amplifier (Light Conversion, Orpheus-F) to generate the pump pulse at 529 nm. Global analysis of TA data was done using the R-package TIMP software, with the graphical interface Glotaran 1.5.1.

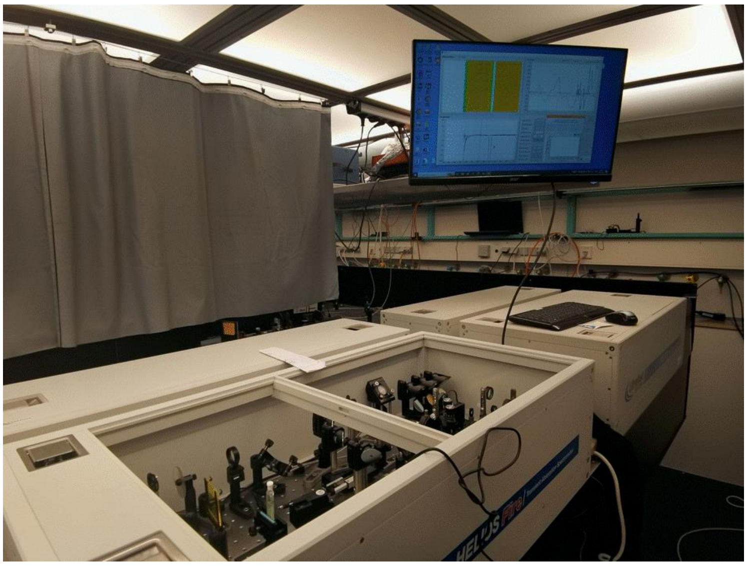

Figure 6.4. Helios-Fire pump-probe ultrafast systems.

6.5.3 XPS and UPS pattern

XPS measurements were conducted by using a PHI 5500 Multi-technique System with a base pressure of ~10^{-9} torr. The X-ray radiation was Al Kα emission (1486.7 eV; take-off angle, 75°). For UPS characterization, to avoid any charging during the measurement, Si wafers were coated with Cr/Au (2 nm/80 nm) as conductive layer by thermal evaporation. Then samples were transferred into the UPS chamber and measurements were carried out at a base pressure of 10^{-9} mbar. UPS measurements were conducted with a Kratos Axis Ultra^{DLD} spectrometer (Kratos, Manchester, England). Illumination at 21.22 eV was provided by the He(I) emission line from a helium discharge lamp. Photoelectron emission was collected at 0° from the surface normal of the samples. The spectra were taken in three different spots to confirm the spectra are producibility and irradiation exposure time was kept under one minute.

6.5.4 Film morphology

The thin film morphology was characterized by a Leica POM at room temperature (Figure 6.5). The grain size statistics are determined by Gwyddion software 15 grains in different areas for the perovskite thin film with each hot-casting temperature.

Figure 6.5. Leica polarized optical microscope.

The AFM measurements were performed using by a Bruker Dimension Icon FS at room temperature (Figure 6.6). The perovskite films were fabricated on the silicon substrate. The surface topographical images were obtained in tapping mode using a silicon tip at a resonant frequency of 300 kHz and a spring constant of 26 N/m. The root mean square (RMS) roughness values were extracted from an image of 10 μm × 10 μm.

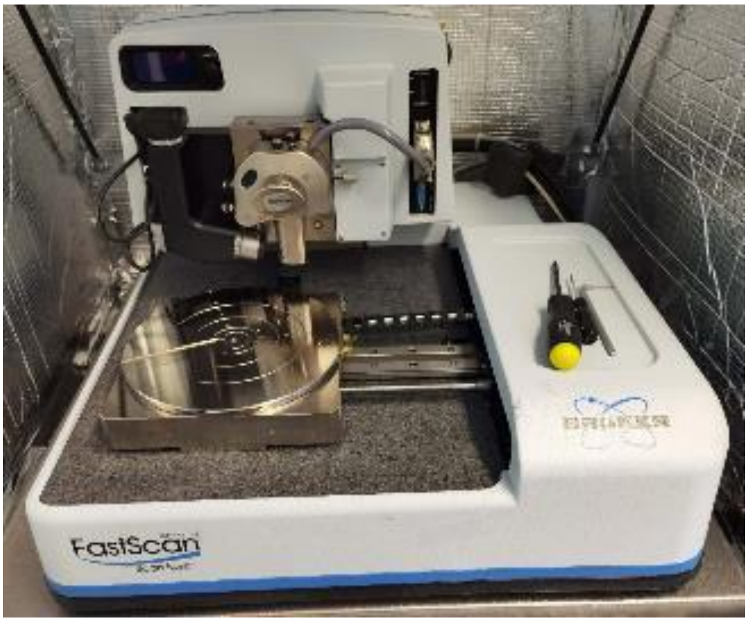

Figure 6.6. Dimension Icon fast scanning atomic force microscope.

6.5.5 Film thickness

The thickness of $(TEA)_2SnI_4$ perovskite thin film on silicon wafer was measured by a Bruker Tencor Profilometer (Figure 6.7).

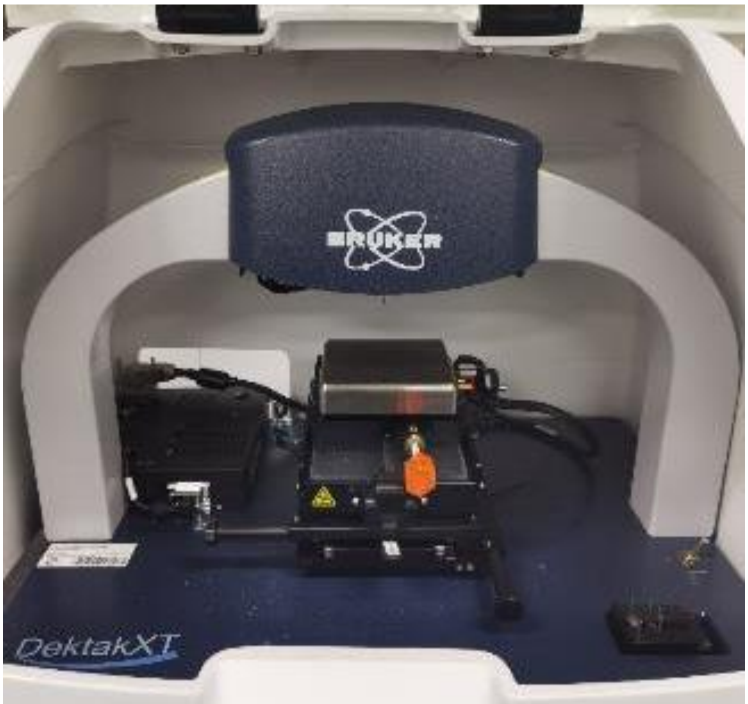

Figure 6.7. Bruker Tencor Profiler.

6.5.6 Molecular organization

The one-dimensional X-ray diffraction patterns of the 2D perovskite thin films were recorded in the 2θ between 3° and 40°, with a step of 0.01° and a speed of 10 degrees per minute, using a Rigaku SmartLab HR-XRD equipment with Cu Kα (λ = 1.5406 Å) radiation (Figure 6.8). The interlayer distance was calculated by Bragg's law $2d\sin\theta = n\lambda$.

Figure 6.8. XRD of Rigaku D/MAX 2600 V

GIWAXS measurements were performed by means of a solid anode X-ray tube (Siemens Kristalloflex X-ray source, copper anode X-ray tube operated at 35 kV and 20 mA), Osmic confocal MaxFlux optics, X-ray beam with pinhole collimation, and a MAR345 image plate detector (Figure 6.9). The beam size was 1.0 × 0.2 mm^2 (width × height), and the samples were irradiated just below the critical angle for total reflection with respect to the incoming X-ray beam (~0.1°). The scattering intensity was detected on a two-dimensional image plate (MAR-345) with a pixel size of 150 μm (2300 × 2300 pixels), and the detector was placed 523 mm from the sample center. All X-ray scattering measurements were performed under vacuum (~1 mbar) to reduce air scattering and beam damage to the sample and degradation of perovskite materials. All data processing and analysis were performed using the software package Data squeeze.

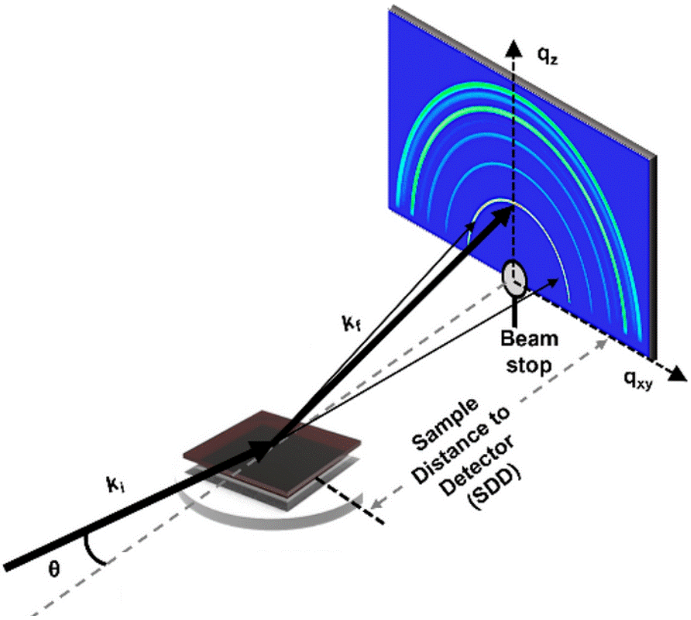

Figure 6.9. Schematic of the GIWAXS for thin-film measurement.

6.5.7 Optical-pump THz-probe spectroscopy

The OPTP setup was driven by a commercial, regenerative amplified, mode-locked Ti:sapphire femtosecond laser with a 1 kHz repetition rate. The pulse duration was around 50 fs, and the central wavelength was ~ 800 nm. A single-cycle THz pulse was generated by optical rectification on a 1 mm thick ZnTe crystal. The THz electrical field was probed in the time domain with an 800 nm sampling pulse using the electro-optic effect in a second ZnTe crystal, by varying the time delay between THz and sampling beam with an optical delay stage. For the pump-probe measurements, excitation by 400 nm light pulse was used. It was produced by second harmonic generation based on 800 nm light by beta barium borate (BBO) crystal. The pump-probe delay was controlled by a second optical delay stage. The photoconductivity ($\sigma(t_p)$) dynamics was monitored by probing the relative change in the peak field of the THz pulse ($-\Delta E(t_p)/E_0$) induced by photoexcitation, thanks to the linear proportionality of these two quantities within the thin-film approximation:[1]

$$\sigma(t_p) = -\frac{(n_1+n_2)}{Z_0 \cdot l} \cdot \frac{\Delta E(t_p)}{E_0} \qquad \text{(Equation 6.1)}$$

Here, $\Delta E(t_p) = E_{pump}(t_p) - E_0$ is the pump-induced THz electric field changes, and t_p is the pump-probe delay. n_1 and n_2 are the refractive indices of the media before and after the sample (in our work, n_1 and n_2 are 1 and 1.95 for vacuum and fused silica, respectively), $Z_0 = 377\ \Omega$ is the impedance of free space, $l = 50\ nm$ is the film thickness.

Frequency-domain photoconductivity spectra

The frequency-domain photoconductivity spectra were obtained at a specific pump-probe delay time by Fourier transforming the complete time-domain $\Delta E(t)$ and $E_0(t)$ (where t represents the sampling-probe delay time) into frequency-domain $\Delta E(\omega)$ and $E_0(\omega)$, and applying thin film approximation as in OPTP measurement:

$$\sigma(\omega) = -\frac{(n_1+n_2)}{Z_0 \cdot l} \cdot \frac{\Delta E(\omega)}{E_0(\omega)} \qquad \text{(Equation 6.2)}$$

In the study, the time-domain data was collected at 3 ps after photoexcitation by simultaneously moving the pump and sampling stage.

6.6 NMR spectra

In Chapter 2, the NMR spectra were recorded with the NMR spectrometer Bruker Avance 300 (Bruker, 300 MHz for ^{1}H and 76 MHz for ^{13}C) at room temperature. Chemical shifts (*δ*) were reported in parts per million (ppm) and were referenced to the residual solvent signal as an internal reference (($(CD_3)_2SO$: 2.50 ppm for ^{1}H, 39.5 ppm for ^{13}C). Coupling constants (*J*) were given in Hz and the apparent resonance multiplicity is reported as s (singlet), br s (broad singlet), dd (doublet of doublets), or m (multiplet). Elemental analysis was carried on a Vario MICRO cube (Elementar).

In Chapter 3, the solution NMR experiments were performed on a Bruker Avance 400 MHz spectrometer equipped with a BBI probehead with z-gradients. ^{1}H spectra were acquired using 32 scans and a recycle delay of 2 s. ^{119}Sn spectra were acquired using 256 scans and a recycle delay of 10 s. DMSO-d_6 from the company Deutero GmbH was used as solvent without further purification. All NMR experiments were performed under ambient conditions.

6.7 Impedance spectroscopy

In Chapter 2, the impedance measurements were performed with the FET configuration by connecting source and drain electrodes using a computer-controlled Solartron impedance analyzer under ac voltage of 100 mV in a vacuum chamber.

6.8 Perovskite FETs characterization

The device characterization was performed using a semiconductor parameter analyzer (Keithley 4200-SCS) in a low-temperature probe station (Figure 6.10). The temperature-dependent measurements were performed using a Desert Cryogenics low-temperature probe station. The transfer characteristics were collected in pulse mode, and the output characteristics were measured in continuous mode. In the pulse mode, V_{GS} was applied over a short impulse of 1 s.

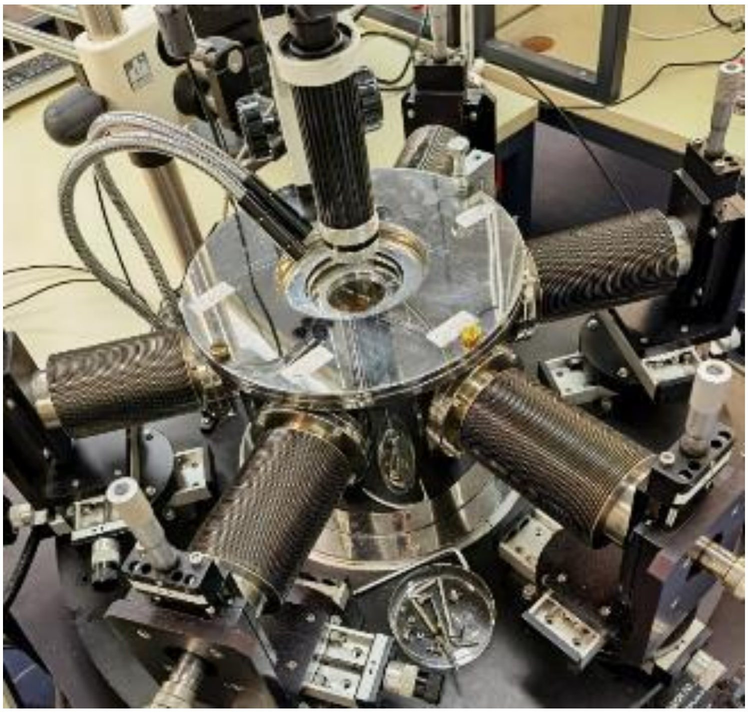

Figure 6.10. Probe station for contacting the devices under vacuum and low temperature.

6.9 Kelvin probe force microscopy

Mapping of the FET potential distribution was performed via KPFM, using an Asylum Research MFP3D Microscope (Oxford Instruments) together with a lock-in amplifier (HF2LI-MOD, Zurich Instruments). To avoid degradation of the perovskite film, the setup is placed in an argon filled glovebox with atmosphere containing less than 1 ppm O_2 and minimal humidity. Our sample holder allows to establish an electrical connection to the source, drain and gate electrodes and ground them, or apply direct current voltages to them individually. To control the source and drain electrode voltages, we used the auxiliary output channels of the HF2 lock-in amplifier and applied a maximum voltage of 9 V (Figure 6.11). To generate the gate voltage, we used a 44 V battery stack. For the KPFM measurement we used Pt-Ir metal coated cantilevers (Bruker, SCM-PIT-V2), with resonance frequency $\omega_0 \sim 75$ Hz and spring constant ~ 3 N/m. The scan rate of the measurements was 0.2 Hz. To obtain reliable data, frequency modulation KPFM was employed, in the heterodyne configuration, whereby the cantilever is mechanically excited at its first resonance, ω_0, and electrically excited with an amplitude of 1V at its second resonance minus the first (ω_1-ω_0).[2] Frequency mixing between the mechanical motion and the periodic electrostatic force generate a sideband signal on the second resonance frequency, ω_1, that we use as input signal for the KPFM feedback.

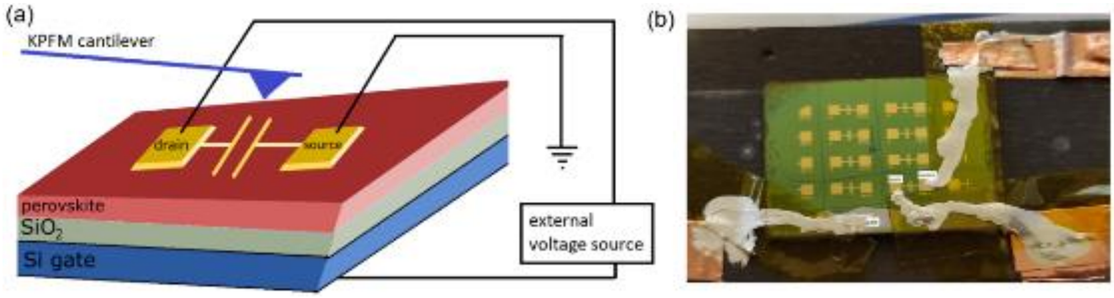

Figure 6.11. (a)Schematic representation of KPFM experiment and (b) image of experimental setup. The connections with the relevant electrodes were established with silver paste and copper tape.

6.10 DFT calculation

The computational methodology employed in this study involved first-principles calculations based on density functional theory (DFT) implemented in Vienna Ab-initio Simulation Package (VASP, version 6.3.1).[3] The calculations utilized the generalized gradient approximation (GGA) in the Perdew–Burke–Ernzerhof (PBE) functional form and incorporated Van der Waals interactions via Grimme's D3 method.[4] The projector augmented wave (PAW) method was utilized to describe valence-core interactions.[5] The calculations considered the following numbers of valence electrons for each atom type: Sn (14), I (7), C (4), H (1), N (5). A plane-wave energy cutoff of 520 eV was employed for all calculations. During geometry relaxation, forces of each atom below 0.01 eV/Å were used. The structural relaxation was carried out by sampling the Brillouin zone on a 4 × 4 × 1 *k*-mesh and a 5 × 5 × 1 *k*-mesh was used to calculate the density of states (DOS). To address the underestimation of semiconductor band gaps by DFT within the GGA, the GGA–1/2 approach was employed. This method corrects the spurious electron self-interaction term.[6,7] Additionally, the calculations accounted for spin-orbit coupling (SOC) since it is known to be significant in describing the electronic structure of organic-inorganic hybrid perovskites. The VESTA and Sumo packages were utilized for structure visualization and projected DOS, respectively.[8,9] The planar average electrostatic potentials were plotted using VASPKIT.[10]

6.11 GIWAXS simulation

The GIWAXS simulations were carried out using the software SimDiffraction (By Prof. Dr. Dag W. Breiby at PoreLab, Department of Physics, Norwegian University of Science and Technology), which is developed to provide accurate calculated scattering patterns for textured polycrystalline thin films.[11] Based on the molecular crystal structure specified in the CIF files generated from the theoretical modeling, the GIWAXS patterns were predicted, taking into account the pronounced preferred orientation of the crystallites. In the present case, the *a*-*b* plane of the proposed unit cells was found to be highly parallel to the substrate surface. An orientational distribution of a few degrees ($< 3^o$) about the surface normal was included in the simulations, understood to correspond to both divergence in the incoming beam, and actual slight crystallite alignment variations. The simulations were convoluted with a fixed radial peak width of 0.05 $Å^{-1}$, accounting for crystal size broadening and also the non-monochromatic nature of the beam and other geometric broadening effects. For direct comparisons with the simulated scattering patterns, the experimental raw data were interpolated to rectilinear (Q_{xy}, Q_z) cylindrical coordinates.

6.12 Reference

1. R. Ulbricht, E. Hendry, J. Shan, T. F. Heinz and M. Bonn, *Rev Mod Phys.*, 2011, **83**, 543.
2. J. L. Garrett and J. N. Munday, *Nanotechnology*, 2016, **27**, 245705.
3. G. Kresse and J. Furthmüller, *Phys. Rev. B*, 1996, **54**, 11169.
4. J. P. Perdew, K. Burke and M. Ernzerhof, *Phys. Rev. Lett.*, 1996, **77**, 3865.
5. S. Grimme, J. Antony, S. Ehrlich and H. A. Krieg, *J. Chem. Phys.*, 2010, **132**, 154104.
6. G. Kresse and J. Furthmüller, *Comput. Mater. Sci.*, 1996, **6**, 15.
7. G. Kresse and D. Joubert, *Phys. Rev. B*, 1999, **59**, 1758.
8. K. Momma and F. Izumi, *J. Appl. Crystallogr.*, 2011, **44**, 1272.
9. A. M. Ganose, A. J. Jackson, O. Scanlon and D. Sumo, *J. Open Source Softw.*, 2018, **3**, 717.
10. V. Wang, N. Xu, J. C. Liu, G. Tang and W. T. Geng, *Comput. Phys. Commun.*, 2021, **267**, 108033.
11. D. W. Breiby, O. Bunk, J. W. Andreasen, H. T. Lemke and M. M. Nielsen, *J. Appl. Crystallogr.*, 2008, **41**, 262.

Publications

[1] **Shuanglong Wang**, Sabine Frisch, Heng Zhang, Okan Yildiz, Mukunda Mandal, Naz Ugur, Beomjin Jeong, Charusheela Ramanan, Denis Andrienko, Hai I. Wang, Mischa Bonn, Paul W. M. Blom, Milan Kivala, Wojciech Pisula and Tomasz Marszalek, Grain engineering for improved charge carrier transport in two-dimensional lead-free perovskite field-effect transistors, *Materials Horizons*, **2022**, 9, 2633.

[2] **Shuanglong Wang**, Konstantinos Bidinakis, Constantin Haese, Franziska H. Hasenburg, Okan Yildiz, Zhitian Ling, Sabine Frisch, Milan Kivala, Robert Graf, Paul W. M. Blom, Stefan A. L. Weber, Wojciech Pisula and Tomasz Marszalek, Modification of two-dimensional tin-based perovskites by pentanoic acid for improved performance of field-effect transistors, *Small*, **2023**, 2207426.

Curriculum Vitae

Shuanglong Wang

Date of Birth: 12/07/1992

Place of Birth: Henan province, China

Nationality: Chinese

Education

Ph.D. Chemistry, Max-Planck-Institute for Polymer Research	10/2019-07/2023
M.S. Microelectronics, Shanghai University	09/2016-05/2019
B.E. Material Science, Shanghai University of Engineering Science	09/2012-06/2016

Doctoral Thesis: Charge carrier transport in two-dimensional tin halide perovskite field-effect transistors

Master Thesis: Design, fabricate, and characterization of high-performance flexible organic solar cells and light-emitting diodes

Presentations

Asia-Pacific International Conference on Perovskite, Organic Photovoltaics and Optoelectronics, Kobe, Japan	Jan. 2023
Invited seminar, Nanjing University of Posts and Telecommunications	Oct. 2022
Invited seminar, Lodz University of Technology	Nov. 2021

List of publications

[1] **S. L. Wang**, S. Frisch, H. Zhang, O. Yildiz, M. Mandal, N. Ugur, B. M. Jeong, C. Ramanan, D. Andrienko, H.-I. Wang, M. Bonn, P. W. M. Blom, M. Kivala, W. Pisula*, T. Marszalek*. Grain engineering for improved charge carrier transport in two-dimensional lead-free perovskite field-effect transistors. Materials Horizons, **2022**, 9, 2633.

[2] **S. L. Wang**, K. Bidinakis, C. Haese, F. H. Hasenburg, O. Yildiz, Z. T. Ling, S. Frisch, M. Kivala, R. Graf, P. W. M. Blom, S. A. L. Weber, W. Pisula*, T. Marszalek*. Modification of two-dimensional tin-based perovskites by pentanoic acid for improved performance of field-effect transistors. Small, **2023**, 2207426.

[3] **S. L. Wang**, S. W. Wu, Z. T. Ling, H. M. Chen, H. Lian, X. Portier, F. Gourbilleau, T. Marszalek, F. Zhu, B. Wei, T. Xu*. Mechanically and thermally stable, transparent electrodes with silver nanowires encapsulated by atomic layer deposited aluminium oxide for organic optoelectronic devices. Organic Electronics. **2020**. 78. 105593.

[4] Y. Zhao, S. W. Wu, Z. T. Ling, H. M. Chen, N. J. Yu, P. C. Zhou, H. Lian, W. X. Lan, Y. J. Liao, B. Wei*, **S. L. Wang***. Systematical investigation of ultrathin doped emissive layer structure: achieving highly efficient and long lifetime orange organic light emitting diodes. Advanced Materials Interfaces. **2020**. 7. 1901609.

[5] T Xu, C. L. Gong, **S. L. Wang**, H. Lian, W. X. Lan*, G. Lévêque, B. Grandidier, J. Plain, R. Bachelot, B. Wei*, F. R. Zhu*. Ultraviolet-durable flexible nonfullerene organic solar cells realized by a hybrid nanostructured transparent electrode. Solar RRL, **2020**, 4, 1900522.

[6] J. J. Liu, Y. L. Li, **S. L. Wang**, Z. T. Ling, H. Lian, T. Xu, X. W. Zhang, Y. J. Liao*, B. Wei*. Long-lasting and efficient inverted pure blue organic light-emitting diodes by inserting an ultrathin aluminum interlayer. Journal of Alloys and Compounds, **2020**, 814, 152299.

[7] J. Y. Xie, X. J. Wang, **S. L. Wang**, Z. T. Ling, H. Lian, N. Liu, Y. J. Liao, X. Y. Yang, W. S. Qu, Y. Peng*, W. X. Lan*, B. Wei. Solution-processed ZnO/MoS_2 quantum dots electron extraction layer for high performance inverted organic photovoltaics. Organic Electronics, **2019**, 75, 105381.

[8] K. P Liu, O. Cristini-Robbe, O. I. Elmi, **S. L. Wang**, B. Wei, I. S. Yu, X. Portier, F. Gourbilleau, D. Stiévenard, T. Xu*. Tunneling atomic layer-deposited aluminum oxide: a

correlated structural/electrical performance study for the surface passivation of silicon junctions. Nanoscale Research Letters, **2019**, 14, 1.

[9] J. J. Liu, Y. Zhao, **S. L. Wang**, T. Xu, W. X. Lan*, B. Wei. Efficient inverted top-emitting organic light-emitting devices with double electron injection layers. Optics & Laser Technology, **2019**, 117, 260.

[10] **S. L. Wang**, Y. Zhao, H. Lian, C. Y. Peng, X. Y. Yang, Y. L. Gao, Y. Peng, W. X. Lan, O. Ibrahim Elmi, D. Stiévenard, B. Wei*, T. Xu*, Furong Zhu*. Towards all-solution-processed top-illuminated flexible organic solar cells using ultrathin Ag-modified graphite-coated poly(ethylene terephthalate) substrates. Nanophotonics. **2019**. 8. 297.

[11] Z. H. Ye, Z. T. Ling, M. Y. Chen, J. L. Yang, **S. L. Wang**, Y. Q. Zheng, B. Wei, C. Li, G. Chen*, and Ying Shi*. Low energy consumption phosphorescent organic light-emitting diodes using phenyl anthracenone derivatives as the host featuring bipolar and thermally activated delayed fluorescence. RSC Advances. **2019**, 9, 6881.

[12] C. Y. Peng, K. P. Liu, **S. L. Wang**, N. J. Yu, Z. Y. Tang, Z. T. Ling, H. Lian, G. Chen*, Y. J. Liao, W. X. Lan, B. Wei*. Efficient and chromaticity-stable flexible white organic light-emitting devices based on organic-inorganic hybrid color-conversion electrodes. RSC Advances, **2019**, 9, 22577.

[13] G. j. Shi, X. Z. Zhang, M. Q. Wan, **S. L. Wang**, H. Lian, R. Xu, W. Q. Zhu*. High-performance inverted organic light-emitting diodes with extremely low efficiency roll-off using solution-processed ZnS quantum dots as the electron injection layer. RSC Advances, **2019**, 9, 6042.

[14] J. H. Zhang, Y. X. Guan, J. L. Yang, W. Q. Hua, **S. L. Wang**, Z. T. Ling, H. Lian, Yi. J. Liao, W. X. Lan, B. Wei*, W.-Y. Wong*. Highly-efficient solution-processed green phosphorescent organic light-emitting diodes with reduced efficiency roll-off using ternary blend hosts. Journal of Materials Chemistry C, **2019**, 7, 11109.

[15] Y. H. Wu, J. L. Yang, **S. L. Wang**, Z. T. Ling, H. Zhang*, B. Wei*. High-performance

white organic light-emitting diodes using distributed bragg reflector by atomic layer deposition. Applied Sciences, **2019**, 9, 1415.

[16] Z. T. Ling, Y. Zhao, **S. L. Wang**, S. H. Pan, H. Lian, C. Y. Peng, X. Y. Yang, Y. J. Liao, W. X. Lan*, B. Wei, G. Chen*. High-performance light-soaking-free polymer solar cells based on a LiF modified ZnO electron extraction layer. Journal of Materials Chemistry C, **2019**, 7, 9354.

[17] **S. L. Wang**, J. L. Yang, T. Xu, D. H. Dou, Z. Y. Tang, Z. X. Gao*, M. Y. Chen, K. P. Guo, J. S. Yu, J. Plain, R. Bachelot, J. H. Zhang, B. Wei*. Highly efficient and foldable top-emission organic light-emitting diodes based on Ag-nanoparticles modified graphite electrode. Organic Electronics. **2018**. 64. 146.

[18] **S. L. Wang**, M. Y. Qiao, Z. H. Ye, D. H. Dou, M. Y. Chen, X. Y. Yang, Y. Peng, Y. Shi, J. Y. Li, C. J. Li*, Bin Wei*, Wai-Yeung Wong*. Efficient deep-blue electrofluorescence with an external quantum efficiency beyond 10%. iScience. **2018**, 9. 532. 20189.

[19] M. Y. Chen, J. L. Yang, Z. H. Ye, **S. L. Wang**, Z. Y. Tang, G. Chen, Y. Q. Zheng, Y. Shi*, B. Wei*, W.-Y. Wong*. Extremely low-efficiency roll-off of phosphorescent organic light-emitting diodes at high brightness based on acridine heterocyclic derivatives. Journal of Materials Chemistry C, **2018**. 6, 9713.

[20] B. Wei, Z. Y. Tang, **S. L. Wang**, C. P. Qin, C. Y. Li, X. W. Ding, Y. L. Gao, X. Portier, F Gourbilleau, D Stiévenard, T. Xu*. Enhanced photovoltaic performance of inverted polymer solar cells through atomic layer deposited Al_2O_3 passivation of ZnO-nanoparticle buffer layer. Nanotechnology, **2018**, 29, 395204.

[21]

Acknowledgement

Doing a PhD is one of the best decisions I have ever made in my life so far. My research experience at Max-Planck-Institute for Polymer Research has been what I would expect. After nearly four years of research, my PhD training is approaching a conclusion. I'm really appreciate to my families and all of my lovely friends and colleagues who kindly supported me during my PhD study. At first, I would like to thank Dr. Tomasz Marszalek and Prof. Dr. Wojciech Pisula for providing me the opportunity to join AK-Blom and work on the fascinating research topic of perovskite field-effect transistors. They provided me with detailed guidance over the four years. I am grateful for their intelligence, patience, passion for research, and dedication for excellence. Secondly, I would like to thank Prof. Dr. Paul W. M. Blom for his supportive supervision. His helpful and insightful comments are of great significance to me during my research projects. A special thanks to Ms. Petra Pausch for all her kind assistance from the first moment that I was admitted at MPIP until now.

Many thanks to Dr. Beomjin Jeong, Dr. Jasper J Michels, Dr. Ulrike Kraft and Dr. Yungui Li in my group for their fruitful discussions.

Special thanks to Lei Gao, Franziska Hasenburg, Sabine Frisch, Naz Ugur, Heng Zhang, Okan Yildiz, Konstantinos Bidinakis, Constantin Haese, Zhitian Ling, Oscar Sachnik, Dr. Mukunda Mandal, Dr. Charusheela Ramanan, Dr. Hai I. Wang, Dr. Denis Andrienko, Dr. Robert Graf, Prof. Dr. Milan Kivala, Prof. Dr. Stefan A. L. Weber, Prof. Dr. Dag W. Breiby for their contribution to the publications, continuous support, sympathetic advises, as well as friendly and constructive discussions.

I would like to thank the technician Christian Bauer, Frank Keller, Verona Maus, Sirma Koynova, and Leon Prädel for their supportive and kind cooperation in the lab.

Many thanks to all my colleagues and friends at AK-Blom and all the others for their support and the nice working atmosphere. It was a great pleasure working with all of you.

Lastly, I would also like to express my special thanks to my family for their everlasting support and encouragement.

Shuanglong Wang

Mainz, Germany

June 2023